Multi time-step tomographic wave-front reconstruction for wide field Adaptive-Optics in astronomy

博士論文

Multi time-step tomographic wave-front reconstruction for wide field Adaptive-Optics in astronomy

(天文学における広視野補償光学のための複タイムステップトモグラフィー波面再構成)

大野 良人

平成27年

Abstract

In this thesis, we develop and evaluate a new tomographic wave-front reconstruction method for wide-field adaptive optics (WFAO) systems, called *multi time-step wave-front reconstruction*, to solve the lack of information in tomographic reconstructions and expand the field of regard (FoR) of WFAO systems. Also, we evaluate a method to estimate wind speeds and directions at multiple altitudes using the measurements from multiple wave-front sensors. This wind estimation method is required to implement the multi time-step reconstruction. The basic idea of the multi time-step reconstruction is to increase the information using the measurements at both the current and previous time-steps, which requires wind speeds and directions of wind and the frozen flow assumption.

First, we demonstrate the influence of the lack of information in the tomographic reconstruction. Then, we present that the multi time-step tomographic reconstruction method is effective to reduce the tomographic error due to the lack of information.

Second, we show the result of the numerical simulation of the tomographic reconstruction on a multi-object adaptive optics (MOAO) system on a future extreme large telescope. The numerical simulation shows that the multi time-step reconstruction increases Strehl ratio (SR) over a field of regard of 10 arcminutes diameter by a factor of 1.5–1.8 if we know the wind speeds and directions.

Third, we evaluate the multi time-step reconstruction and the wind estimation method in the laboratory experiment on RAVEN, which is a MOAO demonstrator. We can successfully measure the wind speeds and directions in the laboratory experiment. Also, the multi time-step reconstructor can increase an ensquared energy (EE) in a 140 mas box by 0.03–0.05.

Finally, we present the on-sky performance of the multi time-step reconstruction and the wind estimation with RAVEN on the Subaru telescope. Unfortunately, there is no clear improvement by the multi time-step reconstruction because of the error of the wind estimation. With the off-line analysis with the on-sky measurements of the wave-front sensors, we improve the wind estimation method and re-evaluate the multi time-step reconstruction. We conclude that the multi time-step reconstruction can reduce the WFE compared with the normal tomographic reconstruction if the decay ratio of the cross-correlation of WFS slopes is more than 0.7 and there is no dome seeing.

Acknowledgements

I would like to express my special appreciation and thanks to my supervisor Masayuki Akiyama. He always encouraged me in the research and give me precious opportunities to research with overseas researchers. Your advice on both research as well as on my career have been priceless. I would also like to thank Shin Oya, who supports my research as well as my stay in Hawaii. I would also like to thank Olivier Lardiére, Carlos Correia, Colin Bradley, and other RAVEN members. This thesis is based on the work with them in the RAVEN project, and they support my research. I would also like to thank staff members of Subaru telescope for their support.

I would like to thank the three referees of my thesis, Hideki Takami, Takashi Murayama, Takashi Ichikawa. I received many helpful comments from them. I would like to thank the students in the astronomical institute of Tohoku University.

A special thanks to my family. At the end I would like express appreciation to my wife Aya who always support me.

Contents

List of Figures

List of Tables

Chapter 1

Introduction to Wide-Field AO Systems and Tomographic Reconstruction

1.1 Background

In ground-based observations for astronomy, we suffer from the turbulence in the Earth's atmosphere, especially in the optical and near infrared (NIR) wavelengths. Due to the atmospheric turbulence, the phase of the light propagating from space to a telescope through the atmosphere is disturbed and the image produced by the telescope is blurred. As a result, we lose the sensitivity and the spatial resolution for the astronomical observation. Adaptive optics (AO) is a system which corrects the phase distortion due to the atmospheric turbulence. Now, most of large ground-based telescopes, which have a primary mirror of 8–10 meters diameter, have a classical AO system, called *single-conjugate adaptive optics* (SCAO). These SCAO systems successfully achieve the high spatial resolution close to the diffraction limit of these telescopes and allow us to observe fainter objects and smaller structures in galaxies. AO systems are considered as an essential technique for future *extreme large telescopes* (ELTs), which have a primary mirror of diameter larger than 30 meters, to maximize their spatial resolution and sensitivity.

Classical SCAO systems have a critical limitation. It is a limitation that the correction of SCAO is effective only within a limited angle from a guide star (GS). Wide-field AO (WFAO) concepts, involving *tomographic wave-front reconstruction* to estimate the atmospheric volume, come out from requirements to apply AO correction into a wide field and to increase the efficiency of AO assisted observations. The developments for WFAO system have already started and actually, some WFAO systems are working on the current large telescopes as a facility

instrument or demonstrator. However, there are many new techniques and difficulties for realizing WFAO systems on the future ELTs. One of the new techniques not used in SCAO systems is *tomographic wave-front reconstruction*. In this thesis, we develop a tomographic wave-front reconstruction algorithm to expand the field in which the WFAO correction is effective, called *field of regard* (FoR), and to maximize the efficiency of WFAO systems.

We will start this chapter with explaining a basic theory of the atmospheric turbulence. Since the atmospheric turbulence is a non-stationary random phenomenon, we need to understand and characterize the atmospheric turbulence statistically. This statistical theory of the atmospheric turbulence is an important basis to design and evaluate AO systems. We will then present the principle of SCAO systems and their limitations. Then, we will outline three WFAO concepts and the challenging points to realize these WFAO systems especially for future ELTs. We will provide more introduction about the tomographic wave-front reconstruction. At the end of this chapter, we will summarize the object of this thesis.

1.2 Atmospheric Turbulence

This section is based on Hardy (1998) [24].

1.2.1 Kolmogorov Theory

Kolmogorov[30] investigated the statistical structure of turbulence, which is the velocity fluctuations in a fluid medium. In his theory, when energy is injected to the fluid medium, it forms a large length-scale disturbance. The length-scale at which the energy injection occurs is referred to as *outer scale*, L_0. Then, the injected energy is broken down into smaller length-scale, forming an *energy cascade*, until a small scale where the energy is dissipated by viscosity, called *inner scale* ℓ_0.

In Earth's atmosphere, the main energy input is solar heating during the daytime, which causes turbulences on the length-scale of L_0 by the local convection. In the night time, the air masses of different altitudes and temperatures are mixed by wind shearing and the turbulences break down into smaller scale until the inner scale ℓ_0. This process causes temperature fluctuations in the atmosphere, which affect the density of the air and therefore result in refractive index fluctuations. The phases of light rays from space are disturbed by the refractive index fluctuations

in the atmosphere. In the remainder of this thesis, we use a term of *atmospheric turbulence* for the turbulence of the refractive index in the atmosphere.

1.2.2 Structure Function

In order to describe a non-stationary random variation of the atmospheric variables, such as velocity, temperature, and refractive index, *structure function*[30] D_f for the non-stationary random variable f at two different points is defined as

$$D_f(\boldsymbol{\rho}) = \langle [v(\boldsymbol{r}) - v(\boldsymbol{r}+\boldsymbol{\rho})]^2 \rangle, \tag{1.1}$$

where $\boldsymbol{r} = (x, y, z)$ is a vector of a three-dimensional coordinate, $\boldsymbol{\rho}$ is a spatial separation between two points, and $\langle\rangle$ represents an ensemble average. The structure function corresponds to the intensity of the fluctuations in $f(\boldsymbol{r})$ over scales equal to or less than $\boldsymbol{\rho}$. The turbulences of the atmospheric variables are a non-stationary random variables, that is, their mean value varies over time. However, in fact, this change occurs rather smoothly and therefore the structure function D_f can be considered a stationary random function, if $\boldsymbol{\rho}$ is not too large. The turbulences of the atmospheric variables are also considered to be isotropic and homogeneous in small scales. Therefore, the structure functions of these variables only depend on a separation distance $\rho = |\boldsymbol{\rho}|$. The structure function D_f can be represented by the correlation function B_f as

$$D_f(\rho) = 2[B_f(0) - B_f(\rho)], \tag{1.2}$$

where $B_f(\rho) = \langle f(r) f(r+\rho) \rangle$ and $B_f(0)$ is a mean-square value of the variable f.

Kolmogorov found that a two-thirds power law for the velocity structure function $D_v(\rho) \propto \rho^{2/3}$. Obukhov [41] showed that Kolmogorov's law can be applied to the temperature structure function, i.e. $D_T(\rho) = C_T^2 \rho^{2/3}$, where C_T is the temperature structure constant. Similarly, the refractive index structure function is given by

$$D_N(\rho) = C_N^2 \rho^{2/3}, \tag{1.3}$$

where C_N^2 is the structure constant of the refractive index with a unit of $\mathrm{m}^{-2/3}$. This constant C_N^2 represents the strength of the atmospheric turbulence and varies with altitude and time. The vertical profile of this constant, $C_N^2(h)$, is commonly used to characterize the condition of the atmospheric turbulence. The C_N^2 profile is measured at many places. From the profiling of the C_N^2 with balloons [37], it is

found that the C_N^2 profile has peaks at several altitudes and therefore the atmospheric turbulence can be considered as the multiple discrete layers. In good sites for astronomical observations, it is known that more than 60% of the turbulence is concentrated in the ground layer [16], which is the turbulence lower than 0.5 km, and additional turbulence layers are often within 4–10 km.

Tatarski [47] showed that the three-dimensional power spectrum of refractive index can be expressed as

$$\Phi_N(\kappa) = 0.033 C_N^2 \kappa^{-11/3} \tag{1.4}$$

where κ is a spatial wave number $\kappa = 2\pi/\rho$. This expression is only valid within the range of $L_0 > \rho > \ell_0$, which is called *inertial range*.

1.2.3 The Near-Field Approximation

In the remainder of this thesis, we use the near-field approximation for the light propagation through the atmosphere turbulence, in which the diffraction is neglected and light rays propagate straight through the atmospheric turbulence. Under this approximation, the phase distortion of the wave-front propagating to an aperture can be considered as the sum of phase distortions along the optical path of the light ray in the atmosphere. This approximation is valid for weak turbulence found at good sites for astronomical observations.

With a characteristic size of the turbulence ℓ and a wavelength λ, the first-order diffracted angle is given as $\theta = \lambda/\ell$. Diffracted rays interfere when the travel distance is comparable to $L \approx \ell/\theta$. From the turbulence profile at the top of the Maunakea measured by Thirty Meter Telescope project [16], the characteristic size of the turbulence ℓ is 0.25 m at altitude of 16 km in the worst case, which assuming 75 %ile model and low observation elevation of 30 degrees. This corresponds to a travel distance $L = 130$ km, which is much larger than the maximum of the atmospheric turbulence altitude. Therefore, the interference effect is negligible at good sites such as the top of Maunakea and the effect due to the atmospheric turbulence can be described based on the near-field approximation.

1.2.4 Effect of Turbulence

Let us consider that there is n_{layer} turbulence layers. In the near field approximation, the shift of the phase due to the refractive index fluctuations of i-th

turbulence layer at altitude h_i with a thickness of δh_i is

$$\phi_i(\boldsymbol{x}) = k \int_{h_i}^{h_i+\delta h_i} dz\ n(\boldsymbol{x}, z), \tag{1.5}$$

where $\phi_i(\boldsymbol{x})$ is a phase aberration at a two-dimensional coordinate $\boldsymbol{x}$ on i-th turbulence layer, k is a wave number $k = 2\pi/\lambda$, and $n(\boldsymbol{x}, z)$ is a refractive index minus 1.

The total aberration due to n_{layer} layers is given simply by

$$\phi(\boldsymbol{x}) = \sum_{i=1}^{n_{layer}} \phi_i(\boldsymbol{x}). \tag{1.6}$$

The phase structure function for the Kolmogorov turbulence is represented by substituting Eq. (1.5) into Eq. (1.1) as $f = \phi$ and using Eq. (1.4) as

$$D_\phi(\xi) = 6.88 \left(\frac{\xi}{r_0}\right)^{5/3}, \tag{1.7}$$

where ξ is a separation distance on a two-dimensional plane and r_0 is *Fried parameter* [17] in unit of meter as

$$r_0 = \left[0.423k^2 \sec\zeta \int dh C_N^2(h)\right]^{-5/3}, \tag{1.8}$$

where ζ is a zenith angle. Fried parameter r_0 is also referred to as a turbulence coherence length and is the diameter over which a mean-square value of the phase distortion corresponds to 1 rad^2 at a wavelength of λ. Fried parameter r_0 is convenient measure of the strength of turbulence. The typical size of r_0 is 0.15 m at the visible length of 0.5 μm in good sites at night. Fried parameter varies with wavelength as $\lambda^{1.2}$. This means that shorter wavelength is more affected by the turbulence compared with longer wavelength at the same C_N^2. Similarly, a coherence angle, which represents an angular separation within which a mean-square value of the phase difference between two wave-fronts propagating different path in the atmosphere corresponds to 1 rad^2 at a wavelength of λ, is defined as

$$\theta_0 = \left[2.914k^2(\sec\zeta)^{8/3} \int dh C_N^2(h) h^{5/3}\right]. \tag{1.9}$$

This coherence angle is referred to *isoplanatic angle*. The isoplanatic angle is represented by r_0 as

$$\theta_0 = 0.314(\cos\zeta)\frac{r_0}{\bar{h}} \tag{1.10}$$

where $\bar{h}$ is a weighted mean turbulence height,

$$h = \int dh C_N^2(h) h^{5/3}. \tag{1.11}$$

The power spectrum for the phase fluctuation is given by

$$\Phi_\phi(\kappa) = 0.023 r_0^{-5/3} \kappa^{-11/3}. \tag{1.12}$$

1.2.5 Limitation of the Kolmogorov Model

As stated in 1.2.2, the Kolmogorov turbulence model is valid only within the inertial range, that is, for $L_0 > \xi > \ell_0$. In the astronomical imaging, the inner scale has only negligible effect because the turbulence power is weak at the inner scale, but the outer scale has a major impact when the size of a telescope aperture D is comparable to the outer scale. The turbulence with the spatial scale larger than the aperture diameter of the telescope contributes the tip-tilt modes of the phase distortion over the aperture. This tip-tilt modes causes image motion on the focal plane. In the case of long exposure, The size of point spread function (PSF), which is equal to the image of a point-like source, depends on this motion. If the atmospheric turbulence follows the von Karman model and the outer scale is finite, the PSF size affected by the atmospheric turbulence become smaller than the size expected by the Kolmogorov model.

The modified model including the outer scale was proposed by von Karman. Using the von Karman model, the power spectrum Eq. (1.12) and the structure function Eq. (1.7) for phase fluctuations are given as [9]

$$\Phi_\phi(\kappa) = 0.023 r_0^{-5/3} \left[\kappa^2 + \left(\frac{2\pi}{L_0}\right)^2\right]^{-11/6}, \tag{1.13}$$

$$D_\phi(\xi) = 0.172 \left(\frac{r_0}{L_0}\right)^{-5/3} \left[1 - \frac{2\pi^{5/6}}{\Gamma(5/6)} \left(\frac{\xi}{L_0}\right)^{5/6} K_{5/6}\left(\frac{2\pi\xi}{L_0}\right)\right] \tag{1.14}$$

where Γ is the gamma function and K denotes the modified Bessel function of the second kind. Fig. 1.1 shows the power spectrum and the structure functions of the phase fluctuations with the Kolmogorov model and the von Karman model. In

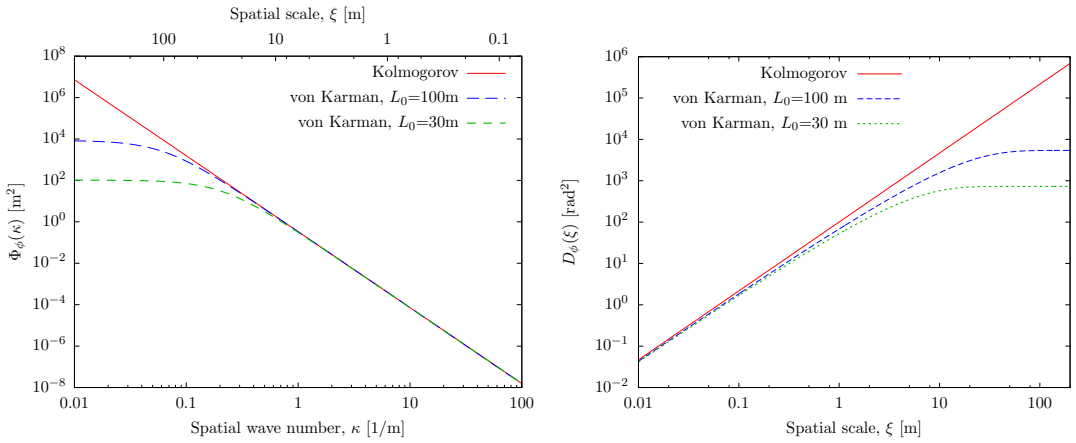

Figure. 1.1: The power spectrum (the left panel) and the structure function (the right panel) for phase fluctuations with the Kolmogorov model (the red solid lines) and the von Karman model as L_0=100 m (the blue dashed lines) and L_0=30 m (the green dotted lines). Fried parameter is set to r_0=0.2 m.

both figures, the von Karman model shows a flatter spectra in spatial scales larger than the size of the outer scale.

The full width at half maximum (FWHM) is a diameter at which the intensity of PSF is a half of its peak value. With assuming the Kolmogorov model, FWHM of long-exposure PSF, $\theta_{\text{Kolmogorov}}$, at a wavelength of λ is computed numerically by a fourier transform of the optical transfer function $\exp[-0.5D_\phi(\lambda f)]$ [48], where f is the spatial frequency,

$$\theta_{\text{Kolmogorov}} = 0.98\frac{\lambda}{r_0}. \tag{1.15}$$

Tokobinin [48] simulated the effect of the outer scale on the seeing size numerically. The FWHM of the PSF for the von Karman turbulence is approximated as

$$\theta_{\text{vonKarman}} \approx \sqrt{1 - 2.183\left(\frac{r_0}{L_0}\right)^{0.356}}\,\theta_{\text{Kolmogorov}}. \tag{1.16}$$

This approximation is obtained by fitting to the numerical results and shows good agreement with numerical results for $L_0/r_0 > 22$. Fig. 1.2 shows the seeing size difference between the Kolmogorov and the von Karman model. The seeing size of the von Karman model becomes much smaller because there is no turbulence which spatial scale is larger than L_0 in the von Karman model. This feature is measured at 6.5 m Magellan telescopes [13].

A dome seeing, which occurs in a telescope dome, do not follow the Kolmogorov turbulence. The dome seeing is difficult to be modeled because it depends on the dome and telescope structure, temperature, and observation site. This dome seeing

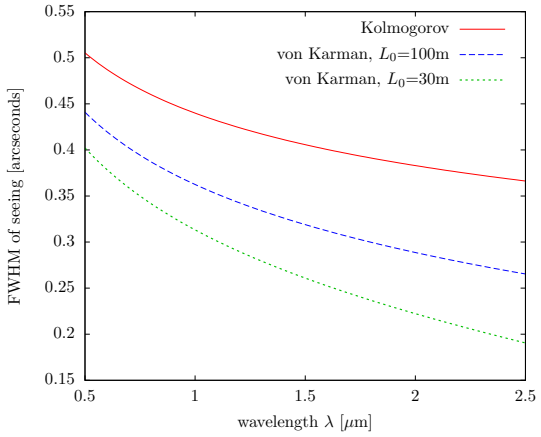

Figure. 1.2: The seeing size for the Kolmogorov model (the red solid lines) from Eq. (1.15) and the von Karman model as L_0=100 m (the blue dashed lines) and L_0=30 m (the green dotted lines) computed by Eq. (1.16). Fried parameter is set to r_0=0.2 m at λ=0.5 μm.

turbulence increases the turbulence power at ground and sometimes has a large effect on astronomical observations.

1.2.6 Taylor Hypothesis

The time evolution of the atmospheric turbulence can be expressed by two effects : the boiling due to the energy cascade and the shifting due to wind. The first effect can be considered to be neglected within a short time scale and this assumption is well known as *Taylor's hypothesis of frozen flow*. In this condition, the atmospheric turbulence can be modeled simply by multiple turbulence layers moving due to winds with time. Furthermore, the frozen flow assumption allow us to predict the time evolution of the atmospheric turbulences, i.e., the spatial displacement of a turbulence layer with wind $\boldsymbol{v}$ during time duration Δt is $\boldsymbol{v}\Delta t$. Many studies verify the frozen flow assumption on-sky and suggest that the time scale in which the frozen flow assumption is valid is range from a few ms to 100 ms, which depends on conditions [21, 42, 46].

1.3 Principle of SCAO system

1.3.1 Single-Conjugate Adaptive Optics

Fig. 1.3 shows a schematic view of a SCAO system. In principle, an AO system consists of a *guide star* (GS), *wave-front sensor* (WFS), *controller*, and *deformable*

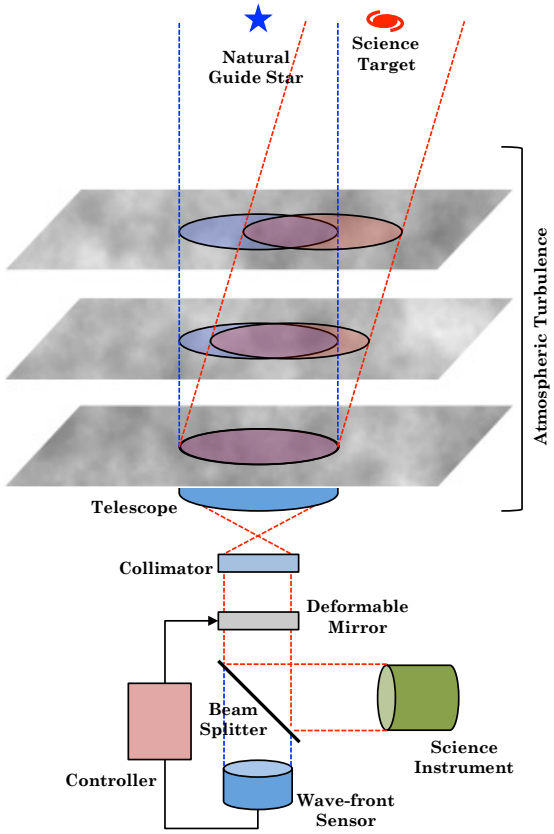

Figure. 1.3: The schematic view of a SCAO system.

mirror (DM). The process of AO correction is basically performed by the following steps. First, the light from a GS is observed by a WFS to measure the wave-front distortion in the direction of the GS. Second, a shape of a deformable mirror is computed from the measurement in order to compensate the wave-front distortion when the DM reflects the light. Third, DM shape is controlled and the correction is applied to the wave-front of the light from a science target. In most of the current AO system, the wave-front distortion is measured in the optical wavelength and the correction is done in NIR wavelength. This is because the AO correction works better in longer wavelength than shorter wavelength, which is more sensitive to the residual of the correction of the atmospheric turbulence. The optical light from the GS is split by a beam splitter and fed to WFS.

Guide star

GS is required as wave-front reference. Although the best case is that science target itself is a bright point source and can be used as a GS, the science target is usually a faint and extended object, such as an extra-galaxy, and therefore we have to find a bright star around the science target, which can be used as a GS, it is called *natural guide star* (NGS). In this case, the

AO correction is performed based on the wave-front distortion in the NGS direction. If the science target is far from the NGS, the light of the science target propagates through different path from the path of the NGS at high altitude in the atmosphere, as shown in Fig. 1.3. This difference makes the performance of the SCAO correction worse. Therefore, the performance of the SCAO correction decreases with the angular separation from NGS. The permissible separation from the NGS is characterized by the isoplanatic angle θ_0, which is roughly 10 arcseconds in H-band even at good observing sites. The limitation is known as *angular anisoplanatism*. Due to the angular anisoplanatism, the shape of corrected PSF varies increasingly with the angular separation from the NGS. In addition, sufficiently bright stars are not available in all parts of the sky, and therefore, the sky-coverage of NGS based AO system is very limited. Related to the sky-coverage, however, we can improve by using artificial guide star, that is, *laser guide star* (LGS).

Wave-front sensor

The most used WFS is Shack-Hartmann WFS (SH-WFS). The SH-WFS divides the image of the telescope aperture into the sub-apertures by a micro-lens-array and measures a wavefront gradients in each subaperture. The wave-front propagating into SH-WFS can be reconstructed from the measurement of the local gradients. This process is called *wave-front reconstruction*.

Deformable mirror

The correction is done by a DM. In general, tip-tile modes, which are the strongest mode, are corrected by another tip-tilt mirror to relax the requirements for the stroke of the DM. The size of the element of a DM determines the smallest spatial size which we can correct by an AO system. The turbulence with the spatial scale below the element size of the DM can not be corrected by the system, known as *fitting error*.

Control

For the real-time compensation, the AO loop needs to be controlled faster than the coherence time of the atmospheric turbulence [24] given by

$$\tau_0 = 0.134/f_G, \tag{1.17}$$

where f_G is the Greenwood frequency given by

$$f_G = \left[0.102k^2 \sec(\zeta) \int_0^\infty C_N^2(h) v(h)^{5/3} dh\right]^{3/5}. \tag{1.18}$$

where $v(h)$ is a wind speed at altitude h. The typical value of the coherence time τ_0 is a few ms even at good observation sites. It means that the required frequency for the AO control is order of hundreds Hz. Therefore, the required computation time for the wave-front reconstruction is around 1 ms.

In order to optimize and stabilize the performance of AO system, we have to consider the temporal control of AO system. The SCAO system is performed in *closed loop*, in which the WFS is put behind of a DM and measures the residual wave-front distortion corrected by the DM, that is, there is feedback from WFS into DM. The simplest controller is an integrator, but more optimized controls are proposed. This temporal control is not in the scope of this thesis, but it is very important for an AO system.

1.3.2 Laser Guide Star AO System

LGS can improve the sky-coverage of an AO system. It is an artificial star created by a laser beam. There are two kinds of the LGS system : Rayleigh LGS and sodium LGS. The first one uses Rayleigh scatter in the atmosphere and is created at altitude of 10–20 km. The other one is created in the sodium layer at altitude of around 90 km by exciting the state of sodium with a laser at wavelength of 589 nm. In this thesis, we focus on the sodium LGS, which is mainly used in the AO systems of the current large telescopes.

Although using LGS allows us to create GS anywhere we want, there are some difficulties and limitation of LGS.

Insensitivity for the overall tip-tilt modes

Even if we use a LGS, another NGS is required to measure overall tip-tilt modes, which is called tip-tilt NGS (TT-NGS). Since the light of LGS propagates through the atmosphere twice, going up from a laser launch telescope and going down from the LGS, the effect of the overall tip-tilt due to the atmospheric turbulence is cancelled out and therefore we can not measure the overall tip-tilt modes by LGS. The TT-NGS can be fainter than the NGS. In the case of NGS, the limit-magnitude is determined by the size of the subapertures of SH-WFS. On the other hand, since the overall tip-tilt can

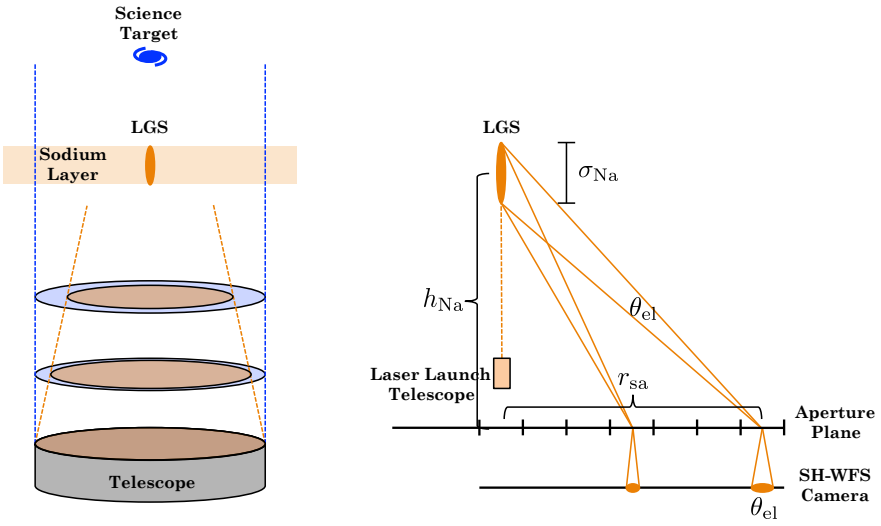

Figure. 1.4: The schematic images for the cone effect and the spot elongation due to the LGS.

be measured from the image motion in only one aperture, the magnitude limit of TT-NGS is determined by the size of the telescope aperture. In addition, since overall tip-tilt modes have relatively large isoplanatic angle compared with high order modes, the angular anisoplanatism for the overall tip-tilt modes, known as *tilt anisoplanatism*, has weaker dependence on the separation than angular anisoplanatism. Therefore, the permitted separation of TT-NGS from the LGS is larger than the one for NGS. Thus, using the LGS can improve the sky-coverage compared with NGS AO system even though we need another TT-NGS.

Cone effect

The LGS is created at finite altitude and its light propagates in the atmosphere with a conical optical path as shown in the left panel of Fig. 1.4. As a result, the volume of the atmospheric turbulence measured by the LGS is different especially at high altitudes from the turbulence volume in which the light of the science target propagates. This result in the deterioration of the SCAO performance. This is known as *cone effect* or *focal anisoplanatism*. The effect increases with the size of the telescope aperture and will be severe in the future ELTs.

Spot elongation of sodium laser on SH-WFS

From on-sky lidar measurements of sodium layer [5], it is observed that the sodium layer has a vertical thickness of roughly 10 km. Due to this thickness,

the angular size of the LGS spot is elongated in radial direction on the SH-WFS as shown in the right panel of Fig. 1.4. The degree of the elongation, θ_{el}, increases with the horizontal distance on the aperture plane between the subaperture and the laser launch telescope, r_{sa}, and is approximated as

$$\theta_{\mathrm{el}} \approx \frac{r_{\mathrm{sa}}\sigma_{\mathrm{Na}}}{h_{\mathrm{Na}}^2} \tag{1.19}$$

where h_{Na} is the altitude of the sodium layer and σ_{Na} is the thickness of the sodium layer. If it is assumed that h_{Na}=90 km, σ_{Na}=10 km, zenith direction, and the center launch system, in which the laser is launched from the back of the secondary mirror, the elongation at the outermost subaperture is roughly 1 arcseconds for a 8 m telescope and 4 arcseconds for a 30 m telescope. This elongation causes spot position estimation errors for outer subapertures [19]. In reality, the vertical profile of the sodium layer has complex structure and varies with time, and the spot elongation pattern also varies.

1.3.3 Performance Metrics

There are different metrics to evaluate the performance of AO correction. One is a *wave-front error* (WFE) which is computed from WFS telemetry data. Others are FWHM, *Strehl ratio* (SR), and *ensquared energy* measured from observed PSF.

Wave-front error

WFE is defined as the root mean square (rms) value of the residual wave-front distortion. If the residual phase distortion of the wave-front is denoted by φ, the WFE σ is expressed as

$$\sigma = \sqrt{\frac{1}{S}\int \left(\varphi(\boldsymbol{x}) - \bar{\varphi}\right)^2 d\boldsymbol{x}} \tag{1.20}$$

where S is the telescope pupil area and $\bar{\varphi}$ is an average of the residual distortion over the telescope pupil.

Full width at half maximum

FWHM is a diameter at which the intensity of PSF is a half of its peak value. The FWHM affected by the atmospheric turbulence is represented by Eq. (1.15) and Eq. (1.16). It is noted that the FWHM is often measured by fitting two-dimensional gaussian or moffat function to the observed PSF for convenience, but, to be exact, the gaussian and moffat function are not

good approximation of the PSF corrected by an AO system because the AO corrected PSF has two components, which are a corrected bright core and uncorrected diffuse halo.

If there is no turbulence, the PSF is determined by the diffraction due to optics, which is called *diffraction-limited*, and have diffraction pattern, known as airy disk for circular aperture. The radius of the innermost dark ring of the diffraction-limited PSF is given by

$$\theta_{\text{dif}} = 1.22\frac{\lambda}{D} \tag{1.21}$$

where D is aperture diameter. The FWHM of the diffraction-limited PSF is given by $1.03\lambda/D$. The FWHM of the uncorrelated PSF is represented by Eq. (1.15) or Eq. (1.16) depending the turbulence model.

Strehl ratio

Strehl ratio (SR) is the ratio of peak intensity of observed PSF to the peak intensity of the diffraction-limited PSF, has a value from 0 to 1. The goal of AO system is maximizing the SR by the correction. The SR can be estimated from the WFE by using Mareshal approximation [24],

$$\text{SR} \approx e^{-\sigma^2}. \tag{1.22}$$

Although this expression is very useful, it is accurate to a couple of percent for rms errors of $1/10\lambda$.

Ensquared energy (EE)

The ensquared energy (EE) is a fraction of intensity within a defined square, which is used to evaluate AO performance for spectroscopic observation by setting a square size to the width of a slit.

1.4 Wide-Field Adaptive Optics

While SCAO systems with both NGS and LGS are well-established and provides near diffraction-limited spatial resolution in NIR wavelength on the current large telescopes, there are scientific demands to apply AO correction to wide FoR to increase an observation efficiency or/and PSF uniformity over the wide FoR. As mentioned in the previous section, the size of FoR of a SCAO system is limited by the angular anisoplanatism. In order to overcome the angular anisoplanatism,

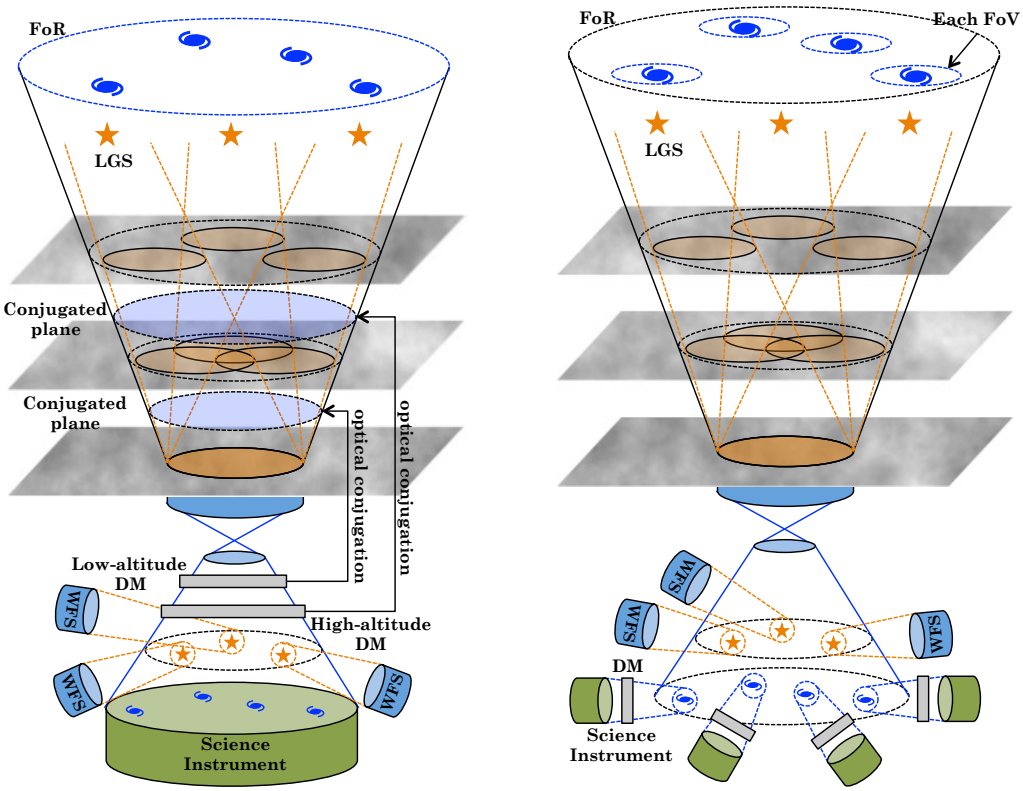

(a) MCAO (b) MOAO

(c) GLAO

Figure. 1.5: The schematic views of WFAO systems.

three WFAO concepts with using multiple LGSs are proposed: *multi-conjugate adaptive optics* (MCAO), *multi-object adaptive optics* (MOAO), and *ground-layer adaptive optics* (GLAO). The schematic views of these systems are shown in Fig. 1.5. Each WFAO system is design for different purposes. In this section, we introduce principle, advantage, disadvantage, and current/future systems of each WFAO concepts briefly.

1.4.1 Multi-Conjugate Adaptive Optics

MCAO system was proposed by Beckers [6]. MCAO system requires the tomographic wave-front reconstruction to reconstruct a three-dimensional structure of the phase distortion due to the atmospheric turbulence with using multiple LGSs. Then, MCAO system compensates for the phase distortion three-dimensionally by multiple DMs based on the reconstructed phase distortion. The number of DMs is usually 2–3, which are put in series and conjugated at different heights in the atmosphere (the blue planes in the Fig. 1.5(a)). MCAO system provides a uniform correction over a wide field of view (FoV) of 1–2 arcminutes. This is a main advantage of MCAO system and good for the precise photometry and astrometry. In addition, using multiple LGSs can reduce the cone effect of LGSs, which however is not limited to a MCAO system. This is important for future ELTs, where the cone effect will be severe. As shown in Fig. 1.5(a), the measurement of wave-fronts is done in closed-loop in MCAO system, in which WFSs are put after DMs and measure the residual wave-front distortions.

MCAO system suffers from *generalized fitting error* due to the discrete number of DMs [43]. Consider the case of three turbulence layers and two DMs conjugated to different altitude from the turbulence layers, as Fig. 1.5(a). Even if the tomography perfectly estimates the turbulence layers, it is impossible to provide the perfect correction for all direction by the two DMs. This is known as the generalized fitting error. Increasing the number of DMs is a solution of this problem, but it requires additional optical surfaces, which decreases throughput, and complexity of the control. Another difficulty associated with a MCAO system is the requirement of large DMs to compensate the phase distortions at high altitudes. These difficulties limit the size of FoV size of a MCAO system to the diameter of 1–2 arcminutes, which is smaller than other WFAO concepts.

At this moment, one MCAO system works as a facility instrument for Gemini-South 8 meters telescope, named the *Gemini Multi-conjugated adaptive optics System* (GeMS) [40, 44]. The GeMS computes the tomography by using 5 Na

LGSs and 1–3 TT-NGSs, which measure unseen modes of the LGS, and corrects the phase distortion over the wide FoV more than 1 arcminutes by three DMs conjugated to 0, 4.5, 9 km. Another MCAO system is developed for the Large Binocular Telescope (LBT) [26]. MCAO systems are also designed as first light instruments for future ELTs, for example, NFIRAOS [27] for Thirty Meter Telescope (TMT) and MAORY [14] for European ELT (E-ELT). The NFIRAOS on TMT will do the tomographic wave-front reconstruction using six LGSs and provide the best correction for 30 arcseconds diameter FoV and the mild correction for 2 arcminutes FoV by three DMs.

1.4.2 Multi-Object Adaptive Optics

MOAO system was proposed originally by Hammer et al. [23] and also requires the tomographic wave-front reconstruction. MOAO system provides the optimized correction for multiple small patches in the large FoR of 5–10 arcminutes diameter. As shown in Fig. 1.5(b), there are multiple science pick-off arms on science targets. After each pick-off arm provides the light from the science targets for each science channel, a DM contained in each science channel makes the optimal correction in its science direction. This parallel approach can increase an efficiency of the observation. In addition, since each DM in a MOAO system corrects the phase distortion in one direction, there is no generalized fitting error in MOAO systems, and the size of each DM can be comparable to the size of DM in SCAO systems. Therefore, MOAO systems can realize larger FoR, which is considered 5–10 arcminutes diameter, compared with MCAO systems. The multiplicity of MOAO systems is suited for multi-object observations of galaxies in high redshift universe because these high redshift galaxies have a small apparent angular size and a low number density.

However, MOAO is still considered as very challenging system. The most challenging point of a MOAO system is *open-loop control*. MOAO system corrects the phase distortion in different directions from WFSs and therefore, we need the open-loop control. In the open-loop control, since there is no feedback fed to the WFSs from the DMs, it is required excellent calibration and stability of all DMs and WFSs compared with closed-loop AO systems. Moreover, open-loop WFSs observe the raw phase distortions not corrected by DMs. It means that WFSs with the large dynamical range are required. We have to construct the optical and mechanical design of future MOAO systems with considering how we calibrate and control the system. The complexity of MOAO system is the other challenging

point. Because the FoV of each science path is small and the optical design of each science path can be simple, there can be science channels as many as 10 in future MOAO systems [3, 45]. Therefore, and the number of moving elements, such as DMs and pick-off arms, is much larger than other WFAO concepts.

In order to identify technical readiness and difficulties associated with an MOAO system, there are several projects to develop an MOAO demonstrator and to test it on-sky. Here, we introduce two projects : CANARY [18] for William Herschel Telescope (WHT) of 4.2 meters diameter and RAVEN [32] for Subaru telescope of 8 meters diameter. The CANARY is the first on-sky demonstrator of an MOAO system, which works with three NGSs, four Rayleigh LGSs, and one on-axis science channel in the phase B, and is developed as a pathfinder for EAGLE, which is MOAO system on E-ELT [45]. RAVEN is the first MOAO technical and science demonstrator on 8-m class telescope. RAVEN is developed and tested for the Subaru telescope on Maunakea in Hawaii. RAVEN provides MOAO correction for two science targets simultaneously by using three NGSs and one Na LGS installed in the Subaru telescope. We will explain the system of the RAVEN later.

1.4.3 Ground Layer Adaptive Optics

GLAO system can be considered as a variation of the MCAO system with only one DM conjugated to the ground, as shown in Fig. 1.5(c). As mentioned above, more than half of the atmospheric turbulence are caused in the ground layer. GLAO provides the correction only for the ground layer and improves the seeing rather than achieves near diffraction-limited resolution. The ground layer is a common component to wide range of directions. Therefore, GLAO system provides moderate correction over the wide FoV, which is possibly more than 10 arcminutes diameter. This is useful to survey observations over large field. Mostly, an adaptive secondary mirror is considered as a DM for a GLAO system, then we can perform GLAO correction without any additional optical component. In a GLAO system, a tomographic reconstruction is not necessary since the ground layer turbulence can be computed by averaging measurements from multiple WFSs.

A GLAO system is working in LBT [22], named ARGOS. This is a GLAO system with three Rayleigh LGSs and an adaptive secondary mirror. ARGOS provides 0.3 to 0.4 arcsecond images in J, H and K with GLAO correction from 0.7 to 1 arcsecond uncorrected seeing. Furthermore, other large telescopes plan a GLAO system with adaptive secondary mirror.

	Value
Telescope aperture	30 m
Total system throughput	30 %
Dark	0.006 e^-/pixel/s
Readout	5 e^-/pixel/read
Integration Time	10, 20, and 30 hours
FoR	5, and 10 arcminutes diameter
AO performance	50 % EE
Aperture for EE	50 mas box for point source 300 mas box for extended source
Signal to noise ratio (SNR) for detection	5
Spectral Resolution	3000
Observed wavelength	J-band (1250 nm)

Tab. 1.1: Parameters used in the estimation of the number of detected high redshift LBGs in 1.4.4. The dark count and readout noise is referenced from the TMT IRIS simulation [51].

1.4.4 Importance of Wide Field

The key parameters of WFAO systems are the performance of AO correction and the FoR size. We show the importance of these parameters with respect to multi-object spectroscopy of lyman-break galaxies (LBGs) in high redshift universe, $z > 5$.

From deep imaging surveys by the Hubble Space Telescope (HST), many candidates of galaxies in high redshift universe $z > 5$ are detected by the lyman-break method [7]. It is known that these high redshift LBGs are star-forming galaxies. In order to understand the star formation in the early universe, multi-object spectroscopy of rest-frame UV continuum, emission lines, and absorption lines for large number of high redshift LBGs is required. Such a observation is considered as the main science of a MOAO instrument in the future ELTs [1]. As the low number density of high redshift LBGs, the large FoR is required to maximize the multiplicity of the MOAO for high redshift LBGs.

Here, we estimate the number of high redshift LBGs expected to be detected by a multi-object spectroscopy with a MOAO system on the 30 m aperture telescope and compare the achieved number density with the observed luminosity function. The parameters used in this estimation are summarized in Table 1.1. The total

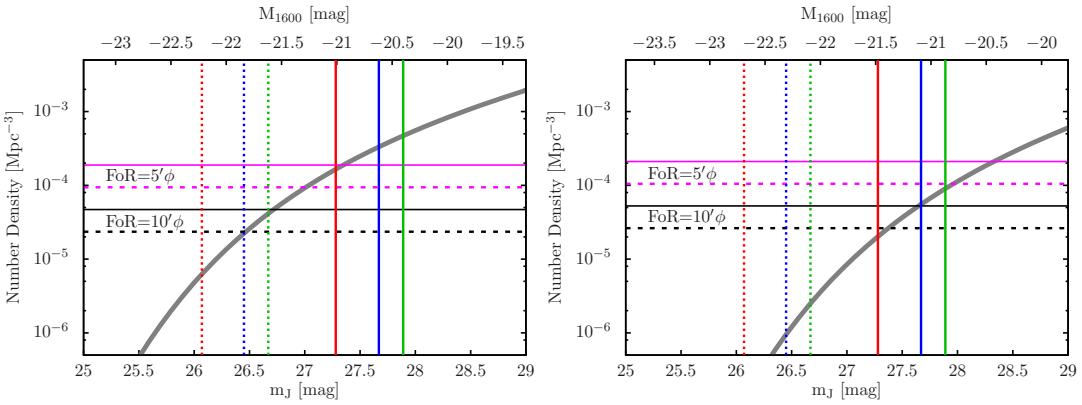

Figure. 1.6: Observed number density and the number density achieved by the multi-object spectroscopy with the future MOAO system at $z \sim 5$ (the left panel) and $z \sim 6$ (the right panel). The gray curve indicates the observed cumulative luminosity function of high redshift LBGs as a function of an apparent magnitude at J-band. The observed luminosity functions are modeled with a Schechter function [7], and the parameters of the Schechter function are $M^*_{UV} = -21.17$, $\phi^* = 0.74 \times 10^{-3}$, and $\alpha = -1.76$ for $z \sim 5$, and $M^*_{UV} = -20.94$, $\phi^* = 0.50 \times 10^{-3}$, and $\alpha = -1.87$ for $z \sim 6$. The redshift range for each redshift is assumed to $4.5 < z < 5.5$ for $z \sim 5$ LBGs and $5.5 < z < 6.5$ for $z \sim 6$. The vertical lines indicate the limit magnitude achieved by the future instrument for the point source (solid) and extended source (dotted) as an integration time of 10 hours (red), 20 hours(blue), and 30 hours (green). The horizontal lines represent the cumulative number density required to detect 10 (solid) and 5 (dotted) LBGs over the FoR of 5 (magenta) and 10 (black) arcminute diameter.

system throughput, including the telescope, the AO system, and the science instrument, is assumed to be 30 %. We consider a point source and an extended source as a intensity profile of LBGs. For the point source, the performance of the MOAO system is assumed to be 50 % EE in a 50 mas box over the FoR. For the extended source, the MOAO performance is 50 % EE in a 300 mas box to maximize the signal to noise ratio (SNR). The background and transmittance of the sky are referenced from the measurement by GEMINI observatory[1]. The dark count and readout noise of the detector are referenced from [51]. The observation is performed at J-band, which is close to the redshifted wavelength of the rest-frame UV continuum. The criteria for the detection is set to SNR=5.

Fig. 1.6 shows a relation between the observed cumulative luminosity function and the number of LBGs detected by the multi-object spectroscopy with the future MOAO system at $z \sim 5$ (the left panel) and $z \sim 6$ (the right panel). The gray curve indicates the observed cumulative luminosity function of high redshift LBGs. The

[1]http://www.gemini.edu/sciops/telescopes-and-sites/observing-condition-constraints/ir-background-spectra

vertical lines indicate the limit magnitude achieved by the future instrument for the point source (solid) and extended source (dotted) as an integration time of 10 hours (red), 20 hours(blue), and 30 hours (green). The horizontal lines represent the cumulative number density required to detect 10 (solid) and 5 (dotted) LBGs over the FoR of 5 (magenta) and 10 (black) arcminute diameter. For example, at $z \sim 5$, an intersection point of the red vertical solid line and the magenta horizontal solid line is above the observed cumulative luminosity function of LBG, and it means that the future instrument can not detect the rest-frame UV continuum of 10 LBGs at $z \sim 5$ within the FoR of 5 arcminutes diameter with a SNR of 5 and an integration time of 10 hours, if the LBGs are point sources. On the contrast, since an intersection point of the red vertical solid line and the black horizontal solid line is below the observed cumulative luminosity function, the rest-frame UV continuum of 10 LBGs at $z \sim 5$ can be detected by the future instrument within the FoR of 10 arcminutes diameter with a SNR of 5 and an integration time of 10 hours. Similarly, if the LBG is extended object, while 5 LBGs can not be detected with a 5 arcminutes FoR and the integration time of 30 hours, it will be possible with a 10 arcminutes FoR. This trend is also seen at $z \sim 6$. These estimates show that in order to maximize the multiplicity for the high redshift LBGs, expanding the FoR without reducing the AO performance is important.

1.5 Tomographic Wave-Front Reconstruction

In this section, we provide more introduction about the tomographic wave-front reconstruction, which is main interest of this thesis. As mentioned in subsection 1.4.4, the key parameters of WFAO systems are the performance of AO correction and the FoR size. The AO performance and the size of FoR depend strongly on the accuracy of the tomographic wave-front reconstruction.

The tomographic wave-front reconstruction has already been demonstrated on sky by some instruments and actually it works on sky[32, 40]. However, the estimation error due to the tomographic wave-front reconstruction causes a significant WFE, called *tomographic error*, and the tomographic error is a one of major error term in WFAO systems. Therefore, improving the tomographic wave-front reconstruction directly results in the enhancement of the WFAO performance.

In this section, we will explain the principle of the tomographic wave-front reconstruction briefly. Then, we will explain the problem associated with the tomographic wave-front reconstruction, which limits the the performance and the

FoR size of WFAO system. Finally, we will explain the computational complexity, which is the other challenging point especially for future ELT-scale WFAO systems.

1.5.1 Tomography Step and Fitting Step

The goal of the tomographic wave-front reconstruction is reconstructing a three-dimensional structure of the phase distortion due to the atmospheric turbulence and computing the shapes (or commands) of DMs from the reconstructed phase distortion. The first part of the tomographic reconstruction is often referred to as a *tomography step* and the second part is a *fitting step*.

The measurements from multiples WFSs contain the information of the phase distortion in corresponding GS directions. In order to overcome the angular anisoplanatism, we have to consider the optical path difference at high altitude depending on the direction. This is achieved by converting the measurements from WFSs, which probes the phase distortion in each direction, into the phase distortion at each altitudes using the tomographic technique. In the case of SH-WFSs, this process is equal to solving an inverse problem for a linear equation between the measurements from SH-WFSs and the phase distortion due to the atmospheric turbulence as

$$\boldsymbol{s} = \boldsymbol{H}\boldsymbol{\phi} + \boldsymbol{\eta} \tag{1.23}$$

where $\boldsymbol{s}$ and $\boldsymbol{\eta}$ are a vector of the measurements and measurement noises of multiple SH-WFSs, $\boldsymbol{\phi}$ is a vector of phase values on a discrete grid of points on the atmospheric turbulence layers, and $\boldsymbol{H}$ is an influence matrix between measurement $\boldsymbol{s}$ and the phase distortion $\boldsymbol{\phi}$. The influence matrix $\boldsymbol{H}$ is created based on the GSs direction, the altitudes and strengths of the atmospheric turbulence layers, and SH-WFS parameters. The altitudes and strengths of the atmospheric turbulence layers vary with time. Therefore, it is required to measure these information during observation and update the influence matrix H to optimize the performance of the tomographic wave-front reconstruction.

The fitting step depends on with the WFAO concepts. In MCAO system, the correction is performed by the series of DMs, which conjugated at different altitudes. The commands of DMs are determined to provide the uniform correction over the FoV. On the other hand, in MOAO system, the phase at each DM-plane is optimized for each direction and the fitting step is performed for each DMs in parallel.

In a simple case, these steps are performed with one matrix-vector multiplication as $\boldsymbol{u}(t) = \boldsymbol{E}\boldsymbol{s}(t)$, where $\boldsymbol{u}$ is a vector of the commands of DMs and $\boldsymbol{E}$ is a matrix performing the tomography step and the fitting step. The matrix $\boldsymbol{E}$ is called *reconstructor* or *reconstruction matrix*. With following the update of the influence matrix H, the reconstruction matrix $\boldsymbol{E}$ needs to be updated.

1.5.2 Lack of Information in Tomographic Reconstruction

The performance of the tomographic wave-front reconstruction depends strongly on the number of GSs. However, the number of GS is limited in astronomical AO systems. From the limited number of GSs, we can not get information of the phase distortion in a volume of the atmosphere corresponding to the FoR from the WFS measurements. This *lack of information* limits the performance of the tomographic wave-front reconstruction and also makes it difficult to expand the FoR size of WFAO systems.

Fig. 1.7 shows the schematic view of this problem. There are three turbulence layers and three GSs. The footprints of the optical path of GSs on the turbulence layers are indicated with orange circles. In the figure, the some parts of turbulence layers are not covered by the GS optical paths. Namely, we can not get information of the phase distortion of this *uncovered area* from WFSs. The *uncovered area* causes a significant tomographic error mostly on the outer area of the FoR. This is one of the lack of information in the tomography.

The other lack of information is caused by the area referred to as *unoverlapped area*. In Fig. 1.7, most of area on the atmospheric turbulence at high altitude is covered by only one GS optical path. The WFSs probes the integrated phase distortion in its GS direction. In other words, the phase distortions from multiple turbulence layers are *degenerated* in the WFS measurement. In order to solve this degeneracy and reconstruct the phase distortion on each atmospheric turbulence screens by the tomographic wave-front reconstruction, the information from multiple directions is necessary, that is, all areas should be covered by two or more GS optical paths. This degeneracy due to the *unoverlapped area* results in a significant tomographic error even in the direction within the GS asterism.

In particular, the tomographic error due to these areas becomes more severe when one considers to expand a FoR of WFAO systems with the wide configuration of GSs. In addition, using LGS increases the geometric error compared with using NGS due to its conical optical path. This means that the tomographic error will

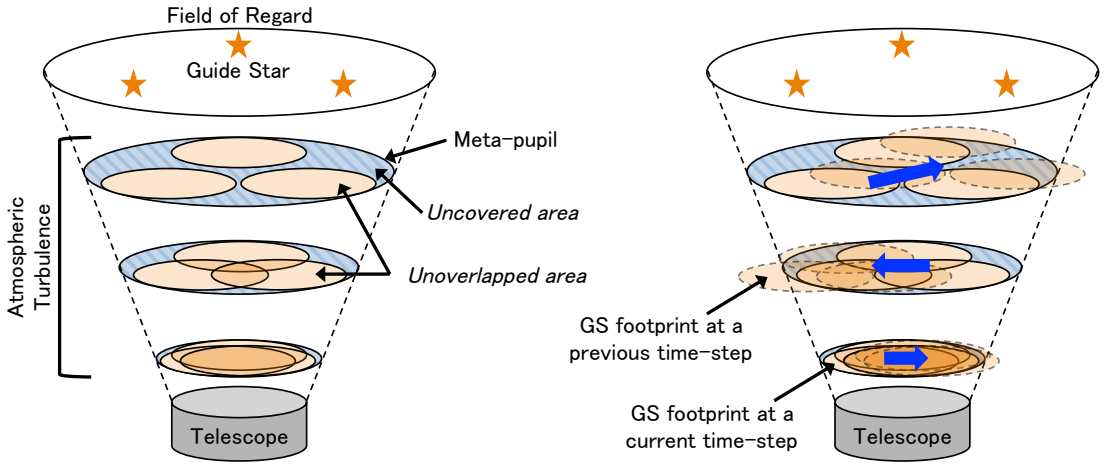

Figure. 1.7: Geometric relation between positions of GSs and regions in the atmosphere measured by WFSs. Left: The solid orange circles show the footprint of GS optical paths at the current time-step. There are areas covered by no or only one GS, referred to as *uncovered area* or *unoverlapped area*. These areas cause significant tomographic errors. Right: The blue arrows indicate wind direction at each altitude. The GS footprints measured at a previous time-step move due to the wind with time, which are dashed orange circles in the figure.

be more severe in WFAO systems for the future ELT with multiple LGSs because the cone effect gets larger with increasing the size of aperture.

Some approaches are proposed to overcome this issue[2, 11]. These methods are based on the frozen flow hypothesis. Under the frozen flow assumption, the time evolution of the atmospheric turbulence can be computed as the shift due to the wind. In this case, as shown in the right panel of Fig. 1.7, the areas in the atmospheric turbulence measured at previous time-steps also moves with time. This means that the estimation and the measurement at previous time-steps can be considered as the information of displaced areas at the current time-step. Ammons et al. [2] propose the multi-layer shift-and-average technique. They averaged the reconstructed phase distortions over multiple time-steps for each turbulence layer with considering the shift due to the wind. Their method can reduce the tomographic error due to the *uncovered* and *unoverlapped* areas successfully in the numerical simulation. Moreover, predictive linear quadratic gaussian (LQG) control probably can reduce the tomographic error due to the lack of information[11]. The predictive LQG is proposed mainly for reducing the time lag error. In the LQG control, the estimations at multiple time-steps are integrated. Therefore, the LQG may works not only for the time lag error, but also for the tomographic error due to the lack of information.

However, It is noted that in the methods above, an estimate at each time-step is already affected by *uncovered* and *unoverlapped* areas. In order to solve the lack of information directly, we should use information from multiple time-steps in the tomographic reconstruction, not after the tomographic reconstruction such as the multi-layer shift-and-average technique and the LQG.

Estimating wind speeds and directions at different altitudes is essential for our tomography method. Several methods to estimate wind speeds and directions from measurements of Shack Hartmann WFS (SH-WFS) are proposed and tested by using on-sky measurements[21, 42]. These methods successfully detect the wind at multiple altitudes and start to be applied to the real-time operation.

1.5.3 Computation Complexity

The computation complexity of the tomographic reconstruction is the other problem especially for future ELT-scale WFAO system. For the real-time compensation of the phase distortion, we have to compute the tomographic reconstruction within 1 ms as mentioned in 1.3.1. Furthermore, the tomographic reconstructor should be updated every from a few ten seconds to a few minutes to follow the change of atmospheric condition.

For example, consider MOAO systems on a current large telescope with 8 m diameter and a future ELT with 30 m diameter. The number of GSs and science channels are assumed to be 5 and 10, respectively. The size of subapertures of SH-WFSs and elements of DMs are 0.5 m, that is, there are $16times16$ subapertures in a SH-WFS and 16×16 elements in a DM for the MOAO system on the current MOAO system and there are 60×60 subapertures and elements for the future MOAO system. The total number of measurements from 5 SH-WFSs is 2560 and 36000, respectively, where it is noted that each subaperture measures local gradients along x and y direction. The total number of estimates of the tomographic reconstruction, i.e. the number of elements of 10 DMs, is 2560 and 36000, respectively. The size of the tomographic reconstructor for the future ELT-scale MOAO system is roughly 200 time larger than the size for the MOAO system for the current large telescopes. The complexity for computing the tomographic reconstructor with simply inversing the influence matrix, $\boldsymbol{H}$, scales as $O(n^3)$, where n is a dimension of the reconstructor matrix. Also, the complexity of the matrix-vector multiplication for the tomographic reconstruction scales $O(n^2)$. Thus, the complexity of the tomographic reconstruction increase largely with the size of the aperture. In the ELT-scale WFAO systems, we can not achieve the

required control speeds with the standard computation method. Therefore, more efficient methods are required.

There are a lot of effort to reduce the computation time of the ELT-scale tomographic reconstruction. In the ELT-scale tomographic reconstruction, we can not compute the tomographic reconstructor directly because it is too large. Therefore, the iterative methods, such as a conjugate gradient method, are proposed, which solves the inverse problem for the tomographic reconstruction iteratively at every time-step. Ellerbroek [15] proposed the sparse matrix technique, which uses the sparseness of the matrix and can reduce the computation time of the matrix-vector multiplication. The most of matrices in the tomographic reconstruction are known as a sparse matrix, and therefore, the sparse technique allows us to reduce the computation time for the iterative method. Also, the conjugate gradient method with an efficient preconditioning technique [49] and a warm start technique [36] is proposed to reduce the number of iterations. Recently, the distributed Kalman filter is developed as a fast non-iterative spatially invariant controller [38]. In addition, the general purpose computing on GPU (GPGPU) can be powerful computing engines of those algorithms.

1.6 Object of This Thesis

In this work, we will develop a new algorithm for the tomographic wave-front reconstruction, which reduces the tomographic error due to the lack of information and to extend the size of FoR of WFAO systems without reducing the AO performance, and the method to estimate wind speeds and directions at multiple altitudes, which is essential for the new tomography algorithm. The basic idea of the new tomographic reconstruction algorithm is to solve the tomographic wave-front reconstruction by using measurement from multi time-steps based on the frozen flow assumption. The main goal is to demonstrate and evaluate the performance of the new tomographic reconstruction by analytical method, numerical simulation, laboratory test, and on-sky observation. Also, we will discuss the GPGPU capability for the future-ELT scale tomographic reconstruction.

Chapter 2

Methodology

2.1 Tomographic Wave-Front Reconstruction

Fig. 2.1 shows a schematic of geometry for a MOAO system with multiple LGSs and SH-WFSs. The goal of tomographic reconstruction is reconstructing DM commands of each science direction from the measurements of multiple SH-WFSs. We consider that the atmospheric turbulence consists of N_{layer} thin layers located at different altitudes. The tomography is computed from N_{lgs} LGSs for N_{obj} science objects. The directions of each LGS and each science target are indexed by $\boldsymbol{\alpha} = (\alpha_x, \alpha_y)$ and $\boldsymbol{\beta} = (\beta_x, \beta_y)$, respectively. The command, or voltage, provided to the elements of DM for kth science object is indicated by a column vector $\boldsymbol{u}_{\boldsymbol{\beta_k}}$.

In the near-field approximation, the phase distortion of the aperture-plane wave-front $\varphi_{\boldsymbol{\theta}}(\boldsymbol{x}, t)$ in the science target direction $\boldsymbol{\beta_k}$ at time t is represented as the sum of the phase distortion caused by the turbulence layers,

$$\varphi_{\boldsymbol{\beta_k}}(\boldsymbol{x}, t) = \sum_{i=1}^{N_{\text{layer}}} \phi_i(\boldsymbol{x} + h_i \boldsymbol{\beta_k}, t), \tag{2.1}$$

where $\boldsymbol{x}$ is two-dimensional spatial coordinate vector $\boldsymbol{x} = (x, y)$, h_i is an altitude of ith turbulence layer, and $\phi(\boldsymbol{x}, t)$ is a phase distortion at a point $\boldsymbol{x}$ on ith turbulence layer at time t. In the case of LGS in direction $\boldsymbol{\alpha_j}$ at altitude h_{Na}, the scaling of the optical footprint at high altitudes due to the cone effect should be considered as

$$\varphi_{\boldsymbol{\alpha_j}}(\boldsymbol{x}, t) = \sum_{i=1}^{N_{\text{layer}}} \phi_i \left(\boldsymbol{x} \frac{h_{\text{Na}} - h_i}{h_{\text{Na}}} + h_i \boldsymbol{\alpha_j}, t \right). \tag{2.2}$$

In the later discussion, wave-fronts and turbulence layers are discretized spatially and denoted by column vectors, this is, $\boldsymbol{\varphi}(t)$ for wave-fronts and $\boldsymbol{\phi}(t)$ for

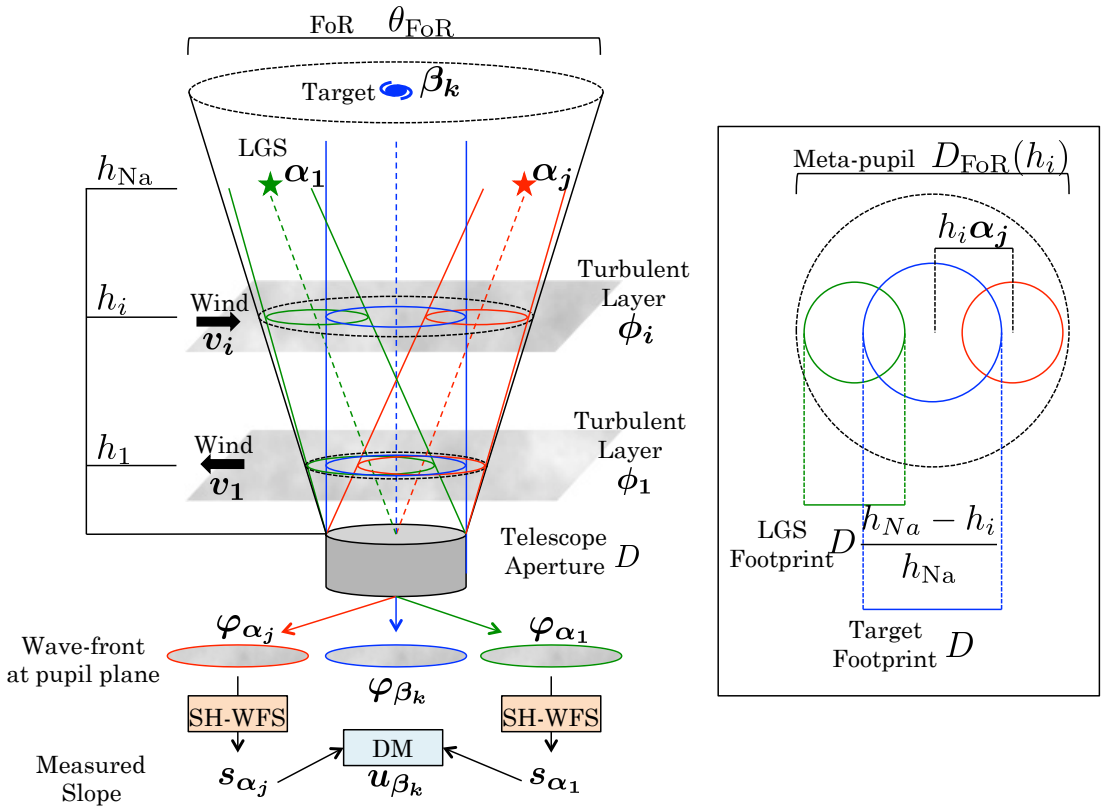

Figure. 2.1: Image of a MOAO model with multiple turbulence screens, LGSs, and SH-WFSs. $\boldsymbol{\beta}$ and $\boldsymbol{\alpha}$ indicate directions of science targets and LGSs. The index i, j, k is used for the turbulence screens, LGSs and SH-WFSs, and science targets and DMs, respectively. The goal of the tomographic reconstruction is to estimate DM command $\boldsymbol{u_\beta}$ from the measured slope $\boldsymbol{s_\alpha}$.

turbulence layers. We define a ray-tracing matrix $\boldsymbol{P}^{\boldsymbol{i}}_{\boldsymbol{\theta}}$, which extracts phase distortion within a optical path footprint in the direction $\boldsymbol{\theta}$ from i-th atmospheric turbulence by using a bilinear interpolation. Using the ray-tracing matrix, Eq. (2.1) and Eq. (2.2) are rewritten with considering all phase points in the aperture as

$$\boldsymbol{\varphi_{\beta_k}}(t) = \sum_{i=1}^{N_{\mathrm{layer}}} \boldsymbol{P}^{\boldsymbol{i}}_{\boldsymbol{\beta_k}} \boldsymbol{\phi_i}(t) = \boldsymbol{P_{\beta_k}} \boldsymbol{\phi}(t), \tag{2.3}$$

$$\boldsymbol{\varphi_{\alpha_j}}(t) = \sum_{i=1}^{N_{\mathrm{layer}}} \boldsymbol{P}^{\boldsymbol{i}}_{\boldsymbol{\alpha_j}} \boldsymbol{\phi_i}(t) = \boldsymbol{P_{\alpha_j}} \boldsymbol{\phi}(t), \tag{2.4}$$

where $\boldsymbol{P}^{\boldsymbol{i}}_{\boldsymbol{\alpha_j}}$ is a ray-tracing matrix including the scaling effect due to the cone effect, $\boldsymbol{\phi}(t) = [\boldsymbol{\phi}^T_{\mathbf{1}}(t) \cdots \boldsymbol{\phi}^T_{\boldsymbol{N}_{\mathrm{layer}}}(t)]^T$, and $\boldsymbol{P_{\beta_k}}$ and $\boldsymbol{P_{\alpha_k}}$ are a concatenation of all submatrices $\boldsymbol{P}^{\boldsymbol{i}}_{\boldsymbol{\beta_k}}$ and $\boldsymbol{P}^{\boldsymbol{i}}_{\boldsymbol{\beta_k}}$, respectively.

We define the relation between the DM commands reconstructed by the tomography and the wave-front made by the DM for kth science direction as

$$\hat{\boldsymbol{\varphi}}_{\boldsymbol{\beta_k}}(t) = \boldsymbol{N}_{\boldsymbol{\beta_k}} \hat{\boldsymbol{u}}_{\boldsymbol{\beta_k}}(t) \tag{2.5}$$

where the hat symbol indicates estimated quantities and $\boldsymbol{N}_{\boldsymbol{\beta_k}}$ is a interaction matrix for kth DM. The interaction matrix is determined experimentally.

The phase variance of the aperture-plane residual wave-front for science direction $\boldsymbol{\beta_k}$ is defined as

$$\epsilon_{\beta_k} = \langle ||\boldsymbol{\varphi}_{\boldsymbol{\beta_k}} - \hat{\boldsymbol{\varphi}}_{\boldsymbol{\beta_k}}||^2 \rangle. \tag{2.6}$$

In MOAO system, a tomographic reconstructor is determined to minimize the residual phase variance ϵ_{β_k} [10],

$$\boldsymbol{E}_{\boldsymbol{\beta_k}} = \underset{\boldsymbol{E}_{\boldsymbol{\beta_k}}}{\operatorname{argmin}}\ \epsilon_{\beta_k}, \tag{2.7}$$

where $\boldsymbol{E}_{\boldsymbol{\beta_k}}$ is the tomographic reconstructor for the direction $\boldsymbol{\beta_k}$ and $\langle\rangle$ indicates ensemble average over time. This reconstructor is known as *minimum variance reconstructor* [15], which provides the solution to minimize the variance of the residual phase at on aperture-plane. The DM commands $\boldsymbol{u}_{\boldsymbol{\beta_k}}$ is reconstructed from the measurements $\boldsymbol{s}_{\boldsymbol{\alpha}}$ by the reconstructor $\boldsymbol{E}_{\boldsymbol{\beta_k}}$ as $\boldsymbol{u}_{\boldsymbol{\beta_k}} = \boldsymbol{E}_{\boldsymbol{\beta_k}} \boldsymbol{s}_{\boldsymbol{\alpha}}$.

2.1.1 Measurement Model

The slope $\boldsymbol{s}_{\boldsymbol{\alpha_j}}(t)$ measured by the j-th SH-WFS aiming the direction $\boldsymbol{\alpha_j}$ at time t is defined as

$$\boldsymbol{s}_{\boldsymbol{\alpha_j}}(t) = \boldsymbol{\Gamma}_{\boldsymbol{\alpha_j}} \boldsymbol{\varphi}_{\boldsymbol{\alpha_k}}(t) + \boldsymbol{\eta_j}(t) = \boldsymbol{\Gamma}_{\boldsymbol{\alpha_j}} \boldsymbol{P}_{\boldsymbol{\alpha_j}} \boldsymbol{\phi}(t) + \boldsymbol{\eta_j}(t), \tag{2.8}$$

where $\boldsymbol{\Gamma}_{\boldsymbol{\alpha_j}}$ is a discrete phase-to-slope operator which converts phases into slopes and $\boldsymbol{\eta_j}(t)$ is a column vector of the noise in measurements of j-th SH-WFS.

We use Fried geometry to define $\boldsymbol{\Gamma}_{\boldsymbol{\alpha_j}}$. In the Fried geometry, slopes for x and y direction in a subaperture are defined by surrounding 4 phase points (Fig. 2.2) as

$$\begin{pmatrix} s^x_{i,j} \\ s^y_{i,j} \end{pmatrix} = \frac{1}{2d_{\mathrm{sa}}} \begin{pmatrix} -1 & 1 & -1 & 1 \\ -1 & -1 & 1 & 1 \end{pmatrix} \begin{pmatrix} \varphi_{i,j} \\ \varphi_{i+1,j} \\ \varphi_{i,j+1} \\ \varphi_{i+1,j+1} \end{pmatrix} \tag{2.9}$$

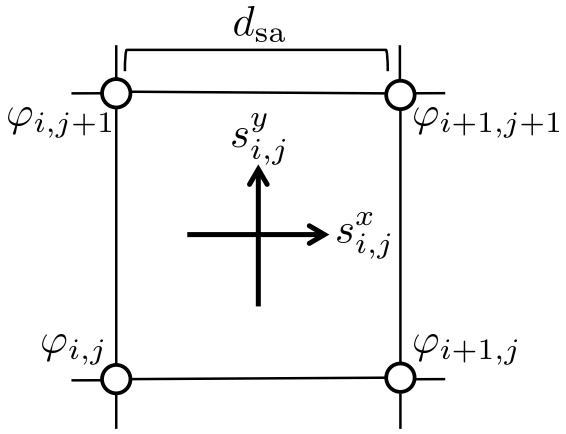

Figure. 2.2: Fried geometry to define slopes for SH-WFS.

where $\varphi_{i,j}$ and $s^{x(y)}_{i,j}$ are a phase value and $x(y)$-slope at a discrete point indexed i and j. Eq. (2.8) is concatenation of Eq. (2.9) for all subapertures.

Concatenating Eq. (2.8) of N_{lgs} SH-WFSs, we can obtain a equation connecting the phase distortion on N_{layer} atmospheric layers and the slope provided by N_{lgs} SH-WFSs as follows.

$$\boldsymbol{s}_{\boldsymbol{\alpha}}(t) = \begin{bmatrix} \boldsymbol{s}_{\boldsymbol{\alpha_1}}(t) \\ \vdots \\ \boldsymbol{s}_{\boldsymbol{\alpha}_{\boldsymbol{N}_{\mathrm{lgs}}}}(t) \end{bmatrix} = \boldsymbol{\Gamma}_{\boldsymbol{\alpha}} \boldsymbol{P}_{\boldsymbol{\alpha}} \boldsymbol{\phi}(t) + \boldsymbol{\eta}(t) \tag{2.10}$$

where $\boldsymbol{\Gamma}_{\boldsymbol{\alpha}}$ is a block diagonal matrix, $\boldsymbol{\Gamma}_{\boldsymbol{\alpha}} = \mathbf{diag}[\boldsymbol{\Gamma}_{\boldsymbol{\alpha_1}}, \cdots, \boldsymbol{\Gamma}_{\boldsymbol{\alpha}_{\boldsymbol{N}_{\mathrm{lgs}}}}]$, $\boldsymbol{P}_{\boldsymbol{\alpha}}$ is a ray-tracing matrix concatenating $\boldsymbol{P}_{\boldsymbol{\alpha}_{\boldsymbol{j}}}$ for $1 \leq j \leq N_{\mathrm{lgs}}$, and $\boldsymbol{\eta}(t)$ is a column vector including measurement noises from all SH-WFSs.

2.1.2 Minimum Variance Reconstructor

The minimum variance reconstructor can be obtained by minimising Eq. (2.6). As shown in Appendix A.1 , the final formula is given as

$$\begin{aligned} \boldsymbol{E}_{\boldsymbol{\beta_k}} =& (\boldsymbol{N}^T_{\boldsymbol{\beta_k}} \boldsymbol{N}_{\boldsymbol{\beta_k}})^{-1} \boldsymbol{N}^T_{\boldsymbol{\beta_k}} \boldsymbol{P}_{\boldsymbol{\beta_k}} (\boldsymbol{P}^T_{\boldsymbol{\alpha}} \boldsymbol{\Gamma}^T_{\boldsymbol{\alpha}} \boldsymbol{\Sigma}^{-1}_{\boldsymbol{\eta\eta}} \boldsymbol{\Gamma}_{\boldsymbol{\alpha}} \boldsymbol{P}_{\boldsymbol{\alpha}} - \boldsymbol{\Sigma}^{-1}_{\boldsymbol{\phi\phi}})^{-1} \boldsymbol{P}^T_{\boldsymbol{\alpha}} \boldsymbol{\Gamma}^T_{\boldsymbol{\alpha}} \boldsymbol{\Sigma}^{-1}_{\boldsymbol{\eta\eta}} && (2.11) \\ =& \boldsymbol{F}_{\boldsymbol{\beta_k}} \boldsymbol{E}_{\boldsymbol{\phi}}. && (2.12) \end{aligned}$$

where $\boldsymbol{\Sigma}_{\boldsymbol{\eta\eta}}$ is a noise covariance matrix, $\boldsymbol{\Sigma}_{\boldsymbol{\phi\phi}}$ is a covariance matrix of the phase distortion of the atmospheric turbulence, $\boldsymbol{E}_{\boldsymbol{\phi}}$ is a *estimation matrix*, and $\boldsymbol{F}_{\boldsymbol{\beta_k}}$ is a *fitting matrix*. If it is assumed that the measurement noise from jth WFS is zero-mean gaussian noise with a variance of $\sigma^2_{\eta,j}$ and noises of all WFS subapertures are independent of each other, the noise covariance matrix becomes a block diagonal

matrix as $\boldsymbol{\Sigma_{\eta\eta}} = \mathbf{diag}[\sigma^2_{\eta,1}\boldsymbol{I}, \cdots, \sigma^2_{\eta,N_{\text{lgs}}}\boldsymbol{I}]$. Furthermore, under the assumption that all WFSs have same noise with a variance σ^2_η, the noise covariance matrix becomes $\boldsymbol{\Sigma_{\eta\eta}} = \sigma^2_\eta \boldsymbol{I}$ and the estimation matrix $\boldsymbol{E_\phi}$ can be rewritten as

$$\boldsymbol{E_\phi} = (\boldsymbol{P_\alpha^T \Gamma_\alpha^T \Gamma_\alpha P_\alpha} + \sigma^2_\eta \boldsymbol{\Sigma^{-1}_{\phi\phi}})^{-1} \boldsymbol{P_\alpha^T \Gamma_\alpha^T}. \tag{2.13}$$

Then, the DM commands for science direction $\boldsymbol{\beta_k}(t)$ is reconstructed from measurements as $\hat{\boldsymbol{u}}_{\boldsymbol{\beta_k}}(t) = \boldsymbol{E_{\beta_k} s_\alpha}(t) = \boldsymbol{F_{\beta_k} E_\phi s_\alpha}(t)$.

The term of $\sigma^2_\eta \boldsymbol{\Sigma^{-1}_{\phi\phi}}$ works as a regularization matrix, which smooths the tomographic errors of high spatial frequencies due to the measurement noise. The effect of the regularization matrix is scaled by the balance between the measurement noise σ^2_η and the turbulence power C^2_N. The phase covariance $\Sigma_{\phi\phi}$ can be computed based on the turbulence powers, altitudes, and the Kolmogorov or the von Karman power spectra, and is a block diagonal matrix including the phase covariance matrix at each altitude as $\Sigma_{\phi\phi} = \mathbf{diag}[\Sigma_{\phi\phi,1}, \cdots, \Sigma_{\phi\phi,N_{\text{layer}}}]$.

This reconstructor is constructed based on the model of the turbulence structure and SH-WFSs, which is known as *model-based reconstructor*. The turbulence altitude, C^2_N values, measurement noise are required to create the model-based reconstructor. We will explain the method to estimate the C^2_N profile in . In addition, the DM commands is estimated from the measured slopes at one time-step by this reconstructor. Therefore, $\boldsymbol{E_{\beta_k}}$ is referred to as *single time-step tomographic reconstruction* in the remainder of this thesis.

2.1.3 Discrete Laplacian Approximation

As mentioned, the off-line and on-line computation complexity of the tomographic reconstructor is one of the problem for the future ELT-scale WFAO systems. The sparse matrix technique can reduce the complexity. However, the phase covariance matrix $\boldsymbol{\Sigma_{\phi\phi}}$ is a dense matrix and can not be incorporated into the sparse matrix computation.

The sparse approximation is proposed by Ellerbroek [15], which assumes the turbulence follows $\kappa^{11/3} \approx \kappa^4$. Under the approximation, the inverse of the phase covariance matrix for ith turbulence layer can be rewritten by using Laplacian or curvature operator as

$$\boldsymbol{\Sigma^{-1}_{\phi\phi,i}} \approx \boldsymbol{L_i^T L_i} = c_i^2 \boldsymbol{\bar{L}_i^T \bar{L}_i} \tag{2.14}$$

where $\boldsymbol{\bar{L}_i}$ is a discrete normalized Laplacian matrix, c_i is a scaling constant for $\boldsymbol{\bar{L}_i}$, and $\boldsymbol{L_i} = c_i \boldsymbol{\bar{L}_i}$. The derivation of the scaling constant is given in Appendix A.2

based on [20]. The discrete Laplacian for all turbulence layers is a block diagonal matrix similar to $\Sigma_{\phi\phi}$.

While this approximated regularization matrix is fully sparse and can be incorporated into efficient sparse-matrix techniques, it is known that the approximated matrix does not regularize tip-tilt modes and other modes that are curvature-free[35]. The unregularized modes, mainly tip-tilt modes, may affect the tomographic error especially in the case with LGSs, where tip-tilt modes can not be measured by LGS.

2.1.4 Multi Time-Step Tomographic Wave-Front Reconstruction

In this section, we will introduce our idea to reduce the tomographic error due to the *uncovered* and *unoverlapped areas* by increasing information of the atmospheric turbulence using the measurements at both of the previous and the current time-steps simultaneously. As mentioned in Chapter 1, the frozen flow assumption allows us to consider the evolution of the atmospheric turbulence as the movements of the turbulence layers due to the winds. Under this assumption, it can be considered that the areas measured by WFSs at a previous time-step shift due to the wind with time, which is indicated in Fig. 1.7. Thanks to the spatial displacement due to the wind, the areas corresponding to the measurements at the previous time-step cover the *uncovered* and the *unoverlapped areas* at the current time-step. An important point is using multi time-step measurements in the tomography.

If an atmospheric turbulence layer moves with a constant speed $\boldsymbol{v} = (v_x, v_y)$, the movement of the phase distortion pattern with a position x at Δt previous time-step is written by

$$\phi(\boldsymbol{x}, t - \Delta t) = \phi(\boldsymbol{x} + \boldsymbol{v}\Delta t, t). \tag{2.15}$$

Using Eq. (2.15), we can rewrite Eq. (2.2) and Eq. (2.4) into equations between the aperture-plane wave-front at the previous time-step $t-\Delta t$ and the phase distortion due to the turbulence layers at the current time-step t as

$$\varphi_{\boldsymbol{\alpha_j}}(\boldsymbol{x}, t - \Delta t) = \sum_{i=1}^{N_{\text{layer}}} \phi_i \left(\boldsymbol{x} \frac{h_{\text{Na}} - h_i}{h_{\text{Na}}} + h_i \boldsymbol{\alpha_j} + \boldsymbol{v_i} \Delta t, t \right), \tag{2.16}$$

$$\boldsymbol{\varphi}_{\boldsymbol{\alpha_j}}(t - \Delta t) = \boldsymbol{P}_{\boldsymbol{\alpha_j}}^{\boldsymbol{\Delta t}} \boldsymbol{\phi}(t), \tag{2.17}$$

where $\boldsymbol{P}_{\boldsymbol{\alpha}_j}^{\boldsymbol{\Delta t}}$ is a ray-tracing matrix considering the movement of the phase distortion pattern within the optical path footprint of LGS in direction $\boldsymbol{\alpha_j}$ during the duration time Δt. Similarly, using Eq. (2.17) allows us to create a measurement model connecting measurements at the previous time-step $(t-\Delta t)$ with the phase distortion due to the atmospheric turbulence at current time-step t,

$$\boldsymbol{s}_{\boldsymbol{\alpha}}(t) = \boldsymbol{\Gamma}_{\boldsymbol{\alpha}} \boldsymbol{P}_{\boldsymbol{\alpha}}^{\boldsymbol{\Delta t}} \boldsymbol{\phi}(t) + \boldsymbol{\eta}(t) \tag{2.18}$$

where, $\boldsymbol{P}_{\boldsymbol{\alpha}}^{\boldsymbol{\Delta t}}$ is a concatenation of all submatrices $\boldsymbol{P}_{\boldsymbol{\alpha}_j}^{\boldsymbol{\Delta t}}$ for $j = 1, \ldots, N_{\text{lgs}}$.

In order to use the measurements from both of the current and previous time-steps simultaneously to increase information and to improve the performance of the tomography, the final measurement model is a concatenation of Eq. (2.10) and Eq. (2.18). The reconstructor can be given as well as the single time-step reconstructor.

$$\tilde{\boldsymbol{E}}_{\boldsymbol{\beta}_k(\boldsymbol{\Delta t})} = \boldsymbol{F}_{\boldsymbol{\beta}_k} (\tilde{\boldsymbol{P}}_{\boldsymbol{\alpha}(\boldsymbol{\Delta t})}^T \tilde{\boldsymbol{\Gamma}}_{\boldsymbol{\alpha}(\boldsymbol{\Delta t})}^T \tilde{\boldsymbol{\Sigma}}_{\boldsymbol{\eta\eta}(\boldsymbol{\Delta t})}^{-1} \tilde{\boldsymbol{\Gamma}}_{\boldsymbol{\alpha}(\boldsymbol{\Delta t})} \tilde{\boldsymbol{P}}_{\boldsymbol{\alpha}(\boldsymbol{\Delta t})} + \boldsymbol{L}^T \boldsymbol{L})^{-1} \tilde{\boldsymbol{P}}_{\boldsymbol{\alpha}(\boldsymbol{\Delta t})}^T \tilde{\boldsymbol{\Gamma}}_{\boldsymbol{\alpha}(\boldsymbol{\Delta t})}^T \tilde{\boldsymbol{\Sigma}}_{\boldsymbol{\eta\eta}(\boldsymbol{\Delta t})}^{-1} \tag{2.19}$$

$$= \boldsymbol{F}_{\boldsymbol{\beta}_k} \tilde{\boldsymbol{E}}_{\boldsymbol{\phi}(\boldsymbol{\Delta t})} \tag{2.20}$$

where

$$\tilde{\boldsymbol{P}}_{\boldsymbol{\alpha}(\boldsymbol{\Delta t})} = \begin{bmatrix} \boldsymbol{P}_{\boldsymbol{\alpha}} \\ \boldsymbol{P}_{\boldsymbol{\alpha}}^{\boldsymbol{\Delta t}} \end{bmatrix}, \quad \tilde{\boldsymbol{\Gamma}}_{\boldsymbol{\alpha}(\boldsymbol{\Delta t})} = \begin{bmatrix} \boldsymbol{\Gamma}_{\boldsymbol{\alpha}} & \boldsymbol{0} \\ \boldsymbol{0} & \boldsymbol{\Gamma}_{\boldsymbol{\alpha}} \end{bmatrix}, \quad \tilde{\boldsymbol{\Sigma}}_{\boldsymbol{\eta}(\boldsymbol{\Delta t})} = \begin{bmatrix} \boldsymbol{\Sigma}_{\boldsymbol{\eta\eta}} & \boldsymbol{0} \\ \boldsymbol{0} & \boldsymbol{\Sigma}_{\boldsymbol{\eta\eta}} \end{bmatrix}. \tag{2.21}$$

The wave-front in the science direction is derived from the measurements at the current and the previous time-step as $\hat{\boldsymbol{\varphi}}_{\boldsymbol{\beta}_k}(t) = \tilde{\boldsymbol{E}}_{\boldsymbol{\beta}_k(\boldsymbol{\Delta t})} \tilde{\boldsymbol{s}}_{\boldsymbol{\alpha}(\boldsymbol{\Delta t})}(t)$, in which $\tilde{\boldsymbol{s}}_{\boldsymbol{\alpha}(\boldsymbol{\Delta t})}(t) = [\boldsymbol{s}_{\boldsymbol{\alpha}}(t)^T \ \boldsymbol{s}_{\boldsymbol{\alpha}}(t-\Delta t)^T]^T$. We refer to this reconstructor as ***multi time-step tomographic reconstruction***. Although the multi time-step reconstructor $\tilde{\boldsymbol{E}}_{\boldsymbol{\beta}_k(\boldsymbol{\Delta t})}$ uses measurements only from two time-steps, it is easily to expand the reconstructor to use multi time-step measurements more than two time-step, for example, $\tilde{\boldsymbol{E}}_{\boldsymbol{\beta}_k(\boldsymbol{\Delta t_1}, \boldsymbol{\Delta t_2}, \ldots, \boldsymbol{\Delta t_n})}$. The wind speed and direction at each altitude should be measured before the reconstruction. We will discuss the method to estimate the wind speed and direction at each altitude in .

2.1.5 Time Difference Δt

The time difference between the current and the previous time steps, Δt, is an important parameter for the multi time-step reconstructor. Although we assume

the frozen flow assumption, in reality, the time scale in which the frozen flow assumption is valid is limited. In order to improve the performance of the tomographic reconstruction by the multi time-step reconstructor, Δt should be chosen to be shorter than the time scale within which the frozen flow assumption holds. There are several studies to investigate the time scale of the frozen flow. Schöck et al. [46] investigated the temporal decay of the intensity of the auto-correlation of the WFS slope measured on sky, and found that a value t_{50}, which is the times for which the cumulative auto-correlation decreases to 50 % of its initial value, is of order of 50–100 ms. If we use this time scale, t_{50}, as an index for Δt, Δt should be equal to or shorter than t_{50}. However, it is noted that it is not clear how the decay ratio of the auto-correlation and t_{50} relate to the performance of the multi time-step reconstructor. Also, the result from Schöck et al. consider the total auto-correlation decay and they did not investigate the temporal decay of each turbulence screen. In order to understand the effect of the frozen flow assumption, more on-sky experiments are required. We will discuss the influence of the frozen flow assumption on the multi time-step reconstructor in Chapter 4, again.

2.1.6 Iterative Computation for ELT-scale Tomography

In the case of WFAO systems on the current large telescopes, since we can compute the reconstructor matrix directly with inversing matrices of Eq. (2.11), the DM commands are estimated by multiply the measured slope by the reconstructor. However, on future ELT-scale WFAO system, computing Eq. (2.11) directly is hard because the matrices are too large. Therefore, iterative method is used to compute the tomographic reconstruction. In this thesis, we use the conjugate gradient method (CGM) for the tomographic reconstruction on the ELT-scale WFAO system.

The CGM solves an equation of $\boldsymbol{Ax} = \boldsymbol{b}$ for $\boldsymbol{x}$ iteratively, where $\boldsymbol{x}$ is a column vector of unknown estimate, $\boldsymbol{A}$ is a coefficient matrix, and $\boldsymbol{b}$ is a known measurements. The coefficient matrix $\boldsymbol{A}$ should be a positive definite symmetric matrix. In the case of the tomographic wave-front reconstruction, we need the CGM for both of the estimation step and the fitting step. In the estimation step, an equation to be solved by the CGM is given as

$$(\boldsymbol{P}_{\boldsymbol{\alpha}}^T \boldsymbol{\Gamma}_{\boldsymbol{\alpha}}^T \boldsymbol{C}_{\boldsymbol{\eta\eta}}^{-1} \boldsymbol{\Gamma}_{\boldsymbol{\alpha}} \boldsymbol{P}_{\boldsymbol{\alpha}} + \boldsymbol{L}^T \boldsymbol{L}) \hat{\boldsymbol{\phi}}(t) = \boldsymbol{P}_{\boldsymbol{\alpha}}^T \boldsymbol{\Gamma}_{\boldsymbol{\alpha}}^T \boldsymbol{C}_{\boldsymbol{\eta\eta}}^{-1} \boldsymbol{s}_{\boldsymbol{\alpha}}(t) \tag{2.22}$$

where $\hat{\boldsymbol{\phi}}(t)$ is a column vector of the phase distortion of the atmospheric turbulent

layers and this is a $\boldsymbol{x}$ in this case. We use the sparse approximation for the phase covariance matrix. Then, in the fitting step, we solve the following equation by the CGM for the DM commands $\hat{\boldsymbol{u}}_{\boldsymbol{\beta_k}}$.

$$(\boldsymbol{N}_{\boldsymbol{\beta_k}}^T \boldsymbol{N}_{\boldsymbol{\beta_k}})\hat{\boldsymbol{u}}_{\boldsymbol{\beta_k}}(t) = \boldsymbol{N}_{\boldsymbol{\beta_k}}^T \boldsymbol{P}_{\boldsymbol{\beta_k}} \hat{\boldsymbol{\phi}}(t) \tag{2.23}$$

The convergence of the CGM is decided by the relative error $||\boldsymbol{b} - \boldsymbol{A}\boldsymbol{x_k}||/||\boldsymbol{b}||$, where $\boldsymbol{x_k}$ is the estimates at k-th iteration.

Each iteration of the CGM consists of matrix-vector multiplications. Thanks to the sparse approximation for the phase covariance matrix, all matrices in the tomographic reconstruction are sparse. Therefore, we use sparse matrix computation for all matrix-vector multiplications in the CGM to reduce the computation time of each iteration.

The other thing to consider for reducing computation time is reducing the number of iteration of the CGM. The number of the iteration of the CGM depends on the condition number of a coefficient matrix $\boldsymbol{A}$. The condition number, $\kappa(\boldsymbol{A})$, is used to measure how sensitive a equation is to error of measurements, $\boldsymbol{b}$, and is defined as $\kappa(\boldsymbol{A}) = \sigma_{\max}(\boldsymbol{A})/\sigma_{\min}(\boldsymbol{A})$, where $\sigma_{\max}(\boldsymbol{A})$ and $\sigma_{\min}(\boldsymbol{A})$ are a maximum and a minimum singular value of a matrix $\boldsymbol{A}$, respectively. If condition number is large, the estimate is affected strongly by the measurement error and the number of the iteration required for the convergence increases. In general, before computing the CGM, we multiply the equation by a matrix $\boldsymbol{M}$, which reduces the condition number of the matrix, so-called *pre-condition matrix*, as $\boldsymbol{MAx} = \boldsymbol{Mb}$ or $\boldsymbol{MAM}^T(\boldsymbol{M}^T)^{-1}\boldsymbol{x} = \boldsymbol{Mb}$ in order to reduce the number of iteration. It is noted that $\boldsymbol{MA}$ or $\boldsymbol{MAM}^T$ should be a symmetric matrix to use the CGM. Several pre-conditioners are proposed for the CGM of the tomographic reconstruction. In this thesis, we use a diagonal-scaling matrix as the pre-conditioner matrix, which transforms the diagonal elements of a matrix to 1. This is known as the simplest pre-condition matrix.

Since the atmospheric turbulence may change smoothly with time, the estimate at the one time-step before is a good initial condition for the CGM at current time-step. This technique is called *warm start*, and can reduce the number of iteration largely. We also use this technique out computation for future ELT-scale tomographic reconstruction.

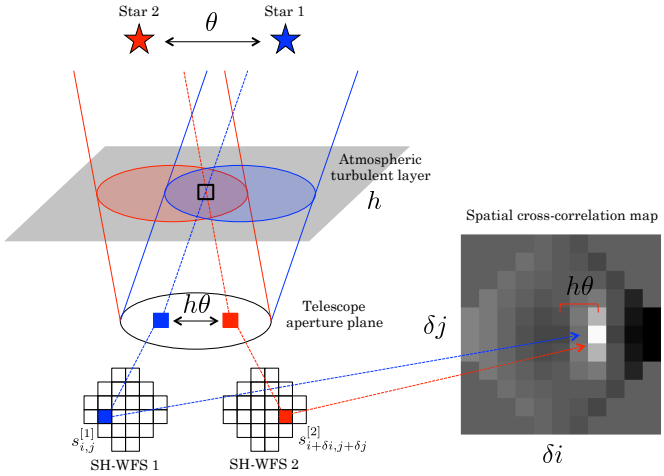

Figure. 2.3: Principle of SLODAR. The lights from two star with an angular separation θ cross at altitude h with a spatial displacement of $h\theta$ and propagate into $[i, j]$ subaperture of WFS1 and $[i + \delta i, æ; \delta j]$ subaperture of WFS2, respectively. The cross-correlation between these subapertures have a correlation power proportional to the turbulence power at altitude h.

2.2 Pre-Estimation Method for Required Parameters

For implement the tomographic reconstruction, we need knowledge of the measurement noise, turbulence height and strength, this is, C_N^2 profile. In addition, wind speed and direction at each altitude are also required to perform the multi time-step reconstruction. Since these quantities vary with time, we should estimated these parameters and update the reconstructor based on the new estimates in each minute. In this section, we describe the method to estimate the required parameter from the measurement of multiple SH-WFSs.

2.2.1 SLODAR for Estimating the C_N^2 Profiles

Slope detection and ranging (SLODAR) is a well-studied method to estimates the $C_N^2(h)$ profile with the measurement from two SH-WFSs. The SLODAR was proposed originally by [50], and is updated by some studies [8, 12]. The basic idea of SLODAR is shown in Fig. 2.3. Consider that there are two stars with an angular separation of θ and there is a turbulent layer at an altitude h. The lights from the two stars cross at altitude h, and reach a telescope aperture with a spatial displacement of $h\theta$. Therefore, if we observe these stars with different SH-WFSs and computes a spatial cross-correlation of the measurements from two SH-WFSs, there is a peak in the spatial cross-correlation map, corresponding to

the spatial offset of $h\theta$. The intensity of the peak is proportional to the strength of the turbulent layers, that is, C_N^2 value. In the case of multiple turbulent layers, there are several peaks corresponding to each turbulent layers and measuring the location and intensity of each peak provides us the vertical profile of $C_N^2(h)$. In this study, we use a method proposed by [8]. They determined the $C_N^2(h)$ by fitting the theoretical spatial cross-correlation maps to the observed cross-correlation map.

We denote a measured slope in x direction of a subaperture indexed $[i, j]$ at time t for the first star as $s_{i,j}^{x[1]}(t)$ and the x slope for the second star as $s_{i+\delta i,j+\delta j}^{x[2]}(t)$, where δi and δj are an offset of subapertures. In general, the C_N^2 estimation by SLODAR is computed with using 1–3 minutes time series of the slope. We subtract tip-tilt modes over the aperture from the measured slope to avoid the influence from the vibration or tracking error. In the slope space, this is equal to subtract the spatial average over subapertures from the measurement.

$$s'^{x[1]_{i,j}}(t) = s_{i,j}^{x[1]}(t) - \frac{1}{n_{\text{valid}}} \sum_{\text{valid } i,j} s_{i,j}^{x[1]}(t) \tag{2.24}$$

where s' is the tilt subtracted slope and n_{valid} is a number of the illuminated subaperture. We also subtract a temporal average in the slope measurement from the measured slope before computing the spatial cross-correlation. The average subtracted slope are computed as

$$s''^{x[1]_{i,j}}(t) = s_{i,j}'^{x[1]}(t) - \left\langle s_{i,j}'^{x[1]}(t) \right\rangle \tag{2.25}$$

where s'' is a slope after the tilt and average pattern subtraction and $\langle\rangle$ is a temporal average over 1–3 time series.

The spatial cross-correlation with subaperture offset of $[\delta i, \delta j]$ is defined as

$$C_{xx}^{\text{obs}}(\delta i, \delta j) = \frac{\left\langle \sum_{\text{valid } i,j} s_{i,j}''^{x[1]}(t) s_{i+\delta i,j+\delta j}''^{x[2]}(t) \right\rangle}{N(\delta i, \delta j)}, \tag{2.26}$$

where $\langle\rangle$ indicates averaging over time and $N(\delta i, \delta j)$ is the number of the pair with the separation $[\delta i,\delta j]$. The cross-correlation of y–y, x–y, and y–x can be defined by C_{yy}^{obs}, C_{xy}^{obs}, and C_{yx}^{obs} similar to Eq. (2.26). However, since the cross-correlations between x and y slopes, C_{xy}^{obs} and C_{yx}^{obs}, have a very week correlation, we use only C_{xx}^{obs} and C_{yy}^{obs} for the SLODAR. The cross-correlation map, $\boldsymbol{C}_{\boldsymbol{xx}}^{\textbf{obs}}$ and $\boldsymbol{C}_{\boldsymbol{yy}}^{\textbf{obs}}$, can be obtained to compute C_{xx}^{obs} and C_{yy}^{obs} for all possible subaperture offset $(\delta i, \delta j)$.

The theoretical cross-correlation maps are computed for each altitude bin based

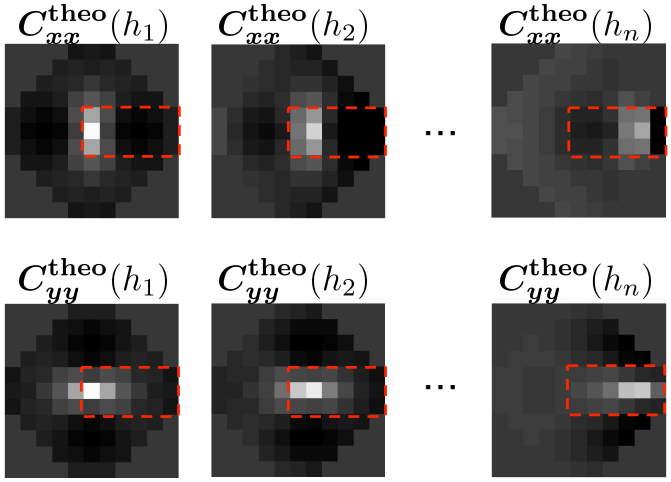

Figure. 2.4: Examples of theoretical slope cross-correlation. The outer scale is 30 m. The only areas surrounding by the red lines are used for the fitting.

on the turbulence model, as shown in Fig. 2.4. The optimal altitude resolution dh is given as $dh = d_{\mathrm{sa}}/\theta$, namely the spatial offset is an integral proporional to the subaperture size d_{sa}. In the case of WFAO with multiple GSs, we can compute the SLODAR for all GS pairs. Since each GS pair has a different angular separation θ, the optimal resolution in the height direction is also different. To avoid averaging profiles with different resolution, we set to a same altitude resolution for all GS pairs. The maximum altitude measured by SLODAR also depends on the angular separation of two stars, which is given by $h_{\mathrm{max}} = (n_{\mathrm{sa}} - 1)d_{\mathrm{sa}}/\theta$, where n_{sa} is a number of subaperture across a telescope pupil. Thus, smaller angular separation gives us the information at higher altitudes with lower altitude resolution. It is noted that the estimates of the C_N^2 value at higher altitude becomes noisier. The high altitude turbulence makes the correlation peak at large spatial offset $[\delta i, \delta j]$. The number of subaperture pair with the large offset is limited compared with the number of the subaperture pair with small offset. In addition, if we have GSs more than two, the high altitude is covered by GS pairs with large angular separation. Therefore, the estimated C_N^2 value becomes statistically noisy. In the later discussion, we remove the correlation between largest spatial offset from the fitting to avoid the influence from the noisy estimates.

Here, we consider the case of n_{pair} pair of GSs. The theoretical spatial cross-correlation maps of altitude h_i for kth GS pair are denoted as $\boldsymbol{C}_{\boldsymbol{xx}}^{\mathbf{theo}[\boldsymbol{k}]}$ and $\boldsymbol{C}_{\boldsymbol{yy}}^{\mathbf{theo}[\boldsymbol{k}]}$, where the theoretical correlation maps are normalized so that $C_N^2(h_i) = 1$. The observed spatial cross-correlation maps for kth pair are represented as $\boldsymbol{C}_{\boldsymbol{xx}}^{\mathbf{obs}[\boldsymbol{k}]}$ and $\boldsymbol{C}_{\boldsymbol{yy}}^{\mathbf{obs}[\boldsymbol{k}]}$. If the turbulence at multiple altitudes are independent from each other, the observed cross-correlation maps can be represented by a linear combination

of the theoretical spatial correlation maps for different altitudes as $\boldsymbol{C}_{\boldsymbol{xx}}^{\mathbf{theo}[\boldsymbol{k}]} \approx \sum_i a_i \boldsymbol{C}_{\boldsymbol{xx}}^{\mathbf{obs}[\boldsymbol{k}]}$. The coefficient a_i for the normalized theoretical correlation map is equal to C_N^2 value at altitude h_i. Considering all GS pairs, we can estimate C_N^2 profile by minimizing the following equation.

$$\min_{a_i} \sum_{k}^{n_{\mathrm{pair}}} \boldsymbol{W}^{\boldsymbol{k}} \left(\begin{bmatrix} \boldsymbol{C}_{\boldsymbol{xx}}^{\mathbf{obs}[\boldsymbol{k}]} \\ \boldsymbol{C}_{\boldsymbol{yy}}^{\mathbf{obs}[\boldsymbol{k}]} \end{bmatrix} - \sum_{i}^{n} a_i \begin{bmatrix} \boldsymbol{C}_{\boldsymbol{xx}}^{\mathbf{theo}[\boldsymbol{k}]}(h_i) \\ \boldsymbol{C}_{\boldsymbol{yy}}^{\mathbf{theo}[\boldsymbol{k}]}(h_i) \end{bmatrix} \right) \tag{2.27}$$

where $\boldsymbol{W}^{\boldsymbol{k}}$ is a masking matrix for the spatial cross-correlation for kth GS pair to extracts the area along the direction of the GS baseline on the cross-correlation map, which is the red area in Fig. 2.4. Since the peaks due to the turbulence layers lie along the direction of the GS baseline, we use only the areas for the SLODAR. The minimization of Eq. (2.27) is done with using *non-negative least square method* [34] because C_N^2 value should be more than 0 at all altitudes. This method provides better solution than the normal least square method without any constraint.

2.2.2 Estimation of SH-WFS measurement noise

The measurement noise can be estimated by a method similar to SLODAR [12]. On , we use the auto-correlation of the slope measured by SH-WFSs, which is defined as

$$A_{xx}^{\mathrm{obs}}(\delta i, \delta j) = \frac{\left\langle \sum_{i,j} s''^{x[1]}_{i,j}(t) s''^{x[1]}_{i+\delta i, j+\delta j}(t) \right\rangle}{N(\delta i, \delta j)}. \tag{2.28}$$

The auto-correlation has a peak at the center, $[\delta i, \delta j] = [0, 0]$, as shown in the left panels of Fig. 2.4. The central peak is enhanced by the measurement noise since the noise has a correlation power with no spatial offset for the auto correlation. Therefore, fitting the theoretical auto-correlations, $\boldsymbol{A}_{\boldsymbol{xx}}^{\mathbf{theo}}$ and $\boldsymbol{A}_{\boldsymbol{yy}}^{\mathbf{theo}}$, to the observed auto-correlations, $\boldsymbol{A}_{\boldsymbol{xx}}^{\mathbf{obs}}$ and $\boldsymbol{A}_{\boldsymbol{yy}}^{\mathbf{obs}}$, with removing the central point, $[\delta i, \delta j] = [0, 0]$, from the fitting and measuring the difference at the center provide us an estimate of the noise averaged over all subapertures. This fitting also gives us estimate of total turbulence of C_N^2 value including high altitude turbulence which can not be measured by the SLODAR. Comparing the total C_N^2 value measured by the auto-correlation fitting with the value from the SLODAR provides the residual turbulence power at high altitude not covered by SLODAR.

We note that this noise measurement gives us the averaged noise and can not be applied for the LGS system since the noise of each subaperture is not same due to the spot elongation and the outer subaperture has systematically a larger noise.

In order to optimise the tomographic reconstruction for the WFAO system with multiple LGSs, the noise difference due to the spot elongation should be taken into account, especially for future ELTs, in which the spot elongation will be more severe.

2.2.3 Wind Speeds and Directions Estimation

In this section, we present the method to estimate wind speeds and directions at multiple altitudes by using the result of tomographic reconstruction. If there are N_l atmospheric layers, the tomographic reconstruction provides the phase distortion on N_l atmospheric turbulence layers, $\hat{\boldsymbol{\phi}}(t) = [\hat{\boldsymbol{\phi}}_{\mathbf{1}}^T(t) \cdots \hat{\boldsymbol{\phi}}_{\boldsymbol{N_l}}^T(t)]^T$. The reconstructed phase distortion pattern on the atmospheric layers at each altitude moves with time due to the wind. Tracking this movement allow us to estimate wind speeds and directions at multiple altitudes separately. In order to detect this movement due to wind, we use temporal correlation.

After reconstructing the phase distortion at each altitude by the tomographic reconstruction, we extract aperture-size wavefront at each altitude in the direction of the center of a GS asterism from the reconstructed phase distortion because the size of the turbulence layers are too large to compute temporal correlation. In addition, it is better to use only areas reconstructed accurately for estimating wind speeds and directions. Although the GS directions has smaller integrated WFE or better SR than other direction because the tomographic reconstruction is computed based on the measurements from the GS direction, it is possible that the most areas at high altitude in GS directions are covered by only own optical path, as shown in the left panel of Fig. 1.7, and affected by the degeneracy due to the *unoverlapped area*. This is because the reconstructed phase distortion at each altitude in the GS direction can be cancelled each other to reduce total WFE in this direction. Therefore, the reconstructed phase distortion in the GS directions may not reflect the real phase distortion pattern, and using GS direction for the wind estimation is not optimal. As shown in Fig. 1.7, the direction of the center of the GS asterism are covered by multiple GS footprints, and the reconstructed phase distortion at each altitude is more accurate compared to the other directions.

We define a matrix $\boldsymbol{P_c^i}$ as the cropping matrix, which extracts the wave-front in the direction of the center of the GS asterism from the estimated phase distortion $\hat{\boldsymbol{\phi}}_{\boldsymbol{i}}$ of the ith turbulent layer.

$$\hat{\boldsymbol{\phi}}_{\boldsymbol{c}}^{\boldsymbol{i}}(t) = \boldsymbol{P_c^i}\hat{\boldsymbol{\phi}}_{\boldsymbol{i}}(t). \tag{2.29}$$

where $\hat{\boldsymbol{\phi}}_{\boldsymbol{c}}^{\boldsymbol{i}}(t)$ is the wave-front at time t extracted from ith turbulence layer. Before computing the temporal correlation, the extracted wave-front is converted into the slope by a discrete phase-to-slope operator $\boldsymbol{\Gamma}_{\boldsymbol{c}}$.

$$\hat{\boldsymbol{s}}_{\boldsymbol{c}}^{\boldsymbol{i}}(t) = \boldsymbol{\Gamma}_{\boldsymbol{c}}\hat{\boldsymbol{\phi}}_{\boldsymbol{c}}^{\boldsymbol{i}}(t), \tag{2.30}$$

where $\hat{\boldsymbol{s}}_{\boldsymbol{c}}^{\boldsymbol{i}}(t)$ is a reconstructed slope vector corresponding to a phase distortion of i-th atmospheric turbulence layer in the direction of the center of the GS asterism at time t. A peak of a slope correlation is sharper than the peak of a wavefront correlation, and can be detected easier than the peak of the wavefront correlation. This is because the slope measured by SH-WFS corresponds to a differential of the phase distortion and the differential play a role of a high-pass filter. Therefore, the small-scale and weak phase distortion is more weighted than large-scale strong distortion by converting to slope, and the movement of the distortion pattern is made clearer on the temporal correlation.

Temporal correlation of the reconstructed slope at i-th turbulence layer can be computed by the same way as SLODAR.

$$T_{xx}^{\mathrm{obs}[i]}(\delta p, \delta q, \delta t) = \frac{\left\langle \sum_{p,q} \hat{s}''^{x,i}_{p,q}(t)\hat{s}''^{x,i}_{p+\delta p,q+\delta q}(t+\delta t) \right\rangle}{N(\delta p, \delta q)}. \tag{2.31}$$

where δt is the time delay for the temporal correlation. The temporal correlation map $\boldsymbol{T}_{\boldsymbol{xx}}^{\mathbf{obs}[\boldsymbol{i}]}$ can be obtained by computing Eq. (2.31)for all possible pairs of δp and δq. The correlation for y-direction slope is represented as similar to Eq. (2.31). In order to increase signal to noise, the correlations of x and y-direction slopes are averaged, $\boldsymbol{T}^{\mathbf{obs}[\boldsymbol{i}]} = (\boldsymbol{T}_{\boldsymbol{xx}}^{\mathbf{obs}[\boldsymbol{i}]} + \boldsymbol{T}_{\boldsymbol{yy}}^{\mathbf{obs}[\boldsymbol{i}]})$.

The movement of the correlation peak on the correlation map $\boldsymbol{T}^{\mathbf{obs}[\boldsymbol{i}]}$ with δt corresponds to the wind speed and direction of ith turbulence layers. We use the centroid algorithm to detect the peak. When a subaperture size of SH-WFS is d_{sa} and the peak position is $(\delta p, \delta q)$, the wind speed is computed by $v_x = d_{\mathrm{sa}}\delta u/\delta t$ and $v_y = d_{\mathrm{sa}}\delta v/\delta t$. By computing v_x and v_y and averaging it over different δt, the wind speed and direction at each altitude can be estimated.

Chapter 3

Analytical Evaluation

3.1 Analytical Tomographic Error

The tomographic error in direction $\boldsymbol{\beta_k}$ is defined as $\sigma_{\boldsymbol{\beta_k}} = (\epsilon_{\boldsymbol{\beta_k}\mathrm{tomo}}/n_p)^{1/2}$, where $\epsilon_{\boldsymbol{\beta_k}}$ is the residual phase variance at an aperture plane defined in Eq. (2.6) and n_p is the number of phase point at aperture plane. Here, we assume that the all subaperture has a same measurement noise variance σ_η^2. In this case, the covariance matrix of the measurement noise $\boldsymbol{\Sigma_{\eta\eta}}$ become $\sigma_\eta^2\boldsymbol{I}$, where $\boldsymbol{I}$ is an identity matrix. We also assume that the DM interaction matrix $\boldsymbol{N_{\beta_k}}$ for $\boldsymbol{\beta_k}$ direction is an identity matrix for simplicity, which means the DM command is equal to the phase caused by the DM. Using this assumption and Eq. (A.2), the tomographic error can be represented as

$$\begin{aligned}\sigma^2_{\boldsymbol{\beta_k},\mathrm{tomo}} =& \frac{\mathbf{Tr}\left[\boldsymbol{R}_{\mathrm{piston}}(\boldsymbol{P}_{\boldsymbol{\beta_k}} - \boldsymbol{E}_{\boldsymbol{\beta_k}}\boldsymbol{\Gamma}_{\boldsymbol{\alpha}}\boldsymbol{P}_{\boldsymbol{\alpha}})\boldsymbol{\Sigma}_{\boldsymbol{\phi\phi}}(\boldsymbol{P}_{\boldsymbol{\beta_k}} - \boldsymbol{E}_{\boldsymbol{\beta_k}}\boldsymbol{\Gamma}_{\boldsymbol{\alpha}}\boldsymbol{P}_{\boldsymbol{\alpha}})^T\boldsymbol{R}^T_{\mathrm{piston}}\right]}{n_p} \\ &+ \sigma^2_\eta\frac{\mathbf{Tr}\left[\boldsymbol{R}_{\mathrm{piston}}\boldsymbol{E}_{\boldsymbol{\beta_k}}\boldsymbol{E}^T_{\boldsymbol{\beta_k}}\boldsymbol{R}^T_{\mathrm{piston}}\right]}{n_p} \\ =& \sigma^2_{\boldsymbol{\beta_k},\mathrm{geo}} + \sigma^2_{\boldsymbol{\beta_k},\mathrm{noise}}. \end{aligned} \tag{3.1}$$

where $\boldsymbol{R}_{\mathrm{piston}}$ is a matrix removing a piston mode from the residual wave-front. If you would like to compute the tomographic error without piston and tilt modes, it is achieved by the replacing $\boldsymbol{R}_{\mathrm{piston}}$ to $\boldsymbol{R}_{\text{tip-tilt}}\boldsymbol{R}_{\mathrm{piston}}$, where $\boldsymbol{R}_{\text{tip-tilt}}$ is a matrix removing tip-tilt. This tomographic error can be computed by the matrix calculation, so-called *analytical tomographic error*. The first term $\sigma^2_{\boldsymbol{\beta_k},\mathrm{geo}}$ represents the tomographic error determined by the geometry such as GS configuration, turbulence structure, and reconstructor, and we refer to $\sigma^2_{\boldsymbol{\beta_k},\mathrm{geo}}$ as *geometric error*. The influence from the *uncovered* and the *unoverlapped areas* are included in the first term. The second term $\sigma^2_{\boldsymbol{\beta_k},\mathrm{noise}}$ is a noise propagation of the measurement noise σ_η. The purpose of the multi time-step reconstructor is to reduce the geometric

Parameters	Values
Diamter of an telescope aperture	30 m
Fried parameter r_0	0.156 m
outer scale L_0	30 m
Altitudes of the turbulence layers	0 km, 5 km, and 10 km
Fraction of C_N^2	50, 25, and 25 %
Wind speeds	5 $\mathrm{m\,s^{-1}}$, 10 $\mathrm{m\,s^{-1}}$, and 20 $\mathrm{m\,s^{-1}}$
Wind directions	90°, 0°, 0°
Number of NGSs	3
NGS asterism radius r_{ast}	20–200 arcseconds
WFS	Shack-Hartmann WFS with 30×30 subapertures
Diameter of subaperture	1 m
Measurement noise	0.01 arcsecond

Tab. 3.1: Parameters used for the analytical evaluation.

error.

3.2 Model

The model for the analytical evaluation is as follows. We consider a simple MOAO model on a 30 m circular aperture telescope with three NGSs. The NGSs are put on a ring of a radius r_{ast}, which is a range of 20–200 arcseconds, indicated as the red plots in Fig. 3.2. We evaluate the tomographic error in the direction of the center of FoR and in the outer directions, shown as the blue and green plots in Fig. 3.2. Fig. 3.1 shows a footprints of the NGS optical paths and the evaluated directions at 10 km as $r_{\mathrm{ast}} = 20$ arcseconds (the left panel) and $r_{\mathrm{ast}} = 200$ arcseconds (the right panel). Fried parameter r_0=0.156 m and the outer scale is 30 m, which are typical value at Maunakea. The atmospheric turbulence consists of three turbulence layers at 0 km, 5 km and 10 km. The C_N^2 fractions are [50 %, 25 %, 25 %], the wind speeds are [5 $\mathrm{m\,s^{-1}}$, 10 $\mathrm{m\,s^{-1}}$, 20 $\mathrm{m\,s^{-1}}$], and the wind directions are [90°, 0°, 0°] at 0, 5, and 10 km, respectively. The size of subaperture of SH-WFSs is 1 m on the aperture-plane and all subapertures have a same measurement noise with a variance of σ_η^2. The spatial sampling of discrete grids on the turbulence layers and the aperture-plane is 1 m. The parameters used for this analysis are summarized Table3.1. Over this chapter, the temporal lag error and the fitting error are not

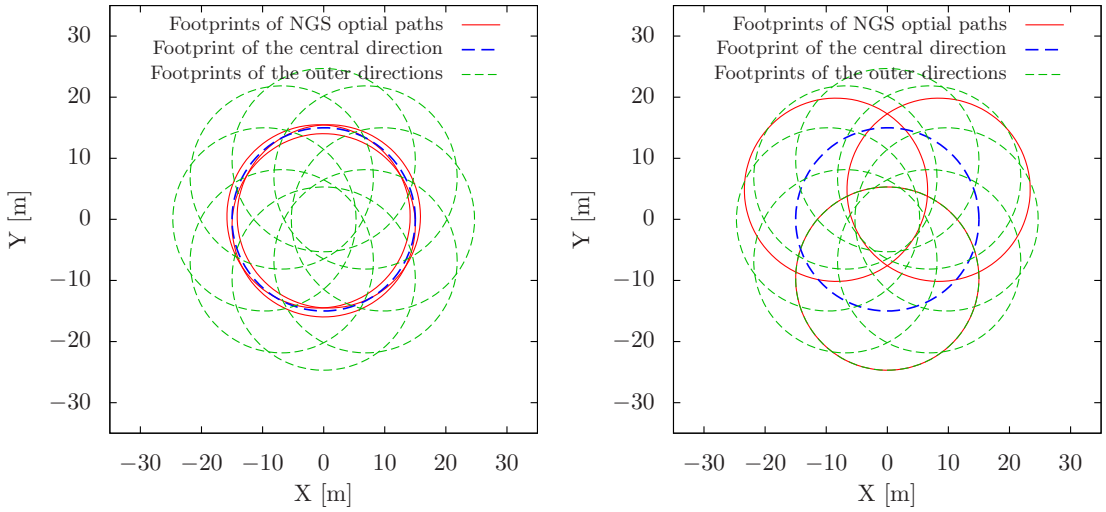

Figure. 3.1: Footprints of the NGS optical paths (red) and the evaluated central direction (blue) at altitude of 10 km for r_{ast}=20 arcseconds (left) and r_{ast}=200 arcseconds (right).

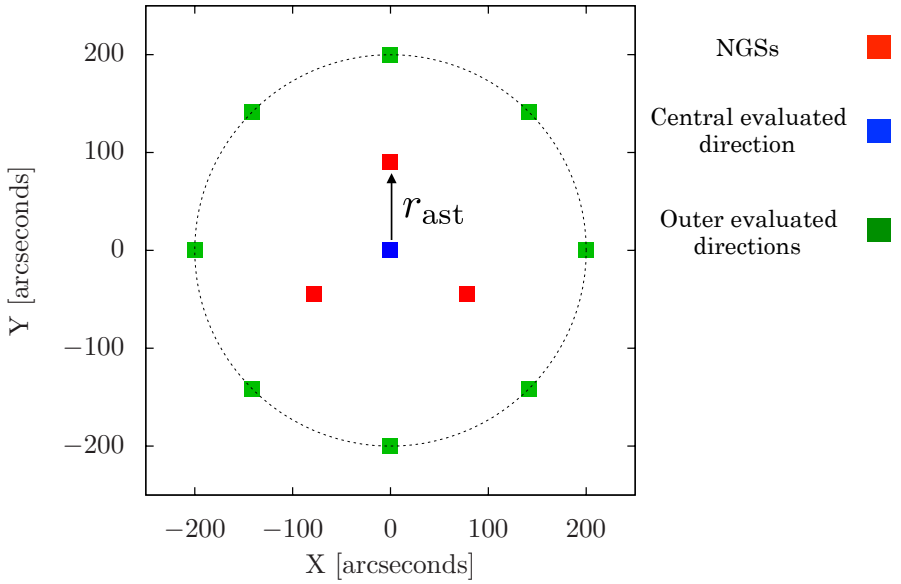

Figure. 3.2: The NGS asterism (red) and the evaluated directions. The blue plot is the central evaluated direction. The green plots are the outside evaluated directions.

included in this analysis and we assume that we have the perfect knowledge of the turbulence altitudes, powers, and wind speeds and directions.

3.3 Effect of Lack of Information

First we demonstrate the influence from *uncovered* and *unoverlapped area*. Fig. 3.3 show the geometric error σ_{geo}, the noise propagation σ_{noise}, and the total tomographic error σ_{tomo} as a function of the asterism radius r_{ast}. The red solid lines in Fig. 3.3 indicate the result with the errors of the single time-step reconstructor evaluated in the central direction and the red dotted lines are the errors of the single time-step reconstructor averaged the values evaluated in the outer directions. Those errors are computed with removing tip-tilt errors.

When r_{ast} is small, the geometrical error of the central direction (solid red line) is small because the central direction is covered densely by the multiple footprints of the NGS optical path in the atmosphere as the left panel of Fig. 3.1. In the outer directions, the geometric error (dashed red line) is large due to the *uncovered area* at small r_{ast}. Then, as the asterism radius increases, the geometric error in the central direction also increases rapidly. At $r_{\text{ast}} = 200$ arcseconds, the geometric error in the central direction is 538 nm, which is ten times larger than the value at $r_{\text{ast}} = 20$ arcseconds. This is due to the *unoverlapped area*. At $r_{\text{ast}} = 200$ arcseconds, all area of the footprint in the central direction is covered by the NGS optical paths, as shown in the right panel of Fig. 3.1. However, some parts of footprints in the central direction are covered by only one footprint of the NGS. The *unoverlapped area* increases with the asterism radius and results in the large geometric error. Although the geometric error in the outer directions decreases because of decreasing the *uncovered area*, the geometric error is still large, which is 408 nm, since most of the footprints in the outer directions is *unoverlapped area*. The noise propagation, which are indicated by the red lines in Fig. 3.3(b), is much smaller than the geometric error for both directions. Therefore, the total tomographic error of the single time-step reconstructor in Fig. 3.3(c) is dominated by the geometric error.

This result suggests the difficulty of expanding the FoR size of the tomographic WFAO systems. In order to expand the FoR size, we have to measure and reconstruct a large volume of the atmospheric turbulence corresponding to the large FoR by expanding the NGS asterism. However, it involves the large tomographic error as we show. This effect become more severe with using LGSs because of

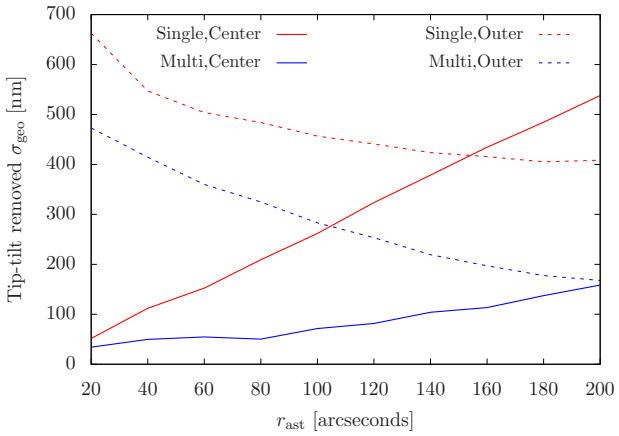

(a) Tip-tilt removed geometric error σ_{geo}

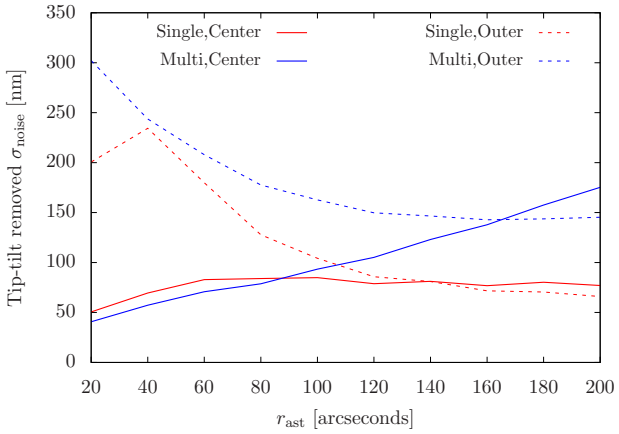

(b) Tip-tilt removed noise propagation σ_{noise}

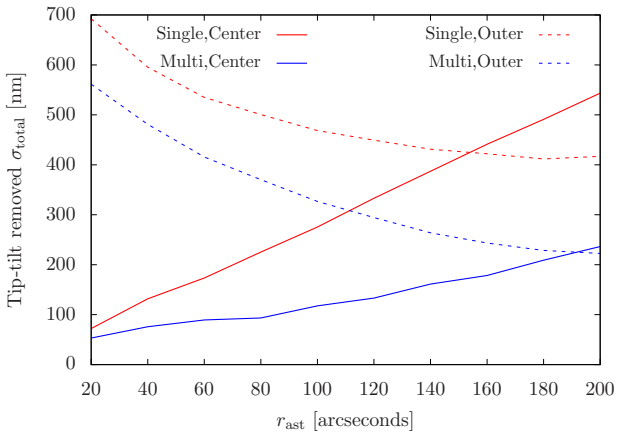

(c) Tip-tilt removed tomographic error σ_{tomo}

Figure. 3.3: The analytical geomatric error σ_{geo} (top), the noise propagation σ_{noise} (middle), and the total tomgoraphic error σ_{tomo} (bottom) as a function of the asterism radius r_{ast}. The all values are computed with removing tip-tilt modes from the residual wave-fronts. The red lines show the result with the single time-step tomographic reconstruction and the blue lines are the results of the multi time-step reconstruction. The solid lines indicate the value evaluated in the direction of the center of the FoR. The dashed lines are the results averaged over outer directions.

its smaller footprints at high altitudes due to the cone effect. This is a critical problem at future ELT-scale WFAO system.

3.4 Analytical Performance of Multi Time-Step Reconstruction

The blue lines in Fig. 3.3 show the results of the multi time-step reconstructor with using the measurement from two time-steps. We set the time difference Δt for the previous time-step to 50 ms. This value is determined by considering temporal de-correlation of the atmospheric turbulence. In [46], they investigated the temporal decay of the auto-correlation intensity of the slope measured by a SH-WFS and defined the time t_{50}, which is the times for which the intensity of the auto-correlation decreases to 50 % of its initial value. In Fig. 3.3(a), the difference of the geometric error in the central direction between the single and the multi time-step reconstruction is small as the asterism radius is small. This means that the single time-step reconstructor is not affected by the *unoverlapped area* in the central direction with the small asterism radius. In the outer directions, the geometric error of the multi time-step is smaller than the error of the single time-step reconstruction for the outer directions, but is much larger than the geometric error of the multi time-step reconstruction for the central direction. Here, we use the measurement at 50 ms previous time-step. The spatial displacement due to the wind between the current and the previous time-steps is 0.25 m, 0.5 m, and 1.0 m at 0 km, 5 km, and 10 km, respectively. Since these offset is not enough to fill the *uncovered area* in the outer directions, the geometric error in the outer directions are not improved so much by the multi time-step reconstruction.

As the asterism radius large, the difference of σ_{geo} can be seen clearly. The multi time-step reconstructor can reduce dramatically the geometric error in both the central and outer directions. The geometric error in the outer directions are comparable to the value in the central direction. This result demonstrates that using the measurements from multi time-steps is effective to solve the degeneracy due to the *unoverlapped area*. The σ_{geo} of the multi time-step reconstructor is 158 nm at r_{ast}=200 arcseconds and is much smaller than the value of the single reconstructor.

The noise propagations of the multi time-step reconstruction is a bit larger than the noise propagation of the single time-step reconstructor in both the central and outer directions. At large asterism radius, the error due to the noise propagation

is roughly comparable to or larger than the geometric error. As result, the total tomographic error is affected by the both effects, as shown in Fig. 3.3(c). However, the tomographic error is much smaller than the value of the single time-step reconstructor. As the asterism radius is 200 arcseconds, the multi time-step reconstructor achieves the tomographic error σ_{geo} ∼220 nm. This is corresponding to the tomographic error in the central direction of the single time-step reconstructor at the asterism radius of r_{ast}=80 arcseconds. Although this result is based on the optimal condition, where the turbulence altitudes, powers, and wind speeds and directions are given, the multi time-step reconstructor has a possibility to reduce the geometric error and expand the FoR size dramatically.

3.5 Dependency on Time Difference Δt

Fig. 3.4 shows the geometric error σ_{geo}, the noise σ_{noise}, and the total tomographic error σ_{tomo} as a function of the time difference Δt for the multi time-step reconstructor. Those errors are also computed with removing tip-tilt errors and we use two time-step measurements for the multi time-step reconstruction. The asterism radius is assumed 200 arcseconds and therefore the main problem is the degeneracy due to the *unpverlapped area*. The used colors are same as Fig. 3.3. The horizontal red lines in Fig. 3.4 are results from the single time-step reconstructor, which doesn't depend on the time difference Δt.

In Fig. 3.4(a), an interesting point is that the multi time-step reconstructor can reduce the geometric error compared to the single time-step reconstructor even with very small Δt such as 10 ms. The spatial displacement due to the wind during 10 ms are 0.05 m, 0.1 m, and 0.2 m at 0 km, 5 km, and 10 km, respectively. These displacement is much smaller than the size of subaperture of 1 m. While the geometric error of the multi time-step error decreasing with Δt, it looks saturated as Δt =60–80 ms, where the spatial displacements are 0.4 m, 0.8 m, 1.6 m at each altitude, respectively. This results suggests that the spatial displacement equal to the subaperture size may be enough to solve the degeneracy due to the *unoverlapped area*.

With respect to the noise propagation, the multi time-step reconstructor is affected more by the measurement noise compared with the single reconstructor as shown in Fig. 3.4(b). The WFE due to the noise propagation has a similar trend to the Fig. 3.4(a) and is comparable to the WFE due to the geometric error.

As a result, the total tomographic error of the multi time-step reconstruction is

affected by both σ_{geo} and σ_{noise}. However, it is much smaller than the tomographic error of the single time-step reconstructor. This difference of σ_{tomo} becomes larger with Δt.

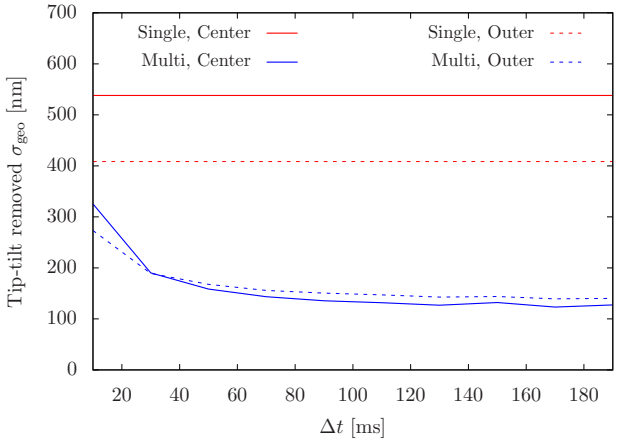

(a) Tip-tilt removed geometric error σ_{geo}

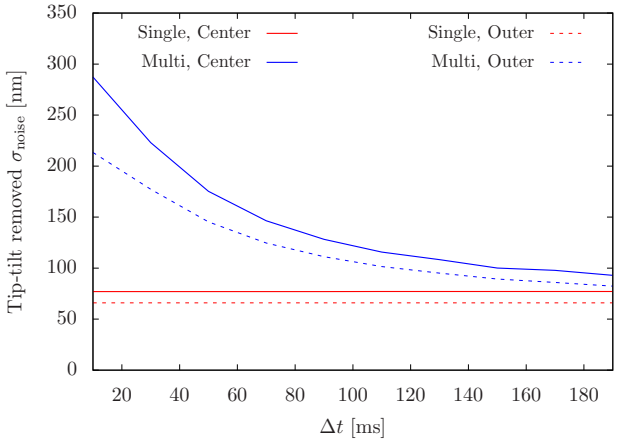

(b) Tip-tilt removed noise propagation σ_{noise}

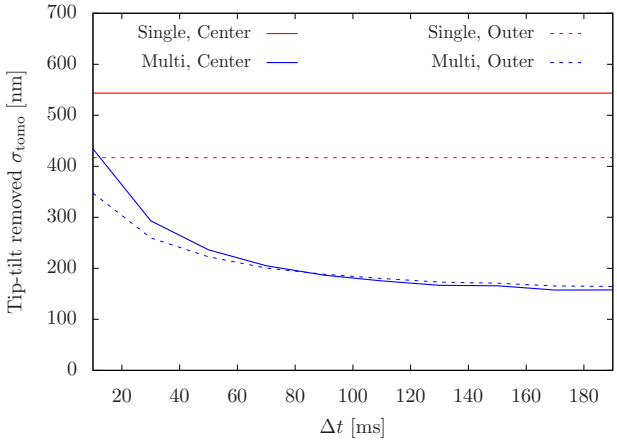

(c) Tip-tilt removed tomographic error σ_{tomo}

Figure. 3.4: The analytical geomatric error σ_{geo} (top), the noise propagation σ_{noise} (middle), and the total tomgoraphic error σ_{tomo} (bottom) as a function of the asterism radius r_{ast}. The all values are computed with removing tip-tilt modes from the residual wave-fronts. The color and line type are same as Eq. (3.3)

Chapter 4

Numerical Simulation

4.1 Simulation Setting

In this chapter, we show the results based on the numerical simulation with assuming ELT-scale MOAO system and investigate the expected performance of the multi time-step reconstruction on these future ELT. We assume a circular aperture with 30 m diameter. The MOAO system has a FoR of 10 arcminutes diameter and does the tomographic reconstruction with eight sodium LGSs at altitude of 88 km. Two LGS asterisms are used in this simulation, which are shown in Fig. 4.1. One is a narrow asterism indicated as open squares in Fig. 4.1, and the other is a wide asterism indicated as filled squares. As mentioned in Chapter 1, tip-tilt modes in wave-front can not be sensed by the LGS and therefore, TT-NGSs are required in a FoR to measure the tip-tilt modes. In this simulation, however, we assume that we can measure the low-order modes of the phase distortion from the LGSs for simplicity. The cone effect and the spot elongation on SH-WFS are considered in the simulation. The vertical sodium-layer profile is approximated to reproduce the lidar measurements [19] as

$$\mathrm{Na}(h) = \begin{cases} \exp\left(-\frac{(h-h_{\mathrm{NA}})^2}{2\sigma_{\mathrm{Na}}^2}\right) & (\text{for } |h - h_{\mathrm{LGS}}| < \sigma_{\mathrm{Na}} \\ 0 & (\text{for } |h - h_{\mathrm{LGS}}| > \sigma_{\mathrm{Na}} \end{cases} \tag{4.1}$$

where $h_{\mathrm{NA}} = 88$ km is an altitude of a sodium layer from the telescope, and σ_{Na}=5 km is a half width of the sodium-layer. The vertical profile of the sodium layer is presented in Fig. 4.2. We use SH-WFSs with 60×60 subapertures and DMs for science targets with 60×60 elements. The spatial sampling of atmospheric turbulence is 0.05 m. The WFE is also evaluated with this spatial sampling to simulate the fitting error. We assume that the MOAO system is controlled with 800 Hz and there is two frames delay between the measurement by WFSs and correction by DMs, that is, 2.5 ms delay on a frame rate of 800 Hz.

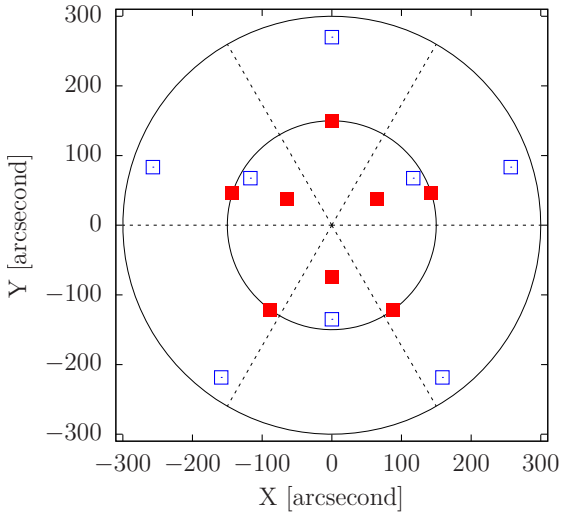

Figure. 4.1: LGS asterisms used in the numerical simulation. A narrow asterism is indicated with the red filled squares. The blue open squares show a wide asterism. The black solid lines show the 2.5 arcminutes and 5 arcminutes radius from the center of a FoR. The dashed lines are directions where the performance is evaluated.

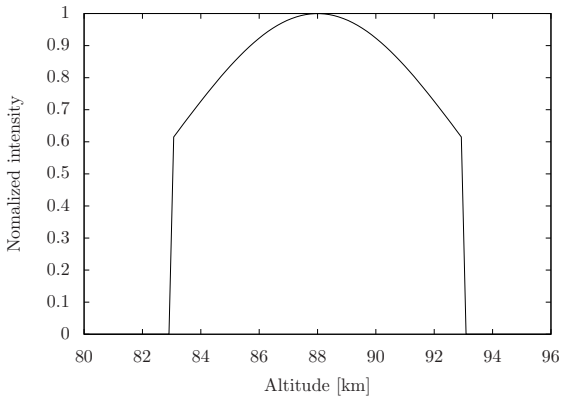

Figure. 4.2: Vertical profile of normalized intensity of Sodium layer used in the simulation. This is approximated based on the lidar on-sky measurements [19]. The altitude and of sodium layer are 88 km and 10 km.

We assume the top of Maunakea as the observation site in the simulation and use a seven-layer model used in [4] for the C_N^2 profile. This model is created based on image-quality measurements from the Subaru Observatory [39] and differential image motion monitor (DIMM) and multiple aperture scintillation sensor (MASS) measurements by Thirty Meter Telescope Project at Maunakea [16]. The model takes into account for additional dome seeing in the Subaru telescope, thus the ground layer has a strong turbulence power, which is 60 % of the total turbulence power. Fried parameter r_0 is 50 %ile value of the seeing measurements, $r_0 = 0.156$

m, and an outer scale is assumed to be 30 m. The C_N^2 values at each altitude are summarized in Table 4.2. We assume a gaussian model for the wind speeds on each layer based on [24]. The assumed wind speeds and directions are also listed in Table 4.2. The performance is evaluated at wavelength of 1650 nm (H-band).

For the computation of the tomographic reconstruction, we use the iterative CGM with the simple diagonal scaling preconditioner. Also, we use Tesla K40 GPU for the parallel computation of the tomographic reconstruction. The codes for GPGPU are made with CUDA 6.0, which is C++ like language for GPGPU. However, all results shown in this chapter are computed with assuming that the computation time is negligible. With respect to the computational efficiency with GPGPU, we will discuss it at end of this chapter.

4.2 Simulation Results

4.2.1 Performance of Multi Time-step Wave-Front Reconstruction

First, we simulated an optimal performance of the single and the multi time-step reconstructors for both of the narrow and the wide LGS asterisms with an assumption that the turbulence profile, wind speeds and directions are known *a priori*. The results are illustrated in Fig. 4.3. SR values are measured from simulated point spread function (PSF) images by comparing the peak intensities of the PSF images to the peak intensity of a diffraction-limited PSF image created by the simulation. All PSF images from the simulation are normalized by the total intensity with in a 1 arcsecond box. The top and the bottom panels in Fig. 4.3 show the simulated maps of the Strehl ratio (SR) across the FoR of 10 arcminutes diameter with the single (top) and the multi time-step (bottom) reconstructors. We use Δt of 50 ms for the multi time-step reconstructor as well as Chapter 3. The bottom panels in Fig. 4.3 show SR profiles as a function of an angular distance from the center of the FoR. The profiles are computed by averaging over six directions shown as dashed lines in Fig. 4.1.

With the narrow asterism, the single time-step reconstructor, which is indicated as red filled squares in the left panels of Fig. 4.3, achieves the averaged SR values of $\sim$0.5 within the inner LGS radius at 75 arcseconds from the center. The averaged SR value decreases slowly with an angular separation from 75 arcseconds to 150 arcseconds because of increasing the *unoverlapped area* as shown in the left

Parameters	Values
Diameter of aperture	30 m
FoR	10 arcminutes
Zenith angle	0°
Number of LGSs	8
Height of LGSs	90 km
Number of turbulence layers	7
r_0 at 500 nm	0.156 m
L_0	30 m
WFS	SH-WFS
Number of WFS subapertures	60×60
Number of DM elements	60×60
Frame rate	800 Hz
Time lag	2 frames
count per a subaperture	700 electrons
readout noise	3 electrons
evaluate wavelength	1650 nm (H-band)

Tab. 4.1: Parameters used in the numerical simulation.

Altitude [km]	$\int C_N^2 dh$ [10^{-14} $m^{1/3}$]	Fraction of C_N^2	wind speed [ms^{-1}]	wind direction [degree]
16	2.734	0.0826	7.0	0
8	2.264	0.0684	33.0	45
4	2.879	0.0869	19.7	90
2	1.233	0.0372	11.6	135
1	1.074	0.0325	9.0	180
0.5	3.190	0.0963	8.0	225
0	19.737	0.5960	7.0	270
Total r_0 [m]	0.156			

Tab. 4.2: Atmospheric turbulence profile used in the numerical simulation.

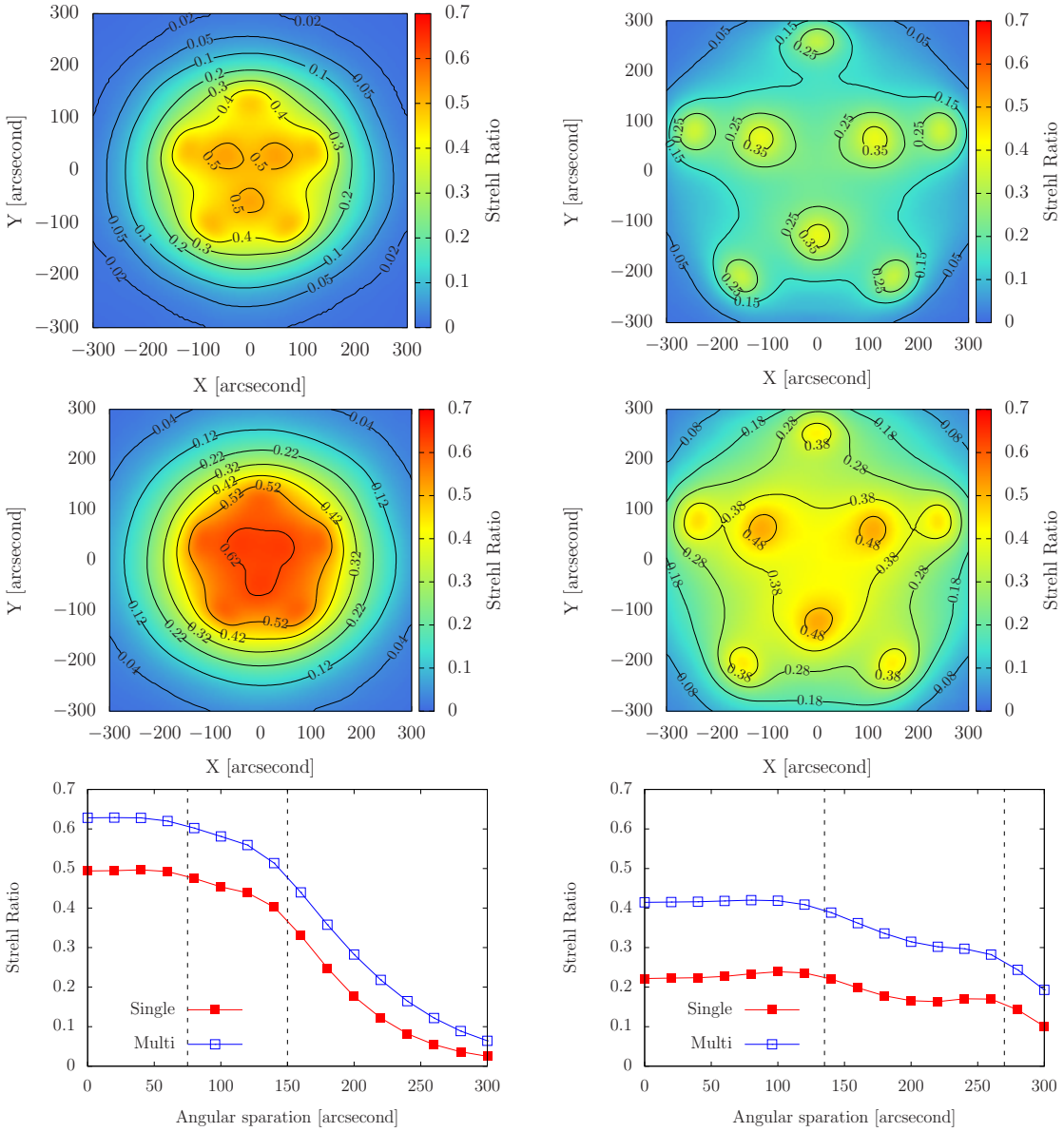

Figure. 4.3: Top and middle : Simulated SR maps within the 10 arcminutes FoR computed by using the single time-step reconstructor (top) or the multi time-step reconstructor with Δt=50 ms (middle). The right panels are the results with the narrow LGS asterism, and the left panels are computed with the wide LGS asterism. The multi time-step reconstructor improves SR values over the FoR for both of the asterisms. Bottom : SR profiles as a function of an angular separation from the center direction of the FoR. The profiles are averaged over directions shown as the dashed lines in Fig. 4.1. The red filled squares show the averaged SR profile with the single time-step reconstructor, and the blue open squares is the result by the multi time-step reconstructor with Δt=50 ms. The dashed black lines show the radii of LGS positions.

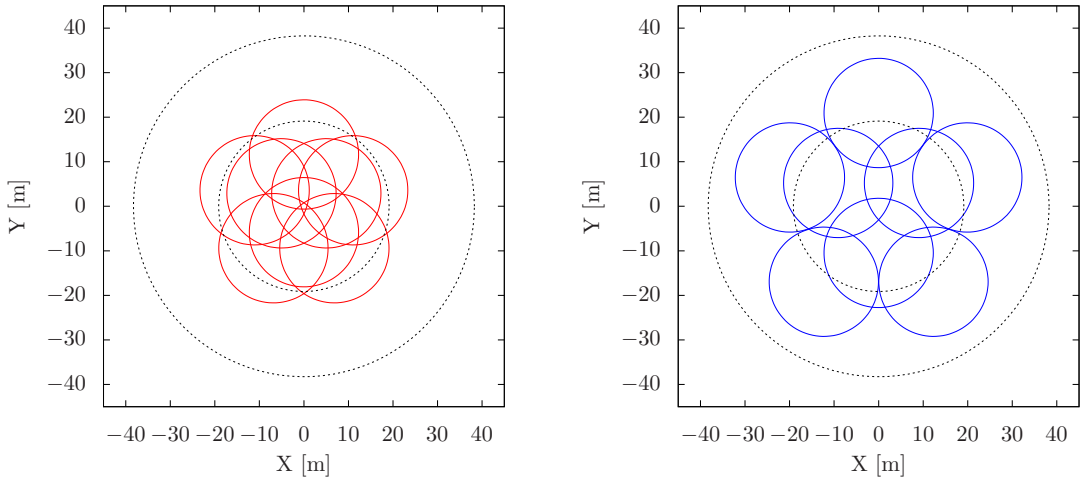

Figure. 4.4: The footprints of the LGS optial paths on the highest turbulence screen at altitude of 16 km The left panal shows the footprints with the narrow asterism and the right is for the wide asterism. The dashed black circle indicates the radius of 150 arcseconds and 300 arcseconds from the center of the FoR.

panel of Eq. (4.4). In the outer region than 150 arcseconds radius, the averaged SR values decrease steeply because there is no LGS and these areas are affected by *uncovered area*. The multi time-step reconstructor with Δt =50 ms, represented as the blue open squares, can increase the SR value over the FoR. The improvement of the averaged SR value is approximately 0.1 at 150 arcseconds, even though there is no *uncovered area* at $r \leq 150$ arcseconds. This suggests that the single time-step reconstructor is affected by the degeneracy due to the *unoverlapped area* even with the narrow asterism.

In the case of the wide asterism, illustrated in the right panels of Fig. 4.3, the SR value at the outer region than 200 arcseconds radius is better than the value of the narrow asterism because the wider area is covered by the LGSs as shown in the right panel of Eq. (4.4). In the contrast, the larger separation between LGSs causes a larger *unoverlapped area* at high altitudes. Hence, the SR value at inside area becomes smaller than the narrow asterism, and there are valley areas between LGSs on the SR map (the left top panel of Fig. 4.3). From the bottom right panel of Fig. 4.3, the averaged SR value is 0.24 with the single time-step reconstructor at maximum. This is affected strongly by *unoverlapped area*. Using the multi time-step reconstructor with Δt = 50 ms can double the averaged SR over the FoR for the wide asterism. At 300 arcseconds from the center, the SR value from the multi time-step reconstructor with the wide asterism is 3 times larger than the result of the narrow asterism.

4.2.2 Dependency on Time Difference Δt and Frozen Flow Assumption

The performance of the multi time-step reconstructor depends on the spatial displacement between the areas measured by the current and the previous time-steps at each altitude, which we refer as $d(h)$ in the paper. This displacement $d(h)$ corresponds to the movement of the atmospheric turbulence layer at an altitude h during Δt, $d(h) = v(h)\Delta t$, if the wind speed is $v(h)$ at an altitude h. The dependence of the multi time-step reconstructor on the Δt is presented in Fig. 4.5. The vertical axis in Fig. 4.5 is the SR improvement ratio, k_{SR}, which represents the ratio of the SR value achieved by the multi time-step reconstructor to the SR value from the single time-step reconstructor and is averaged over the angular separation from the center of the FoV. The multi time-step reconstructor achieves larger k_{SR} for the wide asterism than the narrow one. This suggests the wide asterism is affected more by the *unoverlapped area* than the narrow asterism. However, the trend of the dependence of the k_{SR} on Δt looks similar for the both asterisms. This suggests that the dependence on Δt doesn't depend the asterism of GSs. The multi time-step reconstructor improves the SR even with small Δt. There is 23 % increase in the SR value as Δt=20 ms for the narrow asterism. The improvement ratio k_{SR} is maximized at $\Delta t \sim 100$ ms, where k_{SR} $\sim$1.8 and $\sim$2.1 for the narrow and the wide asterism, respectively. The displacements d with Δt=100 ms are 3.3 m and 0.7 m for the fastest and slowest layer in the model. While, as Δt is larger than 100 ms, k_{SR} is almost no or very week dependency on Δt. This suggests that only small displacement between the areas measured at the current and the previous time-step is enough to solve the degeneracy due to the *unoverlapped area*.

As mentioned before, the time scale of the frozen flow assumption is valid only within a short time. After the time scale of the frozen flow assumption, the phase distortion pattern of the atmospheric turbulence varies. If the time scale of the frozen flow is smaller than Δt for the multi time-step reconstructor, the measurement at previous time step can not be used for the information of the current time step because the phase distortion pattern is no longer kept. Guesalaga et al. [21] also investigated the time evolution of the atmospheric turbulence by using spatio-temporal cross-correlations of the measurements from multiple SH-WFSs installed in the GeMS, which is a MCAO system on the Gemini South. They found that the decay ratio of the correlation intensity for an individual layer, f_{decay}, decreases with the time delay for the correlation, Δt, and depends

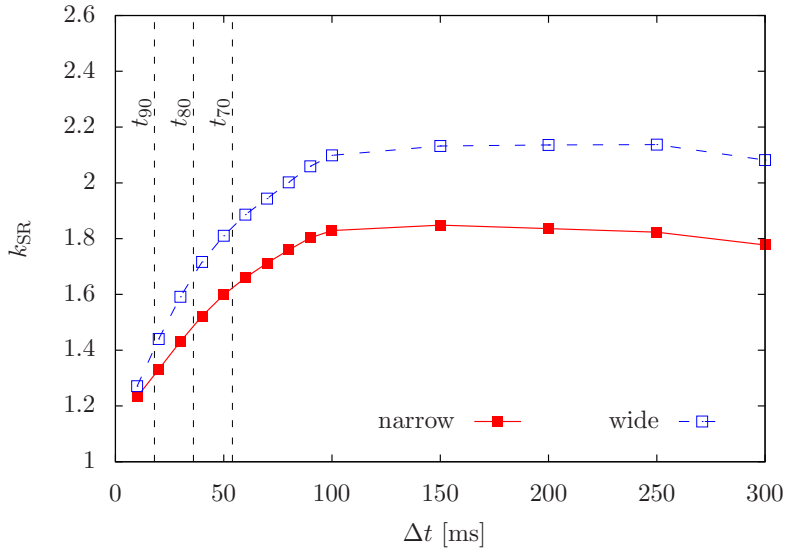

Figure. 4.5: Dependence of the multi time-step reconstructor on the Δt is presented in Fig. 4.5. The vertical axis in Fig. 4.5 is the SR improvement ratio, k_{SR}, which represents the ratio of the SR value achieved by the multi time-step reconstructor to the SR value from the single time-step reconstructor and is averaged over the angular separation from the center of the FoV. The result with the narrow asterism is indicated as the red filled squares, and the blue open squares shows the result with the wide asterism. The vertical dashed lines indicate the time duration that the decay ratio f_{decay} of the temporal correlation of SH-WFS measurements becomes 90 %, 80 %, and 70 %, that is, t_{90}, t_{80}, and t_{70}, wind assuming the wind speed is 33 $\mathrm{m\,s^{-1}}$, which is maximum value in the wind model.

on the distance travelled by the layer, d_{travel}. In their paper, the decay ratio are approximated as a function of Δt and v.

$$f_{\mathrm{decay}} = (-0.157v - 0.365)\Delta t + 1 \tag{4.2}$$

By using this equation, we can estimate Δt to keep the decay ratio f_{decay} to 90 %, 80 %, and 70 %, that is, t_{90}, t_{80}, and t_{70}, respectively. The dashed vertical lines in Fig. 4.5 show t_{90}, t_{80}, and t_{70} with assuming the fastest wind speed in the model, $v = 33$ $\mathrm{m\,s^{-1}}$. The time t_{70} is 54 ms for the fastest layer and 200 ms for the slowest layer with wind speeds of 7 $\mathrm{m\,s^{-1}}$. In order to keep the decay ratio of more then 70 % for all altitudes, Δt should be equal to or shorter than 54 ms. It is noted again that the effect of the decay ratio on the performance of the multi time-step reconstructor is still not quantitative. On-sky experiments and validations are necessary to evaluate the influence of the frozen flow assumption.

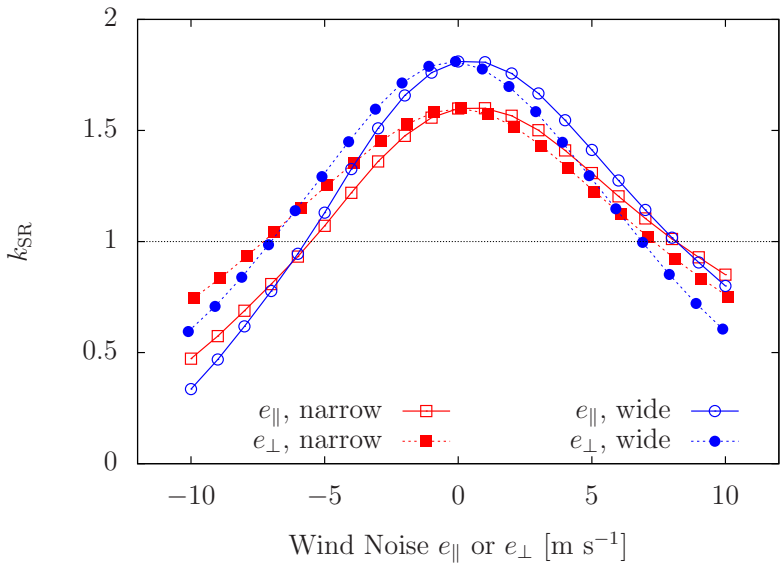

Figure. 4.6: SR improvement ratio, k_{SR}, achieved by multi time-step tomographic reconstruction with different *wind speed errors* $e_{\parallel}$ (the filled symbols) or *wind direction errors* $e_{\perp}$ (the open symbols). The results with the narrow asterism are represented as the red squares and the results with the wide asterism are the blue circles. The SR ratio less than 1 means that the performance of the multi time-step reconstructor is poorer than the performance achieved by the single reconstructor due to the wind estimation error.

4.2.3 Effect of Uncertainty of Wind Speeds and Direction

We discuss an effect from uncertainties of wind speed and direction. The errors of wind speed and direction result in an error of the spatial displacement between the areas measured by the current and the previous time-step. Here, we represent the wind error as $\boldsymbol{e} = (e_{\parallel}, e_{\perp})$. The first one, $e_{\parallel}$, is an error parallel to the wind direction and referred to as *wind speed error*. The second, $e_{\perp}$, is an error perpendicular to the wind direction and referred to as *wind direction error*. Fig. 4.6 shows the improvement ratio k_{SR} achieved by the multi time-step reconstructor comparing to the single time-step reconstructor with different errors of wind speed and direction, with both of the narrow (red symbols) and wide (blue symbols) asterisms. We assume the same wind error for all atmospheric layers and Δt=50 ms for the multi time-step reconstructor. The curve of k_{SR} with the *wind direction error* $e_{\perp}$ is symmetric with respect to the point $e_{\perp} = 0$. The multi time-step reconstructor has the advantage comparing to the singe time-step reconstructor, $k_{\mathrm{SR}} > 0$, as -7 m s$^{-1} \leq e_{\perp} \leq 7$ m s^{-1} for the condition we use for both asterisms. This corresponds that the error of the spatial displacement is less than 0.35 m and that the error of angle of wind direction is less than 12 degrees for the fastest layers with 33 m s^{-1} wind and 45 degrees for the slowest layer with 7 m s^{-1} wind.

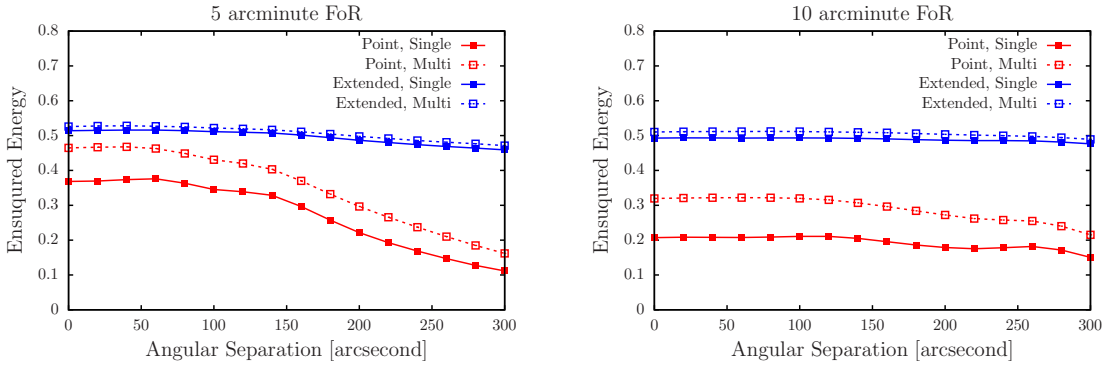

Figure. 4.7: Ensqured energy profiles with the narrow (left) and wide (right) asterism. As the target intensity profile, the point source and extended source are considered. The extended source is assumed to be an exponential profile with an effective radius of 0.1 arcsecond. The EE values are measured from the simulated PSF images (red) with a 50 mas box for the point source, and the exponential profile convolved with the simulated PSF (blue) with with a 300 mas box for the extended source. The solid lines indicate the results with the single time-step reconstructor, and the dotted lines are the EE profiles of the multi time-step reconstruction with Δt=50 ms.

For the *wind speed error* $e_{\parallel}$, the multi time-step reconstructor affected more by negative $e_{\parallel}$, which is an error in opposite direction to the wind, than positive $e_{\parallel}$. This is because $e_{\parallel}$ is negative, the covered areas are shorted than if $e_{\parallel}$ is positive. The allowable range for $e_{\parallel}$ is $-5.5\ \mathrm{ms}^{-1} \leq e_{\parallel} \leq 8\ \mathrm{ms}^{-1}$ for the wide asterism and $-5\ \mathrm{ms}^{-1} \leq e_{\perp} \leq 7\ \mathrm{ms}^{-1}$ for the narrow asterism. The dependence of the multi time-step reconstructor on the wind errors depends on the turbulence power, wind speed, direction and Δt for the multi time-step reconstructor. If the turbulence powers are stronger, the influence from the uncertainty of wind speed and direction is larger. Using larger Δt also makes the tomographic error due to the wind uncertainty larger because the spatial displacement error gets larger.

4.2.4 Detected Number of High Redshift LBGs

We evaluate the gain in multiplicity by the multi time-step reconstruction with respect to the detected number of high redshift LBGs. The parameters used in the evaluation are same as Table1.1, except for the AO performance. As the AO performance for the point source, we use the EE values measured from PSF images simulated in the numerical simulation. The extended source is assumed to be an exponential intensity profile with an effective radius of 0.1 arcseconds. The EE value of the extended source is estimated from the the exponential profile convolved with the simulated PSF image.

	5 arcminutes	10 arcminutes
single	3.83 (0.83)	5.99 (2.22)
multi	6.40 (2.96)	11.60 (8.06)

(a) $z \sim 5$, Point source, 10 hours

	5 arcminutes	10 arcminutes
single	1.26 (1.12)	4.29 (4.31)
multi	1.35 (1.26)	4.63 (4.78)

(b) $z \sim 5$, Extended source, 20 hours

	5 arcminutes	10 arcminutes
single	1.71 (0.32)	2.59 (0.84)
multi	3.00 (1.30)	5.22 (3.43)

(c) $z \sim 6$, Point source, 30 hours

	5 arcminutes	10 arcminutes
single	0.13 (0.11)	0.41 (0.41)
multi	0.14 (0.13)	0.46 (0.48)

(d) $z \sim 6$, Extended source, 30 hours

Tab. 4.3: Detected number of high redshift LBGs at $z \sim 5$ and 6. These are computed with the observed luminosity function from [7], the simulated EE profile shown in Fig. 4.7, and the parameters used in 1.4.4. The values in and out of the parenthesis indicates the detected number with the narrow and wide asterism, respectively.

The simulated EE values at J-band as a function of angular separation from the center are plotted in Fig. 4.7. The time difference for the multi time-step reconstruction is $\Delta t = 50$ ms. In the figure, the EE values for the point source, which is defined with a 50 mas box and represented by the red plots in Fig. 4.7, have a similar trend to the SR values at H-band shown in Fig. 4.3, but the absolute values are different due to the difference in the simulated wavelength. In the case of the extended object, the EE profiles, defined with a 300 mas, box are flatter than the EE profiles for the point source, and the difference between the narrow and wide asterism is very small. This is because the effective radius of 0.1 arcsecond is larger than the FWHM of simulated PSF, and as a result, the EE values are dominated by the original intensity profile rather than the convolved PSF. Therefore, the difference between the single and multi time-step reconstruction is also small for the extended object.

Using the EE values shown in Fig. 4.7 and the observed luminosity function from [7], we compute the detected number of LBGs at $z \sim 5, 6$, which are summarized in Table 4.3. The values in and out of the parenthesis are the detected number with the narrow and wide asterism, respectively. If the high redshift LBGs are point sources, the detected number of LBGs gets 3 times larger by the multi time-step reconstruction with the FoR of 10 arcminute diameter compared with the single time-step reconstruction with the 5 arcminutes FoR for both redshift ranges. In the case of the extended object, as expected from the EE profiles shown in Fig. 4.7, there is almost no difference in the detected number of LBGs between

	5 arcminute		10 arcminute	
	Single	Multi	Single	Multi
$\boldsymbol{s}$	45,248	90,496	45,248	90,496
$\boldsymbol{\varphi}$	29,768	59,536	29,768	59,536
$\boldsymbol{\phi}$	40,616	41,777	60,672	62,059
	1.35×10^9	5.39×10^9	1.35×10^9	5.39×10^9
$\boldsymbol{\Gamma_\alpha}$	180,992	361,984	180,992	361,984
	0.013 %	0.007 %	0.013 %	0.007 %
	1.21×10^9	2.49×10^9	1.81×10^9	3.70×10^9
$\boldsymbol{P_\alpha}$	658,800	1,318,960	658,628	1,318,788
	0.055 %	0.053 %	0.036 %	0.036 %
	1.65×10^9	1.75×10^9	3.68×10^9	3.85×10^9
$\boldsymbol{L}$	200,999	206,774	300,911	307,816
	0.012 %	0.012 %	0.008 %	0.008 %

Tab. 4.4: The three rows from the top show the number of WFS measurements, phase points of the atmospheric turbulence layers, and the phase points on the aperture plane. The assumed parameters are listed in Table 4.1. Other rows indicate the number of total elements, non-zero elements, and the number ratio of the non-zero elements to the total elements of the matrices of $\boldsymbol{\Gamma_\alpha}$, $\boldsymbol{P_\alpha}$, and $\boldsymbol{L}$.

the single and multi time-step reconstruction because of the extent of object itself. The size of the FoR is more important than the EE values for the extend case. Furthermore, the multi-object spectroscopy of the extend LBGs at $z \sim 6$ is difficult even if we use the MOAO system and the future ELT.

4.2.5 Computation Efficiency with GPGPU

Until the previous section, we assume that the computational complexity of the tomographic wave-front reconstruction is negligible. In reality, however, it is the critical issue in the ELT-scale tomographic reconstruction. At end of this chapter, we present our result regarding the computation efficiency with GPGPU for the ELT-scale tomographic reconstruction.

As mentioned in Section 2, the tomographic wave-front reconstruction is solved iteratively by the CGM with the diagonal-scaling matrix. We use the GPU computation for this calculation with a graphic board of Tesla K40. The code is written with C++ for CPU computation and *CUDA* with a version of 6.0 for the GPU computation. The CUDA is the C-like programming code for GPU developed

by the NVIDIA. We use GPGPU packages of *CUSPARSE* for the sparse matrix computations and *CUBLAS* for the vector computations.

The basic parameters and the turbulence profile used for this analysis are the same as that shown in Table 4.1 and Table 4.2. We used the narrow asterism with a FoR of 5 arcminute diameter and the wide asterism with a FoR of 10 arcminute diameter, which are shown in Fig. 4.1. The numbers of all elements of the vectors and the matrices are summarized in Table 4.4. For the matrices, the number and the sparse rate, which is the number rate of non-zero elements, are also listed. The all matrices have the sparse rate less than 1 %. We assume that there are 20 science targets.

The process of the CGM is summarized in Table 4.5 and Table 4.6. First, the measured slopes are transferred to the memory of the GPU from the memory of the CPU because the GPU needs to compute in own memory space. The data transfer between CPU–GPU relatively takes time compared with the data transfers between CPU–CPU or GPU–GPU.

The matrix $\boldsymbol{A}$ is a coefficient matrix as

$$\boldsymbol{A} = \boldsymbol{M}(\boldsymbol{P}_{\boldsymbol{\alpha}}^T \boldsymbol{\Gamma}_{\boldsymbol{\alpha}}^T \boldsymbol{\Gamma}_{\boldsymbol{\alpha}} \boldsymbol{P}_{\boldsymbol{\alpha}} + \sigma_\eta^2 \boldsymbol{L}^T \boldsymbol{L}) \boldsymbol{M}^T, \tag{4.3}$$

where a matrix $\boldsymbol{M}$ is a diagonal scaling matrix. In order to keep the $\boldsymbol{A}$ to be a symmetric matrix, $\boldsymbol{A}$ is multiplied by $\boldsymbol{M}$ from the both the left and right sides. In sparse matrix-vector multiplication, the computation time depends on the number of the non-zero elements in a matrix. If Eq. (4.3) is pre-computed before the CGM, the number of the non-zero elements gets larger than the sum of the non-zero elements of the matrices in Eq. (4.3). As a result, using pre-computed $\boldsymbol{A}$ for a matrix-vector multiplication increases the computation time compared with multiplying a vector by the matrices in Eq. (4.3) in each a matrix-vector multiplication. Therefore, we do not pre-compute $\boldsymbol{A}$. Since all required matrices are transferred to the GPU off-line and kept in the GPU during the control, the transfer time for the matrices are not included in this analysis.

The convergence is checked at the process 7 and 17 in Table 4.5 and Table 4.6. The criteria for the convergence is determined by the relative error with respect to the norm of the right-hand-side vector in Eq. (2.22) and the coefficient a (i.e, if $c_i < ac_0$, we consider that the CGM convergences). We set a to 10^{-3} empirically. If a is smaller values than 10^{-3}, there is almost no improvement in the residual WFE and the required number of iteration increases. If a is larger than 10^{-3}, the number of iteration decreases but the residual WFE increases.

1.	Transfer $\boldsymbol{s_\alpha}(t)$	To GPU from CPU
2.	$\boldsymbol{b} = \boldsymbol{P}_{\boldsymbol{\alpha}}^T \boldsymbol{G}_{\boldsymbol{\alpha}}^T \boldsymbol{s_\alpha}(t)$	the right-hand-side vector
3.	$c_{\text{criteria}} = a\lvert\boldsymbol{b}\rvert$	compute criteria for the convergence
		a is a relative convergence criteria
4.	$\boldsymbol{r_0} = \boldsymbol{b} - \boldsymbol{A x_0}$	initial residual
5.	$\boldsymbol{p_0} = \boldsymbol{r_0}$	initial search direction
6.	$c_0 = \lvert\boldsymbol{r_0}\rvert$	
7.	Check convergence	
8.	$for \;\; i = 1 \ldots N_{\max}$	Loop
	loop	12–19 in Table 4.5
	end	
9.	$\hat{\boldsymbol{\phi}}(t) = \boldsymbol{M}^T \boldsymbol{x_{\text{est}}}$	$\boldsymbol{x_{\text{est}}}$ is an estimates computed in the loop of step 8.
10.	$\hat{\boldsymbol{\varphi}}_{\boldsymbol{\beta}}(t) = \boldsymbol{P_\beta} \hat{\boldsymbol{\phi}}(t)$	Compute the wavefront in the science direction $\boldsymbol{\beta}$
11.	Transfer $\hat{\boldsymbol{\varphi}}_{\boldsymbol{\beta}}(t)$	To CPU from GPU

Tab. 4.5: Computation flow of the CGM.

Process in the loop		
12.	$\boldsymbol{q_{i-1}} = \boldsymbol{A p_{i-1}}$	
13.	$\gamma_{i-1} = \boldsymbol{p_{i-1}} \cdot \boldsymbol{p_{i-1}}$	
14.	$\boldsymbol{x_i} = \boldsymbol{x_{i-1}} + \gamma \boldsymbol{p_{i-1}}$	update the estimate
15.	$\boldsymbol{r_i} = \boldsymbol{r_0} + \gamma \boldsymbol{q_{i-1}}$	update residual
16.	$c_i = \lvert\boldsymbol{r_i}\rvert$	
17.	Check convergence	
18.	$\delta = c_i / c_{i-1}$	
19.	$\boldsymbol{p_i} = \boldsymbol{r_i} + \delta \boldsymbol{p_{i-1}}$	update search direction

Tab. 4.6: Computation flow in the loop of the CGM.

The computational time for each process of the CGM is summarized in Table 4.7 and Table4.8. We estimate the computational time with the single and multi time-step tomographic reconstruction for the narrow and wide asterisms. The Δt for the multi time-step reconstruction is 50 ms, and the one previous measurement is used for the multi time-step reconstruction.

Although the area of the FoR for the wide asterism is 4 times larger than the FoR area for the narrow asterism, the difference in the computational time between the narrow and wide asterisms is only 60 μs in and out of the loop. Also, the multi time-step reconstruction uses the measurements at 2 frames, but the computational complexity of the multi time-step reconstruction is smaller than the double of the computational time of the single time-step reconstructor. These results show that the GPU computation is efficient for the large problem.

The computationally heaviest part is the matrix-vector computation in the process 2, 4, and 12. The process 12 in the loop takes 459–699 μs, depending on the case, and accounts for 80–85 % of the total computation time in one loop. The vector-vector operations in process 3, 6, 13–16, and 19 take a few tens μs, and these are much faster than the matrix-vector computations. If we assume that the wavefront in all 20 science directions are computed by one computer, the computational time at the process 10, in which the wavefronts in the science directions are computed from the reconstructed atmospheric turbulence layers, takes 168 μs. If the wavefront in each science direction is computed parallel by a different computer, it takes only 30 μs.

The data transfer time from CPU to GPU in the process 1 is the same for the all cases. This is because the data transferred in each computation is only the measurement at the current time-step, if the previous measurements are saved in the GPU memory. This data transfer takes 165 μs and is smaller than the matrix-vector computation, but accounts for around 10 % of the total time out of the loop. The final data transfer from GPU to CPU in the process 11 takes 211 μs for the system with one computer and 28 μs for the case of multiple computers.

The total computation times out of the loop are 1409–1760 μs for the case of one computer, and the total times in the loop are 579–831 μs, depending on asterism and reconstructor. The total computation time including the iteration is 96–162 ms, even if the diagonal scaling is used, and these are much larger than the required computational time of 1 ms. It is expected that using the warm start, in which the estimate at one previous time-step are used as the initial of the CGM at the current time-step, can reduce the number of iteration largely. However, if the number of iteration is one, the computational time of 1 ms can

not be achieved with the current computational time. In order to achieve the required computational time, accelerating the matrix-vector multiplication and data transfer between CPU and GPU are necessary, that is, the GPU itself should be improved.

In this section, we assume that the required computational time is 1 ms to minimize the temporal-lag error. However, the required computational time should be determined with considering not only the temporal-lag error, but also a guide star brightness and a WFS measurement noise. If the guide stars are faint and the effect of the measurement noise is larger than the temporal-lag error, the performance of the MOAO is improved by controlling the MOAO system more slowly.A simulation comparing the effect of the temporal lag-error and the measurement noise is required to determined the computational time to be achieved.

	Narrow		Wide	
process	single	multi	single	multi
1.		165		
2.	249	343	251	358
3.	57	67	61	57
4.	484	676	508	724
5.	9	9	8	9
6.	36	37	39	39
7.		Check convergence		
8.		*loop*		
9.	30	30	30	30
10.	168(37)	167(36)	168(37)	167(35)
11.		211 (28)		
Total time in one loop	579	773	620	831
Total time out of the loop	1409(1095)	1705(1391)	1441(1121)	1760(1445)
number of required iteration	257(165)	224(165)	302(203)	227(194)

Tab. 4.7: Computational time and the number of iteration for the convergence of the CGM. The unit for the computational time is μs. While the value out of the parenthesis at the processes of 10 and 11 are assumed to compute the wavefront for 20 science directions by one computer, the values in the parenthesis at these processes are assumed to compute the wavefront for 20 science directions by 20 computers, i.e, it is the computeion time for one science target direction. The tital computetinal times follow the same manner as the values at the processes of 10 and 11. The number of iteration is computed with and without the diagonal scaling preconditioner, where the values in the parenthesis are with the diagonal scaling preconditioner.

	Narrow		Wide	
process	single	multi	single	multi
12.	459	652	486	699
13.	13	39	39	40
14.	29	29	32	34
15.				
16.	34	34	35	35
17.	Check convergence			
18.	0	0	0	0
19.	19	19	20	22

Tab. 4.8: Computational time of the processes in the loop of the CGM

Chapter 5

Laboratory Test with RAVEN

5.1 RAVEN

RAVEN is a MOAO demonstrator installed and tested on the Subaru telescope at Maunakea [32], which is the first MOAO demonstrator at 8 m-class telescope. The RAVEN is designed not only to demonstrate the technical readiness associated with MOAO systems, but also to verify scientific capability of MOAO systems. The RAVEN can apply MOAO correction simultaneously for two science targets within a field of 2 arcminute diameter. The tomographic reconstruction is computed using the measurements from d by 3 NGSs within a FoR of 3.5 arcminute diameter and 1 LGS attached to the Subaru telescope [25] located at the center of the FoR.

There are 4 open-loop SH-WFSs (OL-WFS) for 3 NGSs and 1 LGS in the RAVEN. The measurements from the OL-WFSs are used for the tomographic wave-front reconstruction, SLODAR, the wind estimation, and the tracking of NGSs. There are two science channels each containing a DM to provide AO correction into its science target. Each science channel also has SH-WFS behind the DM and it is called closed-loop WFS (CL-WFS). This CL-WFS is used for the calibration of the system, measuring a raw or residual wave-front in science direction, providing SCAO mode correction, and tracking the science targets. All SH-WFSs consist of 10×10 subapertures and an Andor iXon 860 EMCCD. Each subaperture has a diameter of 0.8 m on the aperture plane and a 4.8 arcseconds FoV. The DMs are an ALPAO DM with 11×11 actuators. The light rays coming from NGSs and science targets are picked off by pick-off arms and fed to each OL-WFS or science channel. The light fed to science path is corrected by a DM. Then, the light divided into optical light and near infrared light by a beam splitter. The optical light is fed into the CL-WFS and the infrared light is sent into the Subaru Infrared Camera and Spectrograph (IRCS)[29]. The RAVEN also has a

Parameters	Values
Diameter of aperture	8 m
Number of NGSs	3
Number of LGS	1
FoR for NGS	3.5 arcminutes diameter
FoR for science target	2 arcminutes diameter
WFS	SH-WFS
Number of subapertures	10×10
Number of DM elements	11×11
Number of science targets	2
Maximum Frame rate	250 Hz

Tab. 5.1: Parameters of RAVEN.

Altitude [km]	$\int C_N^2 dh$ [10^{-14} $m^{1/3}$]	Fraction of C_N^2	wind speed [$m s^{-1}$] x	y
10.5	5.961	0.180	17.0	0.0
5.5	7.418	0.224	6.0	0.0
0	19.737	0.596	0.0	5.68
Total r_0[m]	0.156			

Tab. 5.2: Atmospheric turbulence profile and wind profile generated by the RAVEN CU.

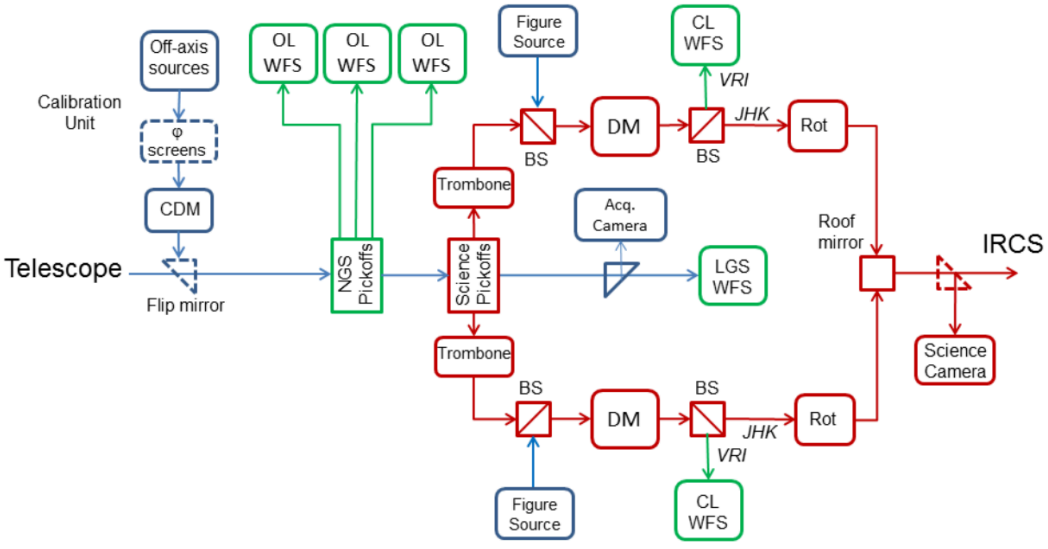

Figure. 5.1: Block diagram of the RAVEN system. *Figure adopted from Lardière et al. (2014)* [32].

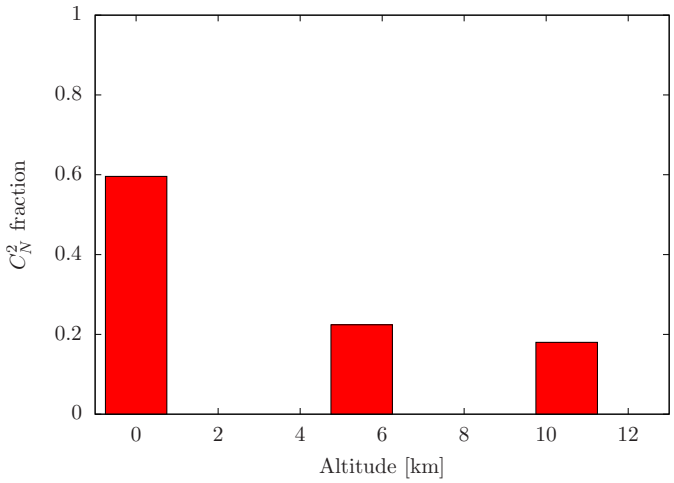

Figure. 5.2: Expected C_N^2 fraction generated by the RAVEN CU.

near infrared camera in the optical bench for the laboratory experiment without the IRCS. These parameters are listed in Table 5.1, and Fig. 5.1 show the block diagram of the RAVEN system.

RAVEN has a calibration unit (CU) on the optical bench, which simulates multiple GSs, multiple science targets, atmospheric turbulence layers, and a telescope [33]. The CU is used to calibrate and test the AO system. The atmospheric turbulences generated by the CU consist of three layers. Two high layers at altitude of 10 km and 5 km are simulated by phase screens, which can be rotated to simulates a movement of the turbulence layers due to the wind. The ground layer at 0 km is generated by a calibration DM with 17×17 actuators. The designed parameters in the CU are summarized in Table 5.2 and Fig. 5.2. It should be noted that the phase distortion patterns generated by the CU are periodic, and the period is 40 s for the 5 km layer and 19 s for the 10 km layer. Also, the atmospheric turbulence generated by the CU is 100 % frozen flow layer.

5.2 SLODAR and Wind Estimation

First, we test the SLODAR and the wind estimation method with the CU. An asterism is shown in Fig. 5.3. The NGSs are at approximately 60 arcsecond radius and the LGS is located at the center of the FoR. The brightness of the NGS is set to R∼8 mag, which is very bright and the WFS measurement error is minimal.

Fig. 5.4 and Table 5.3 show a turbulence profile estimated by the SLODAR. We use the slope for one minute from three OL-WFSs for the SLODAR and the wind estimation. The estimated profile has three major peaks at the almost

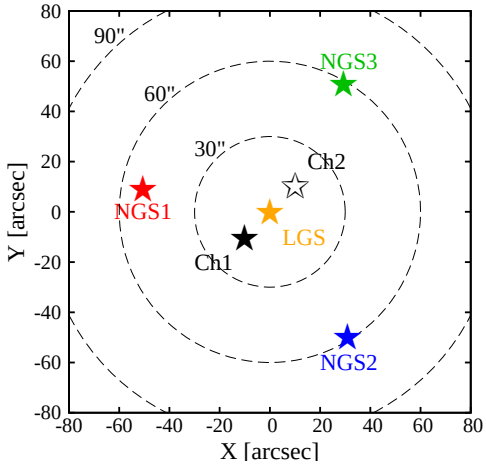

Figure. 5.3: Asterism of the GSs and the science targets for the laboratory test with the RAVEN.

Altitude [km]	$\int C_N^2 dh$ [10^{-14} $m^{1/3}$]	Fraction of C_N^2	wind speed [$m s^{-1}$] x	y
10	4.329	0.169	15.4	-0.6
8	0.896	0.035	8.6	-0.2
6	8.222	0.321	6.3	0.1
0	12.140	0.474	0.1	5.0
Total r_0[m]	0.182			

Tab. 5.3: Atmospheric turbulence profile and wind profile estimated by the SLODAR and the wind estimation method.

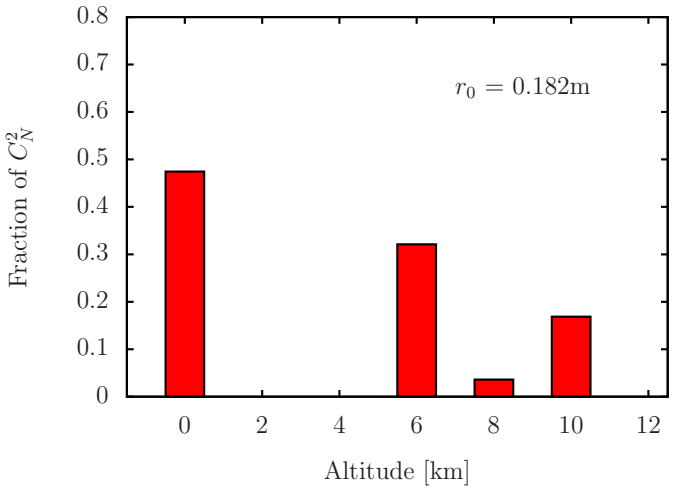

Figure. 5.4: Profile of atmospheric turbulence of the RAVEN CU estimated by the SLODAR.

same altitudes as the designed profile in Fig. 5.2. The smallest turbulence at 8 km in the estimated profile may come from the turbulence layers at 5.5 km or/and 10.5 km due to the mismatch of the altitude between the SLODAR and the designed turbulence layers. The largest difference between the designed and measured profiles is the C_N^2 value at ground layer, and the estimated value of 12.140×10^{-14} $\mathrm{m}^{1/3}$ is 60 % of the designed value. As a result, the total power measured by the SLODAR is smaller than the designed value, i.e., the measured r_0 of 0.182 m is larger than the designed r_0 of 0.156 m. The C_n^2 of the other high layers are consistent between the measured and the designed values.

This larger r_0 than the designed value is already reported in the previous estimation in the lab on RAVEN, which is estimated by a different SLODAR method from the one presented in this thesis. The difference between the two method is that, while the method presented in this thesis uses the correlation map of the slope form multiple SH-WFSs, which is defined in Eq. (2.26), the other method uses the covariance matrix of the slopes. The covariance matrix is defined as

$$Cov_{xx}^{\mathrm{obs}}(i,j,i',j') = \left\langle \sum_{\text{valid } i,j,i',j'} s_{i,j}^{\prime\prime x[1]}(t) s_{i',j'}^{\prime\prime x[2]}(t) \right\rangle, \tag{5.1}$$

where s'' is a slope after the tilt and average pattern subtraction defined in Eq. (2.25). Both methods fit the theoretical correlation or covariance matrix to the measured one to estimate $C_N^2(h)$. We refer to the SLODAR presented in this thesis as a *correlaton SLODAR*. The other SLODAR method is referred to as a *covariance SLODAR*.

The phase distortion at ground layer in the CU is generated by the calibration

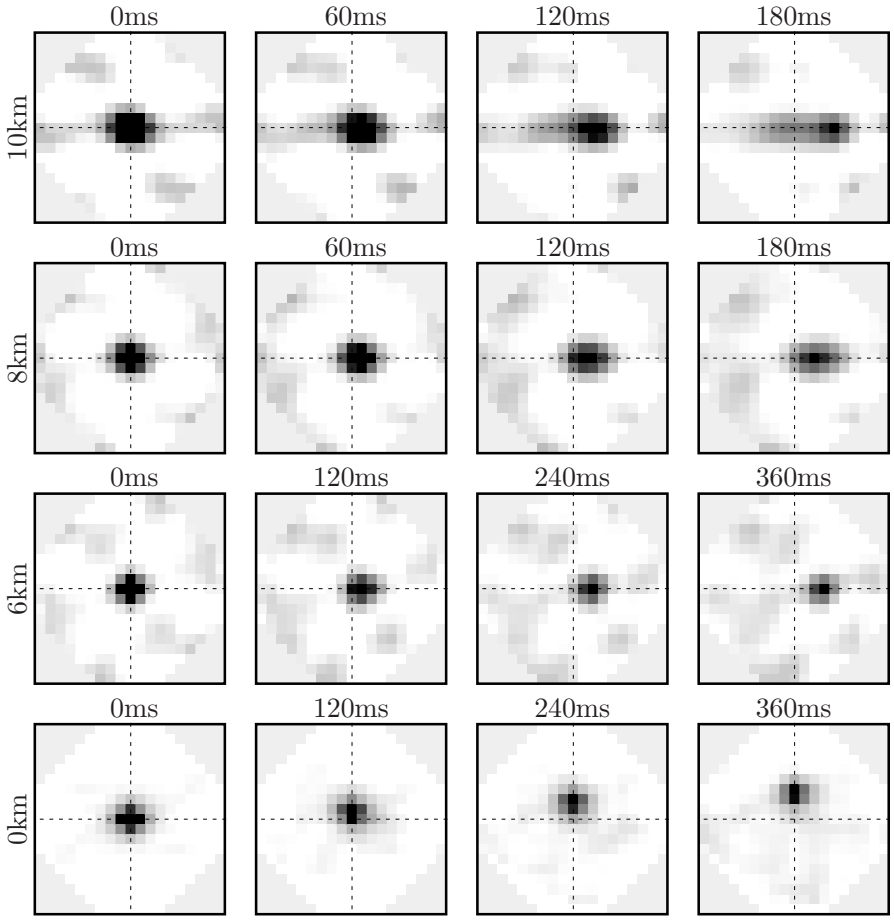

Figure. 5.5: Temporal correlation maps of slope at each altitude estimated by tomographic reconstruction. The values at the top of each image indicate the time delay used to drive the temporal correlation. The x and y-axes are δi and δj with a range of $-9 \leq \delta i, \delta j \leq 9$. One pixel on the temporal-correlation corresponds to one subaperture size, which is 0.8 m in the RAVEN

DM. Since the actuator size of the calibration DM is roughly 0.47 m, the DM can not reproduce the phase distortion with spatial scales smaller than 0.47 m. We conclude that the actuator size causes the discrepancy and that the estimated value reflects the real turbulence profile on the DM better than the designed value.

By using the estimated profile, we evaluate the wind speed and direction at each layer. First, we compute the tomographic reconstruction to reconstruct the phase distortion pattern at each altitude. Then, the temporal correlation map of the estimated slope are calculated with different delay times, δt. The temporal correlation maps are illustrated in Fig. 5.5. The delay time for the lower layers at 0 km and 6 km are set to larger than the higher layers (Fig. 5.5). Generally, the wind speed at low layer is considered slower than the wind speed at high altitude. In order to get clear movement of the temporal correlation peak, longer delay time is preferred for the low altitude layers. For all layers detected by the SLODAR, the peaks on the temporal correlation maps are detected. The estimated wind speeds and directions, which are summarized in Table 5.3, are consistent with the designed value. The error of the wind speed is less than 2 $\mathrm{m\,s^{-1}}$ for all layers, which is an acceptable wind error computed by the numerical simulation in Section 3. With this wind estimation error, the multi time-step reconstructor will work with the future MOAO system (see Fig. 4.6).

5.3 Multi Time-Step Reconstruction

We present the result of the laboratory test of the multi time-step reconstruction in Fig. 5.6 and the top table of Table 5.4. Fig. 5.6 shows the PSF images of two science channels taken by RAVEN infrared camera with the MOAO correction. The pixel scale of the PSF images in Fig. 5.6 is 17.5 mas, and the size of the images are 0.5 arcsecond $\times$ 0.5 arcsecond. The maximum wind speed simulated by the CU , which is 17.0 $\mathrm{m\,s^{-1}}$, is almost half of the maximum wind speed in the model that we used for the numerical simulation in Section 3, and the time duration that the decay ratio f_{decay} of the temporal correlation of SH-WFS measurements is more than 0.7 with the wind speed of 17.0 $\mathrm{m\,s^{-1}}$is $\sim$100 ms. Therefore, we use 100 ms for Δt of the multi time-step reconstructor. The asterism used for the MOAO experiment in the laboratory is the same as the asterism used for the SLODAR, which is shown in Fig. 5.3.

The performance of the MOAO is evaluated by SR, EE, and improvement ratios of the SR and the EE at wavelength of 1650 nm (H-band). First, we

perform a background subtraction to the original image observed by the science camera in RAVEN. Then, the PSF image of each science channel is cropped with 1 arcsecond × 1 arcsecond box from the original image and normalized by the total intensity within the cropped box. In parallel, we create a diffraction-limited PSF image by a simulation with a pixel scale of 1 mas and normalize the diffraction-limited PSF image within a 1 arcminute box. We estimate a SR by comparing the peak intensity in the observed PSF image with that in the diffraction-limited PSF image. Accurately, this SR is an EE within a 1 mas box , but the 1 mas box is small enough compared with the FWHM of the PSFs and it can be considered as a SR. The EE is computed within a 140 mas box, which is a size of the slit of the slope. The measured values are summarized in the top table of Table 5.4

Visually, the PSFs become sharper and have higher peak intensity by the multi time-step reconstruction compared to the single time-step reconstruction for both of the asterisms, as shown in Fig. 5.6. The EEs achieved by the single time-step reconstructor are 0.268–0290 without the LGS and 0.349–0.365 with the LGS. The improvement ratio of the EE achieved by the multi time-step reconstruction is 1.16–1.18 without LGS and 1.05 with LGS. The SR of the single time-step reconstructor without the LGS is 0.072–0.087 and these values are roughly consistent with the value of 0.10 measured previously in the laboratory experiment on RAVEN [32]. On the other hand, the SR of the single case with the LGS is 0.125–0.150, which is much lower than the previous value of 0.23. The improvement ratios of the SR achieved by the multi-time step reconstructor are 1.32–1.51 without the LGS and 1.22–1.25 with the LGS. These improvements show the multi time-step reconstruction works in the lab-test. The improvements in the SR and the EE are better without the LGS than with the LGS. In this laboratory experiment, since the part of the tomographic error due to the *uncovered* and *unoverlapped area* is solved with the LGS and the tomographic error would be dominated by the other components (e.g. the open loop error, the temporal lag-error, the optical error, and so on) rather than the *uncovered* and *unoverlapped area*. Therefore, the improvement by the multi time-step reconstruction becomes smaller relatively than the case without the LGS.

5.4 Comparison with a numerical simulation

We compare the results of the lab-test on the multi time-step reconstructor to a numerical simulation. We assume the parameters of the RAVEN system and the turbulence profile generated by the RAVEN CU, listed in Table 5.1 and Table

Lab-test		EE (140mas)		SR	
reconstructor	GSs	Ch1	Ch2	Ch1	Ch2
single	3NGSs	0.268	0.290	0.072	0.087
multi		0.313	0.343	0.095	0.131
Improvement ratio		1.16	1.18	1.32	1.51
single	3NGSs	0.349	0.365	0.125	0.150
multi	+LGS	0.367	0.385	0.153	0.187
Improvement ratio		1.05	1.05	1.22	1.25

Simulation		EE (140mas)		SR	
reconstructor	GSs	Ch1	Ch2	Ch1	Ch2
single	3NGSs	0.334(0.294)	0.346(0.303)	0.251(0.211)	0.267(0.224)
multi		0.406(0.348)	0.424(0.362)	0.361(0.302)	0.384(0.321)
Improvement ratio		1.21(1.18)	1.23(1.19)	1.44(1.43)	1.44(1.43)
single	3NGSs	0.443(0.379)	0.430(0.367)	0.398(0.333)	0.386(0.324)
multi	+LGS	0.477(0.402)	0.477(0.402)	0.465(0.390)	0.465(0.389)
Improvement ratio		1.07(1.06)	1.11(1.10)	1.17(1.17)	1.20(1.20)

Tab. 5.4: SR, k_{SR}, and EE value of each science channel measured in the lab-test (the top table) compared to those predicted from the numerical simulation (the bottom table). The EE is defined with a 140 max box. There are two GS configuration used in the test, one is only three NGSs and the other is three NGSs+LGS. The values in parenthesis in the lower part is the value accounting for the implementation errors.

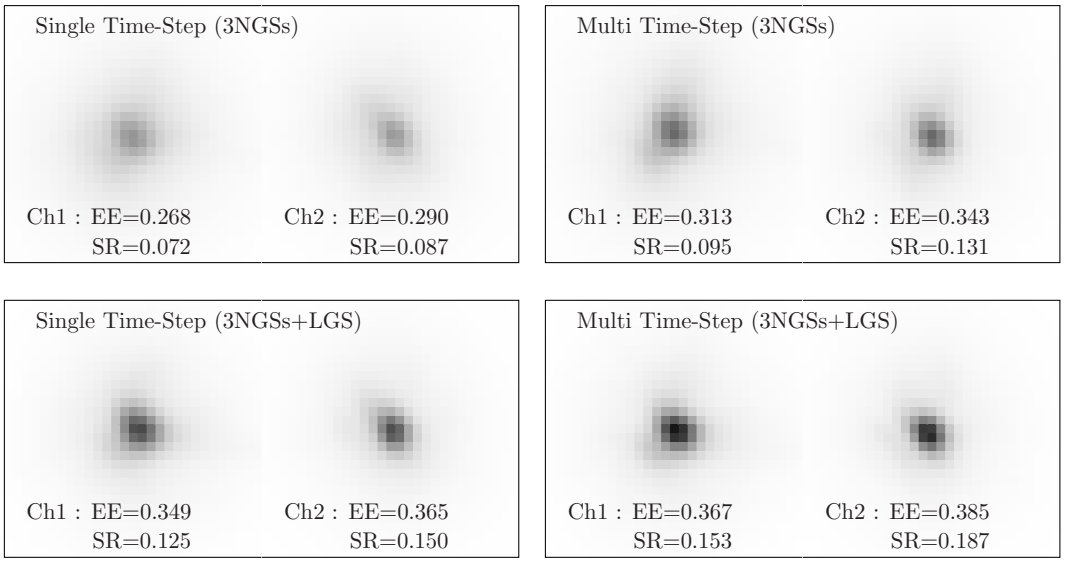

Figure. 5.6: PSF images of each science channel taken in the lab-test with the single and the multi time-step reconstructors. The color scale is linear and aligned for each channel. The wavelength is 1650 nm (H-band). The size of each image is 0.5 arcsecond × 0.5 arcsecond, and the pixel scale is 17.5 mas.

5.2. The coordinates of the GSs and the targets are also set to the same as the coordinates used in the lab-test, illustrated in Fig. 5.3. The EE values and the improvement ratio, k_{SR}, predicted by the simulation are summarized in the lower part of Table 5.4. There is a good agreement between the k_{SR} measured in the lab-test and derived by the simulation, therefore the performance improvement of the multi time-step reconstructor is as good as predicted for both asterisms with and without LGS. It is also consistent between the laboratory test and the simulation that the improvement by the multi time-step reconstruction without LGS is larger than the improvement without the LGS.

However, the absolute values of the EE and the SR measured in the laboratory experiment are much smaller than the values predicted by the simulation for both of the single and the multi time-step reconstructors. This difference may be due to the implementation errors not considered in the simulation, which are calibration error, DM control error, and optical aberration. In the calibration of RAVEN, there are two steps [28]. The first one is to find the rotation matrices, which compensate the misalignment between the OL-WFSs and the CL-WFSs. In particular, in RAVEN, OL-WFSs are rotated respect to the CL-WFSs. The second one is to determine the command matrices to control the science DMs. The rotation and command matrices are determined experimentally using the CU and the CL- and OL-WFSs. Therefore, these include the noise.

The calibration error results from the uncertainties of these matrices. The DM

control error is regarding to the accuracy and long term stability of the DM, i.e., how the DM can reproduce the demanded wave-front. The optical aberration is a static error caused by the misalignment in the system. The optical aberration in the science path can not be seen from the OL-WFSs, and therefore, this aberration can not be corrected by the tomography. This aberration is called non-common path aberration (NCPA). We set to the reference shape of the DMs to remove the static optical aberration [31], but the residual aberration may affect the MOAO performance. Anderson et al. (2012) [4] simulates the performance of the RAVEN and estimates the error budget of the AO correction of the RAVEN system. They estimate a wavefront error (WFE) caused by the implementation errors of the RAVEN to be 107 nm.

In order to evaluate the contribution from the implementation errors, we calculate the total WFE as a quadrature sum of WFE due to the implementation and tomographic errors. The WFE due to the tomographic error is estimated from the SR derived from the simulation by using an approximation, SR=$\exp[-\sigma^2]$, where $\sigma = 2\pi\mathrm{WFE}/\lambda$ and λ=1650 nm. It is noted that this expression is valid for $\sigma^2 < 1$ rad^2 (this is SR$<$ 0.37), and our result can be biased when SR is lower than 0.37. The SR, including the tomographic error and the implementation errors, can be computed with this approximation from the total WFE. Since there is no approximation connecting to EE and WFE, we assume that the absolute loss of the EE due to the implementation errors is same as the absolute loss of the SR. The performance predicted by the simulation, accounting for the implementation errors, are listed in the bottom table of Table 5.4 as the values in a parenthesis. While the simulated EE including the implementation errors is slightly higher than the EE values measured in the laboratory experiment, the simulated SR including the implementation errors is still much higher than the measured SR. This suggests that there are additional errors, which make a PSF peak blurred and affects mostly SR values. The improvement ratios does not vary with the implementation errors.

As the additional errors, we examine the effect of the residual tip-tilt components. Since the tip-tilt errors change the position of the PSF, the fluctuation of the tip-tilt errors affects strongly the SR of the long-exposure PSF. On the other hand, the EE is expected to be less sensitive to the tip-tile error than the SR because the EE is evaluated within a 140 mas box which is larger than the FWHM of the corrected PSF. In the simulation, the standard deviations of the residual tip-tilt errors are roughly 6.5 mas for both of the x and y-direction. The residual tip-tilt error in the laboratory experiment can be estimated from the CL-WFS measurements, and the standard deviations of the residual tip-tilt errors is 15 mas

for x-direction and 20 mas for y-direction in the laboratory experiment. These are much larger than that of the simulation and suggest that the results in the laboratory experiment are affected more by the tip-tilt errors than the result of the simulation. The sparse approximation of the inverse of the phase covariance matrix, $\boldsymbol{L}$, may contribute the uncorrected additional tip-tilt errors in the laboratory test because the sparse approximation can not regularize the tip-tilt modes [35]. The standard deviations of the tip-tilt modes of the uncorrected wave-front are 55 mas in the simulation and 50 mas in the laboratory experiment. Therefore, the additional vibration from the RAVEN does not affect the result in the laboratory experiment.

In order to evaluate the contribution from the tip-tile errors, we add the tip-tilt errors to the corrected wave-front in the simulation so that the standard deviation of the tip-tilt errors in the simulation becomes equal to that of the laboratory experiment. The re-simulated values with the additional tip-tilt errors are listed in Table 5.5. The values in a parenthesis in Table 5.5 is the SR including the effect of the implementation errors. As expected, while the SR is affected strongly on the additional tip-tile errors, there is almost no change in the EE due to the additional tip-tile errors. The simulated SRs including the effect of the uncompensated tip-tilt and the implementation errors are much closer to the measured values than the original simulated SRs in Table 5.4, but these are still higher than the measured values.

In this section, we compare the result in the laboratory with the numerical simulation and discuss the effect of the implementation errors and residual tip-tile errors to explain the lower SRs and EEs in the laboratory experiment than that of the simulation. With considering these effects, the difference between the result of the laboratory experiment and the simulation gets smaller, but the SRs and EEs of the laboratory test are still lower than the values predicted by the simulation. In order to understand what makes this difference, more experiments to examine the implementation errors in detail are required.

Simulation		EE (140mas)		SR	
reconstructor	GSs	Ch1	Ch2	Ch1	Ch2
single	3NGSs	0.326	0.337	0.137(0.116)	0.149(0.126)
multi		0.397	0.413	0.194(0.164)	0.204(0.173)
Improvement ratio		1.22	1.23	1.42	1.37
single	3NGSs	0.432	0.418	0.213(0.180)	0.211(0.179)
multi	+LGS	0.466	0.464	0.250(0.212)	0.247(0.209)
Improvement ratio		1.08	1.11	1.17	1.17

Tab. 5.5: SR, k_{SR}, and EE value of each channel predicted from the numerical simulation with taking account of the additional tip-tilt errors. The additional tip-tilt errors are determined by the measurement on the laboratory experiments. The values in a parenthesis in Table 5.5 is the SR including the effect of the implementation errors.

Chapter 6

On-Sky Evaluation with RAVEN

6.1 On-Sky Performance

The on-sky engineering and science observations with RAVEN on the Subaru telescope are successfully performed on May and August 2014 and June 2015. We test the multi time-step reconstruction and the wind estimation method on sky during the third observation on June 2015. In this chapter, we present the on-sky performance of the SLODAR, the wind estimation, and the multi time-step reconstruction based on the data from the third on-sky observation.

6.1.1 Engineering Field

The engineering fields of the third run are shown in Fig. 6.1. The green points in the figure indicate the position of the NGSs and its magnitude at R-band are listed in Table 6.1. All NGSs are brighter than R=12.6. The limit magnitude of OL-WFSs in RAVEN is around 14 mag at R-band. Target objects are selected in radius of 1 arcminute from the center.

6.1.2 SLODAR

The performance of the SLODAR of RAVEN in the first and second on-sky observations is reported in [32]. The result of the SLODAR in [32] is computed by the covariance SLODAR method. The covariance and correlation SLODAR are implemented in RAVEN and provide the almost same results, but the computation time of the covariance SLODAR is a few seconds faster than the correlation SLODAR, where the covariance SLODAR takes around 5 seconds for its computation and the correlation SLODAR takes around 10 seconds. Therefore, the covariance SLODAR is usually used during on-sky observations.

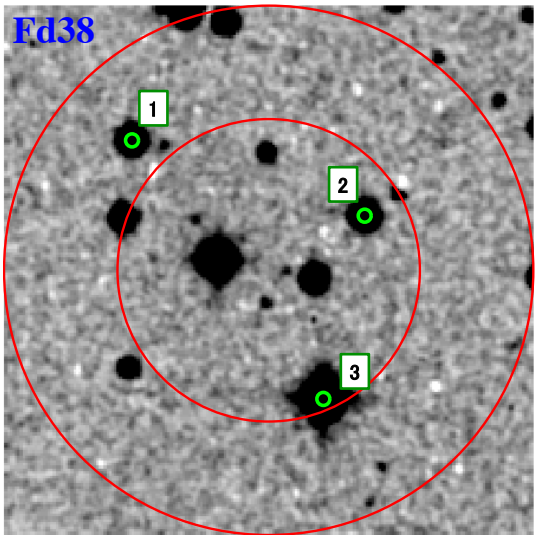

(a) Fd38

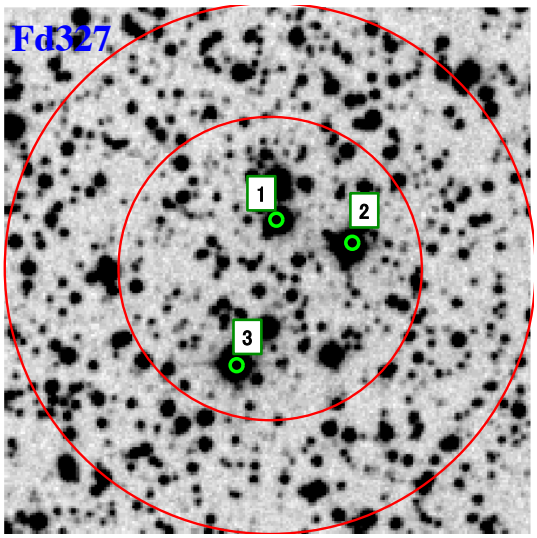

(b) Fd327

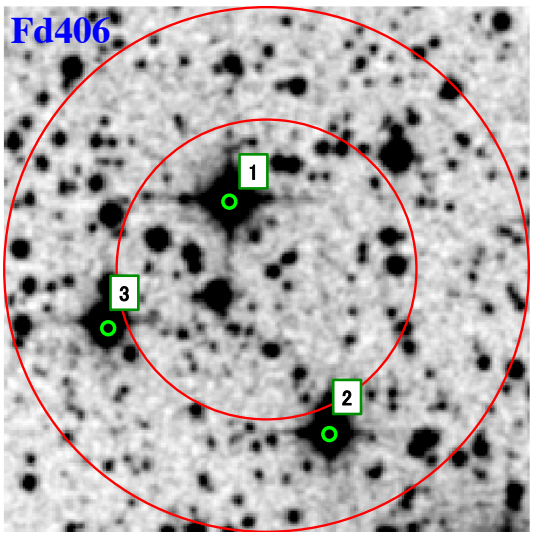

(c) Fd406

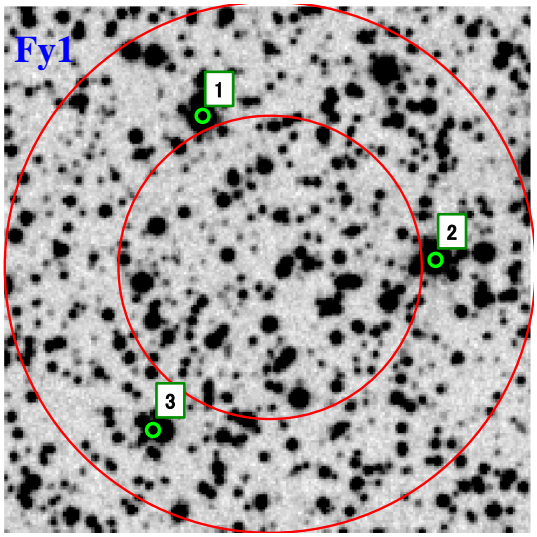

(d) Fy1

Figure. 6.1: Images of the engineering fields. The red lines indicate the radius of 1.75 arcminute and 1 arcminute from the center of the field. The green points represent the NGSs position. The brightnesses of the NGSs are summarized in Table 6.1. The information of the engineering field is summarized in Table 6.1. These images comes from the Digital Sky Survey. The position of NGSs are plotted based on the USNO-A2.0 catalog.

Field ID	RA	Dec
Fd38	15:15:30	+5:15:57
	NGS	Rmag
	1	12.2
	2	12.5
	3	10.2

(a) Fd38

Field ID	RA	Dec
Fd38	19:45:00	+33:14:41
	NGS	Rmag
	1	11.0
	2	10.6
	3	11.0

(b) Fd327

Field ID	RA	Dec
Fd38	20:11:28	+35:51:58
	NGS	Rmag
	1	11.4
	2	12.6
	3	12.0

(c) Fd406

Field ID	RA	Dec
Fd38	19:45:26	+33:25:32
	NGS	Rmag
	1	10.9
	2	10.6
	3	11.4

(d) Fy1

Tab. 6.1: RA, Dec, and NGS magnitudes of the engineering field shown in Fig. 6.1. The NGSs magnitude are referenced from the USNO-A2.0 catalog.

Fig. 6.2 shows an example of the C_N^2 profile and the cross-correlation maps computed from one minute series of the on-sky measurements by the correlation SLODAR. The field is Fd38. In the profile, the ground layer has more than 80 % of the total turbulence power and the weak turbulences are at around 12 km. Only one central peak is seen on the cross-correlation maps, which corresponds to the ground layer. Fig. 6.3 shows another example of a SLODAR result with C_N^2 profile with a significant component at high altitudes. The field is Fd406. The turbulences spread over a wide range of altitudes and 50 % of the total turbulence power occurs at the altitudes higher than 10 km. On the cross-correlation maps, there are strong correlations along the base lines of the NGS pairs.

In most of the time during the on-sky observations, we detect a strong ground layer as expected [16]. Fig. 6.4 shows a histogram of the ground layer fraction measured by the covariance SLODAR during the on-sly observations. The ground layer accounts for the 50 % of the total turbulence power at 75 %-ile. This strong ground layer suggests the large contribution from the dome seeing.

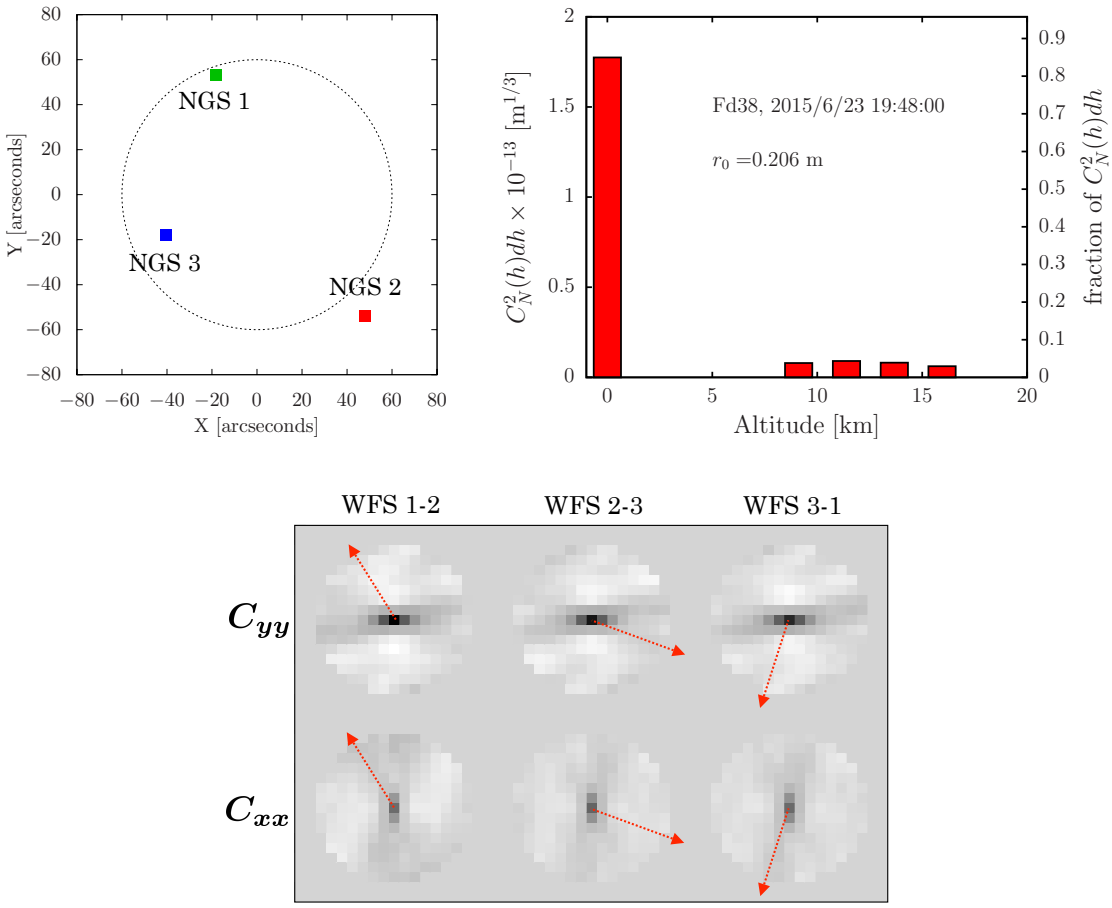

Figure. 6.2: The example of the SLODAR result dominated with a grund layer. The upper left panel shows the NGS asterism and the dashed circle indicates the angular separation of 60 arcseconds from the center of the FoR. The upper right panel shows the C_N^2 profile estimated by the correlation SLODAR and the bottom panel shows the corresponding correlation maps. The red arrows indicate the baseline of the guide stars, and the signals of the correlation are expected to apper along these arrows. In this case, most of the turbulence is concentrated in the ground layer and there are weak turbulences at around 12 km.

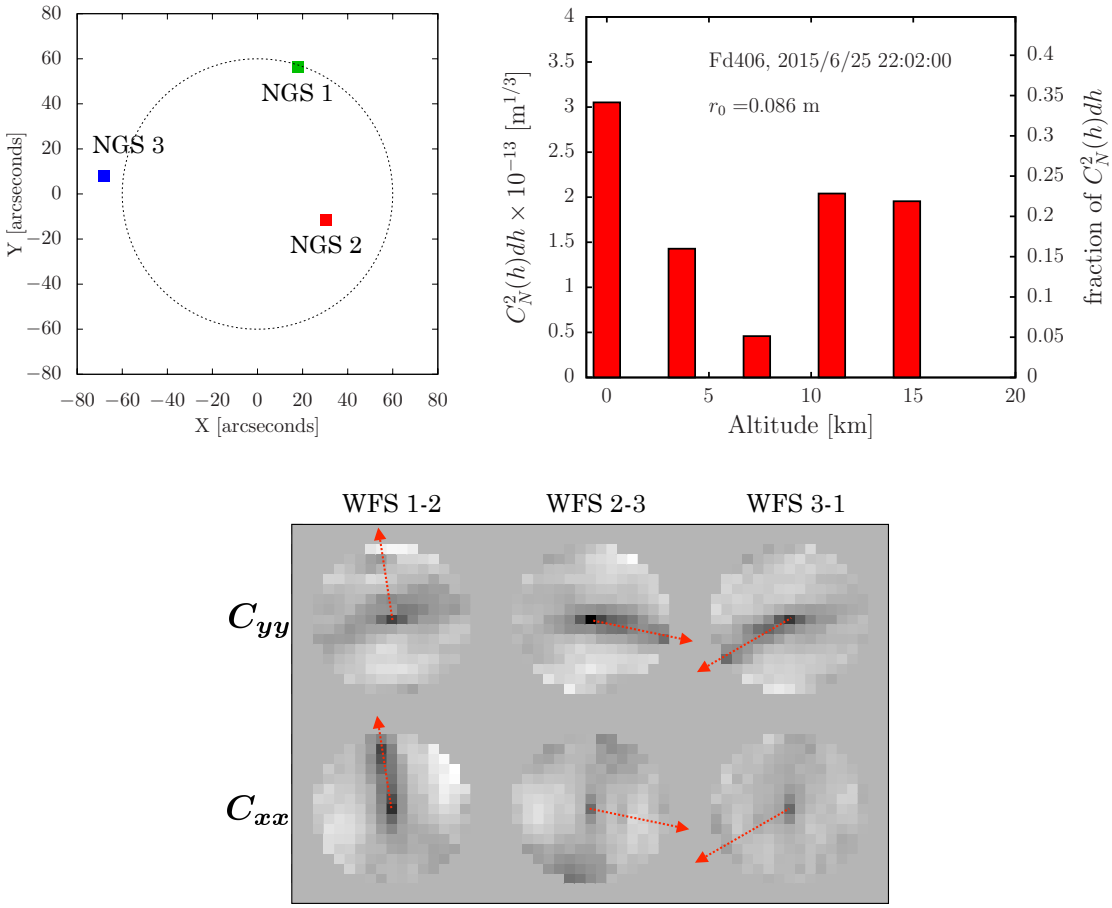

Figure. 6.3: Another example of the SLODAR result with a complex profile. The turbulences occur over wide range of altitudes and the turbulences at altitude higher than 10 km have significant contribution to the total turbulence power. On the correlation maps, there are strong correlations along the base lines of the NGS pairs

6.1.3 Wind Estimation

Fig. 6.5 and Fig. 6.6 show the wind speeds, wind directions, and the temporal-correlation maps with different time delays, δt, at each altitudes for the cases of Fig. 6.2 and Fig. 6.3, respectively. In Fig. 6.5, which is the result of the profile dominated with a ground layer, a peak on each temporal-correlation map seems not to move from the center even with increasing the time delay, δt, up to 100 ms. This suggests that there is slow or not moving component at all altitude. As a result, the measured wind speeds are 1 $\mathrm{m\,s^{-1}}$at all altitudes. The measured directions are different between the ground layer and high altitude layers.

On the other hand, in Fig. 6.6, which is the case that the turbulences spread over a wide range of altitudes, the peaks on the temporal correlation maps slowly move to left with the increase of δt, except for the ground layer. The measured wind speeds are almost 0 $\mathrm{m\,s^{-1}}$at 0 km and around 5 $\mathrm{m\,s^{-1}}$at higher altitudes.

In most of the time during the on-sky observations, we detect temporal-correlation peak moving slowly or not moving with the time delay δt. These peaks are seen at all altitudes as shown in Fig. 6.5 and Fig. 6.6. As a result, the average of the detected wind speeds are very small, which are equal to or less than 1 $\mathrm{m\,s^{-1}}$, for all altitudes.

Although, at low altitudes, this slow wind speeds is not strange because the average wind speed at low altitudes are generally considered to be slow compared with wind speeds at high altitudes [24], there would be some contributions from the dome seeing. The turbulence caused by the dome seeing may be boiling rather than moving with the wind. As explained in Chapter 2, we subtract the temporal average over a minute from the reconstructed slopes before computing the temporal-correlations in order to remove the static pattern in one minute. If the temporal evolution of the dome seeing is faster than 1 minute, it makes the correlation peak on the temporal-correlation map of low altitudes, which does not move with δt. As a result, the estimated wind speeds get small due to the dome seeing.

For the high altitudes, these slow wind speeds and the temporal correlation peak without moving are not considered to reflect the real wind speeds, since the average wind speeds is faster than 10 $\mathrm{m\,s^{-1}}$[24]. It is possible that the temporal-correlation peaks due to moving atmospheric turbulence layers are hidden by the strong peak associated with the additional slow or not moving component. We will discuss this slow wind speeds and the temporal correlation peak without moving in the off-line analysis.

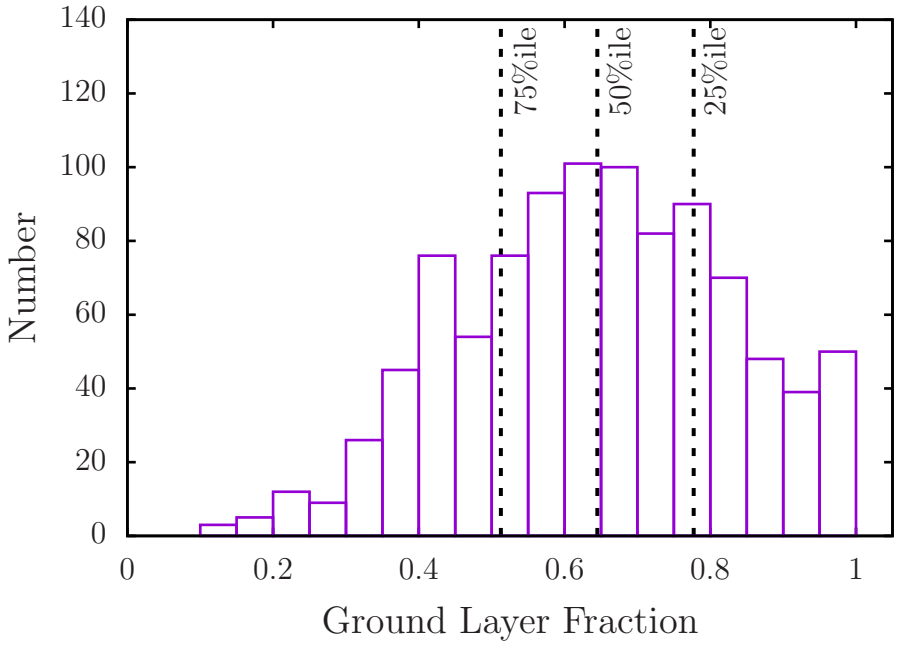

Figure. 6.4: Histogram of ground layer fraction measured by the covariance SLODAR during on-sky observations from June 23th to July 2nd in 2015 (HST).

6.1.4 On-sky Performance of the Multi Time-step Reconstruction

We evaluate the performance of the multi time-step reconstruction with the PSF images taken by IRCS during the on-sky observations. All PSF images which we use are observed by H-band. The exposure time for each image is roughly 30 seconds. The pixel scale of IRCS corresponds to 0.023 arcseconds, which is measured from the image of the binary star taken during the on-sky observations.

We use FWHM, SR, and EE in a 140 mas box for the performance evaluation. These metrics are affected strongly on the background subtraction from the images. Therefore, the same criteria to subtract the background should be used for all images. We define the count of the background at radius of 10 times of its FWHM. When the FWHM is larger than 0.3 arcsecond, the radius of 10 times of its FWHM is out of the FoV because the size of the FoV of each science channel is 4 arcsecond. In this case, we define the back ground count at the radius as large as possible.

Fig. 6.7 shows the FWHM, SR, and EE measured from the on-sky PSF images. These metrics are plotted as a function of a r_0 measured by the covariance SLODAR. The red and blue points indicate the results of the single and multi time-step reconstruction, respectively. For the multi time-step reconstruction, we set Δt to a time duration corresponding to 20 frames. In most case, the frame

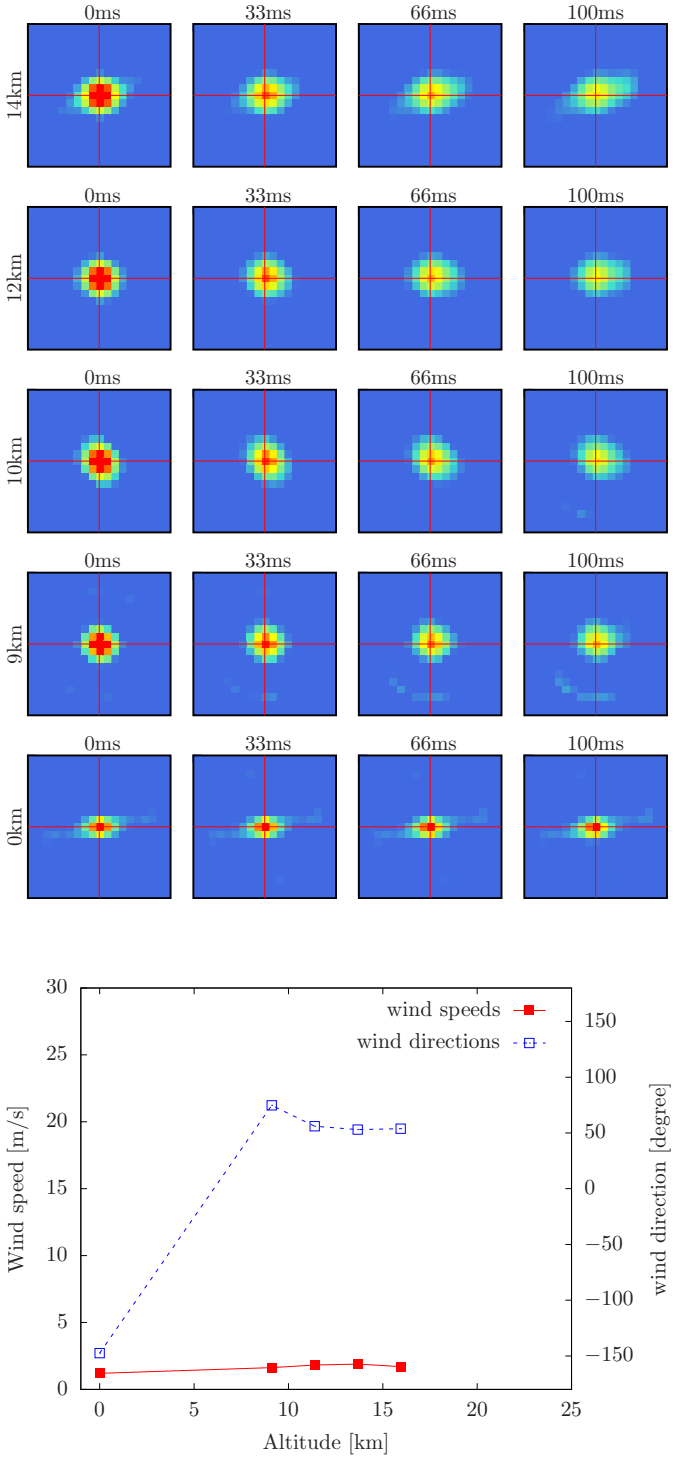

Figure. 6.5: Top: Temporal-correlation maps with different time delays, δt, at each altitudes for the cases of Fig. 6.2. The x and y-axes are δi and δj with a range of $-9 \leq \delta i, \delta j \leq 9$. One pixel on the temporal-correlation corresponds to one subaperture size, which is 0.8 m in the RAVEN. The temporal-correlation maps are normalized by the peak intensity of the map of δt=0 at each altitude. The color scale of the maps is set to [0 0.7]. Bottom: Wind speed (red) and direction profile (blue) as a function of altitude from the telescope. The wind speed follows the left y-axis, and the wind direction follows the right y-axis.

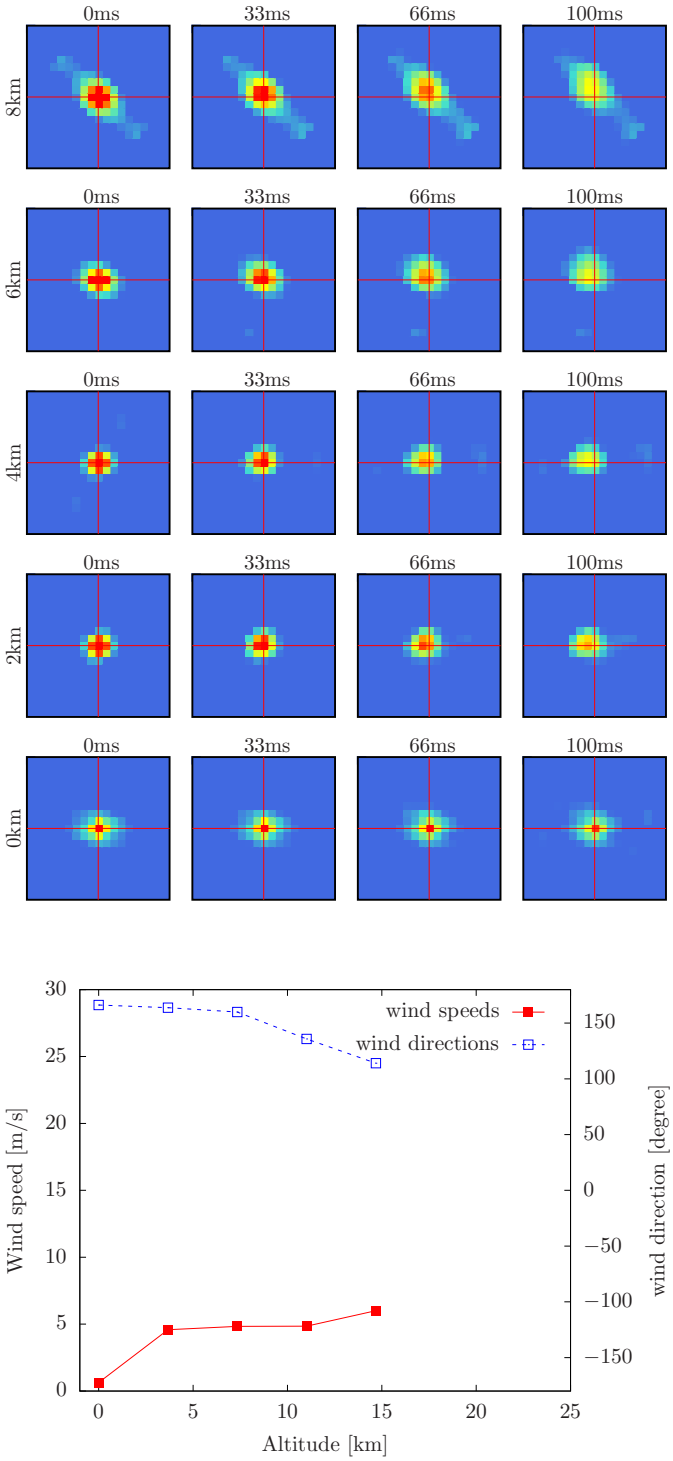

Figure. 6.6: The same figure as Fig. 6.5 with the C_N^2 profile shown in Fig. 6.3.

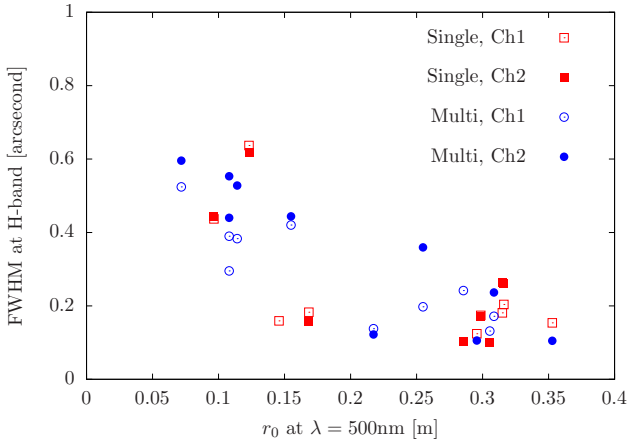

(a) FWHM

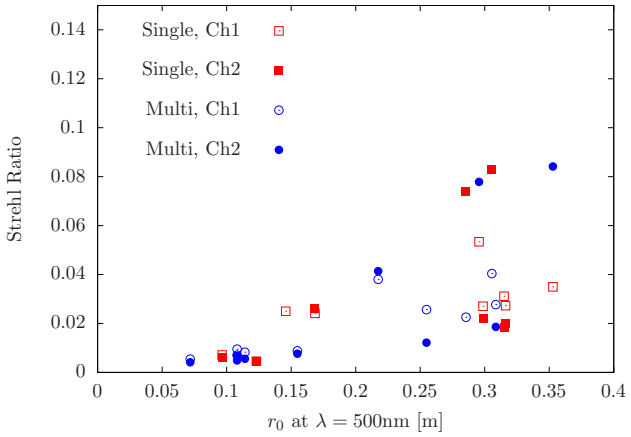

(b) Strehl Ratio

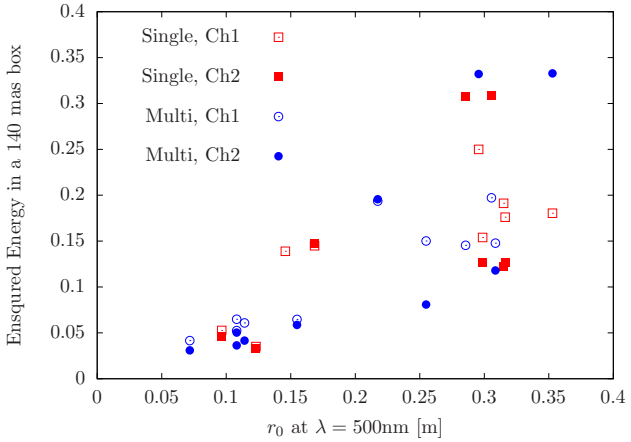

(c) Ensqured Enegy in 140 mas bax

Figure. 6.7: The (a) FWHM, (b) SR, and (c) EE in 140 mas box measured from the PSF images obtained in the on-sky engineering observations. These metrics are plotted as a function of a r_0. The red squres indicate the results of the single time-step reconstructor and the blue circles are the result of the multi time-step reconstructor. The filled and open symbols indeciate the result of the science channel 1 and 2, respectively. In the enginnering observation, we set Δt to a duretion corresponding to 20 frames. In the most case, the framerate of the control for MOAO system is 150 Hz and Δt is 133 ms.

rate of the MOAO control is 150 Hz and therefore Δt is 133 ms. We achieve the FWHM of 0.1 arcseconds and EE more than 0.3 when r_0=0.3 m. On the other hand, there is the large variance of the EEs at the same r_0 =0.3 m. One reason is the variation of the NGS asterisms. Another reason is the effect of the DM instability. The initial command of the DM is set to cancel the phase distortion due to the optical error. This *best flat command* is determined experimentally before the observations and used as the reference command of the DM during the observation. However, we found that the best flat command changes after we use the DM continuously over a long time. Therefore, especially in the latter half of the night, the DMs become unstable and decrease the performance.

In Fig. 6.7, there is no clear improvement due to the multi time-step tomographic reconstruction. The error of the wind estimation may be a main cause which degrades the performance of the multi time-step reconstruction. Fig. 6.8 shows the PSF images observed with the correction by the single and the multi time-step tomographic reconstruction alternately with two minutes intervals. The field is Fd38. Since the PSF images of the science channel 1 are affected by the DM instability, we focus on the result of the science channel 2. The FWHMs of the single time-step tomographic reconstructor are a few mas better than the FWHM of the multi time-step reconstruction, but this difference is much smaller than the pixel scale of 23 mas. It is difficult to conclude that this difference is due to the difference of the reconstructor. The values of SR look to depend on the fried parameter r_0. The EEs in a 140 mas box of the multi time-step tomographic reconstructor is 0.02 larger than that of the single time-step reconstructor. Fig. 6.9 shows the C_N^2 profile the wind speeds and directions used for the reconstruction at this time. The wind speeds at all altitudes are almost 0 m/s, which is affected by the slow or not moving component which we mentioned in the previous subsection. In such a case, the improvement with the multi time-step reconstruction can not be expected. Therefore, the difference in the EEs may not be due to the difference of the reconstructor.

Unfortunately, we can not achieve the clear improvement due to the multi time-step tomographic reconstruction from the on-sky PSF images during engineering observations. In the next section, we improve and evaluate the wind estimation method and the multi time-step tomographic reconstruction with the off-line analysis using the on-sky measurements of SH-WFSs.

r_0 [m]	0.296	0.305	0.353	0.285
Ch1	Single	Multi	Single	Multi
FWHM [mas]	124	132	154	242
SR [%]	0.053	0.040	0.035	0.023
EE [%]	0.250	0.198	0.180	0.145
Ch2	Multi	Single	Multi	Single
FWHM [mas]	106	101	105	103
SR [%]	0.078	0.083	0.084	0.074
EE [%]	0.332	0.309	0.333	0.307

Figure. 6.8: The on-sky PSF images corrected by the single and multi time-step reconstructor. The size of PSF images is 1.5×1.5 arcsecond.

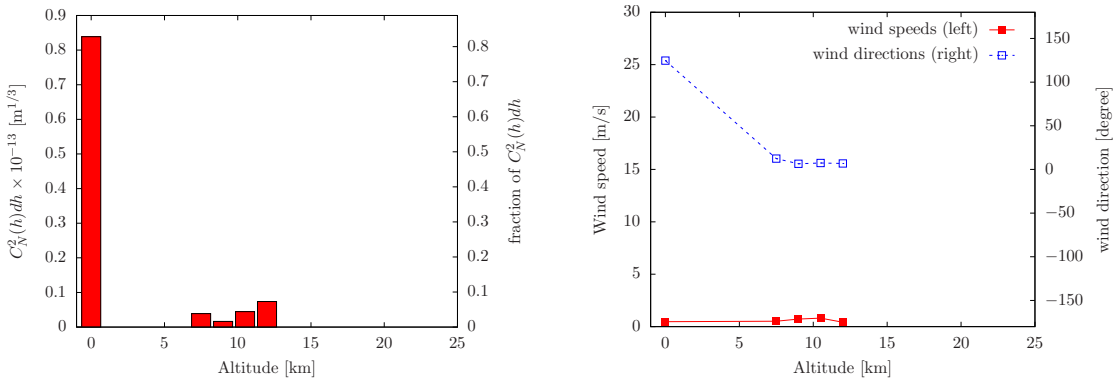

Figure. 6.9: The profiles of C_N^2 values (left panel), wind speeds (right panel), and wind directions (right panel) measured on sky. The field is Fd38 and the asterism is same as Fig. 6.2. In the C_N^2 profile, more than 80 % of the turbulence are concentrated in the ground layer and there are weak turbulences at around 10 km. On the left panel, the detected wind speeds are almost zero at all altitudes.

6.2 Off-Line Analysis

6.2.1 Improvement in the Wind Estimation

First, we improve the wind estimation method. As mentioned in subsection 6.1.3, the wind speeds are seen to be underestimated due to the additional slow or not moving component especially at high altitudes. As explained in Chapter 2, we compute the temporal averaged pattern from the time series of the reconstructed slopes and subtract the computed averaged pattern from the reconstructed slopes to remove static pattern. In the revised wind estimation method, we perform this process for every one second time series of the reconstructed slopes before computing temporal-correlations, and cancel the additional slow or not moving component from the temporal-correlation maps to detect only moving turbulence layers. This process corresponds to remove the component changing slower than 1 Hz or moving slower than $\sim$0.4 $\mathrm{m\,s^{-1}}$from the temporal-correlation maps. For the ground layer, the dome seeing may be removed by this process. Fig. 6.10 and Fig. 6.11 are the revised versions of Fig. 6.5 and Fig. 6.6, respectively. In both of Fig. 6.10 and Fig. 6.11, the only moving peaks are successfully extracted. The measured wind speeds are larger than the value measured during the on-sky observation in real-time, and thus, the underestimation is solved by the revised wind estimation method.

Fig. 6.12 shows example of of the phase distortion pattern averaged over each one second at different altitudes. The averaged pattern at 0 km and 4 km change slowly with time and some distortion patterns remain over several seconds. These long-lived distortion patterns cause the temporal-correlation peak not moving with δt and the underestimation of the wind speeds. Although the averaged distortion pattern at 8 km change more rapidly than that of 0 km and 4 km, sometimes the adjacent distortion maps have marginally same pattern and it is possible that these pattern make the temporal-correlation peak not moving.

At the 0 km, the slowly changing distortion pattern can be explained by the dome seeing, but it is difficult to consider that there are additional components slowly changing at high altitudes, which are different from the moving turbulence layer. In Fig. 6.12, the similar phase distortion patterns are seen on the averaged phase map for all altitudes. These maps are constructed by the tomographic reconstruction. In other words, it is possible that the reconstructed phase distortion or slope is affected by the degeneracy due to the *unoverlapped area*, the uncertainty of the turbulence height and strength measured by the SLODAR, and

the measurement noise. Therefore, these similar patterns, which change slowly as shown in Fig. 6.12, may be caused by the error of the tomographic reconstruction. In the laboratory experiment, since the magnitude of the NGSs are set to around 8 mag, the tomographic reconstruction is performed more accurately compared with the on-sky observations, and thus, the slow or not moving correlation peak is not seen in Fig. 5.5. Furthermore, the turbulence layers generated in the laboratory experiment follows perfectly the frozen flow assumption, and therefore, the temporal-correlation peaks are clearer than the peaks of the on-sky observations.

6.2.2 Atmospheric Turbulence Profile

Here, we summarize the profiles of r_0, $C_N^2(h)$, wind speeds and wind directions in the night on June 23–24th, 2015 measured from the on-sky measurements of the open-loop SH-WFSs with the off-line analysis.

Fig. 6.2.2 shows the r_0 profiles measured by the correlation SLODAR of RAVEN (the blue plots), the auto-correlation fitting of RAVEN (the red plots), and the CFHT DIMM (the gray lines) as comparison. In the later half of the night, the RAVEN results are better than the result form the CFHT. This is may be due to the local difference since the CFHT sit on a different ridge from the Subaru telescope. There is a large difference between the result from the SLODAR and the auto-correlation fitting in 2:30–3:30. In this time, since the NGS asterism is wide, the SLODAR can measure the turbulence up to around 9 km and the SLODAR misses the some turbulence at altitude higher than 9 km. On the other hand, the auto-correlation fitting can measure the total turbulence power including the turbulence missed by the SLODAR. Therefore, there is the large difference between the result from the SLODAR and the auto-correlation fitting in this period.

Fig. 6.14 is the C_N^2 profile. In this day, the atmospheric turbulence is dominated by the ground layer in all the time. Also, there are weak turbulences at around 10 km. The C_N^2 profile of this day looks stable throughout the night.

Fig. 6.15 and Fig. 6.16 are the profile of the wind speeds and directions. The ground layer has the wind of 5 $\mathrm{m\,s^{-1}}$and the higher layers have the wind of 10–15 m $\mathrm{s^{-1}}$. Similar to the C_N^2 profile, the wind speed and condition are stable throughout the night. This stability of the wind speeds and directions is essential for the multi time-step reconstruction.

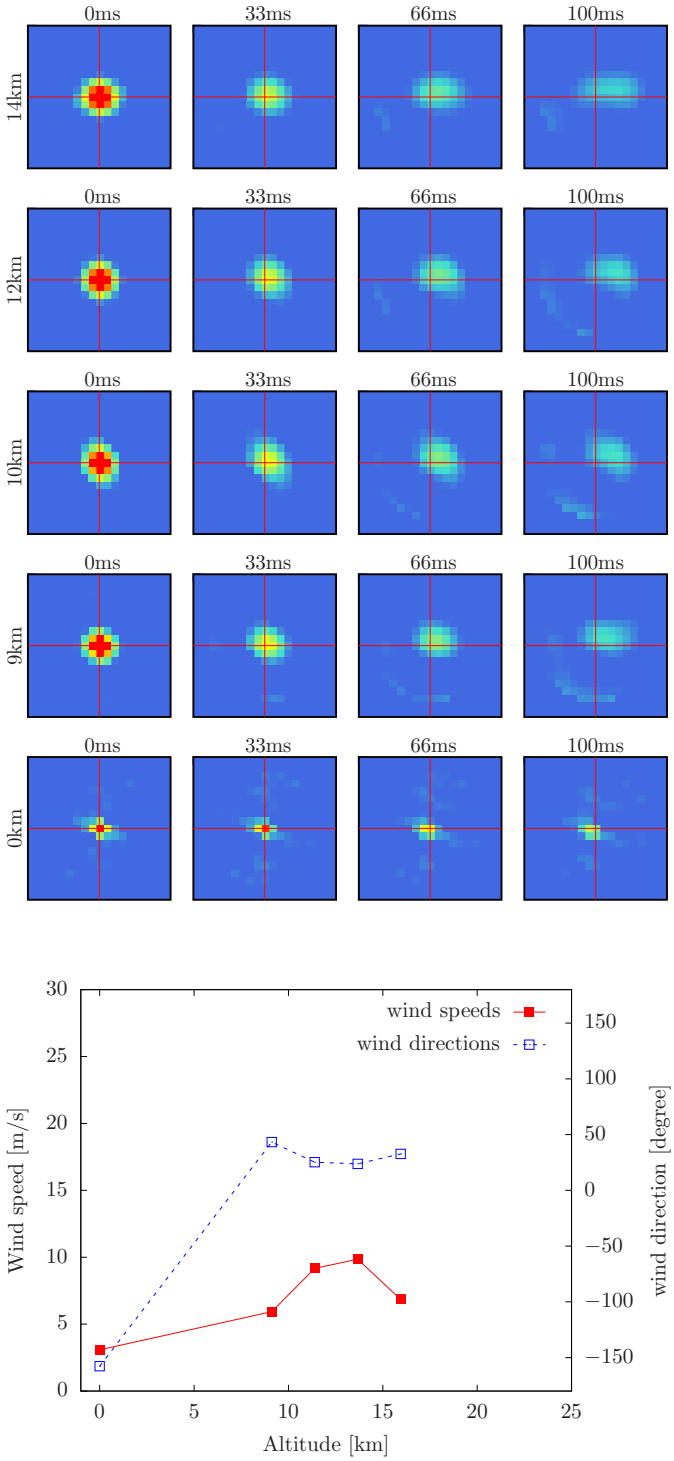

Figure. 6.10: The improved version of Fig. 6.5

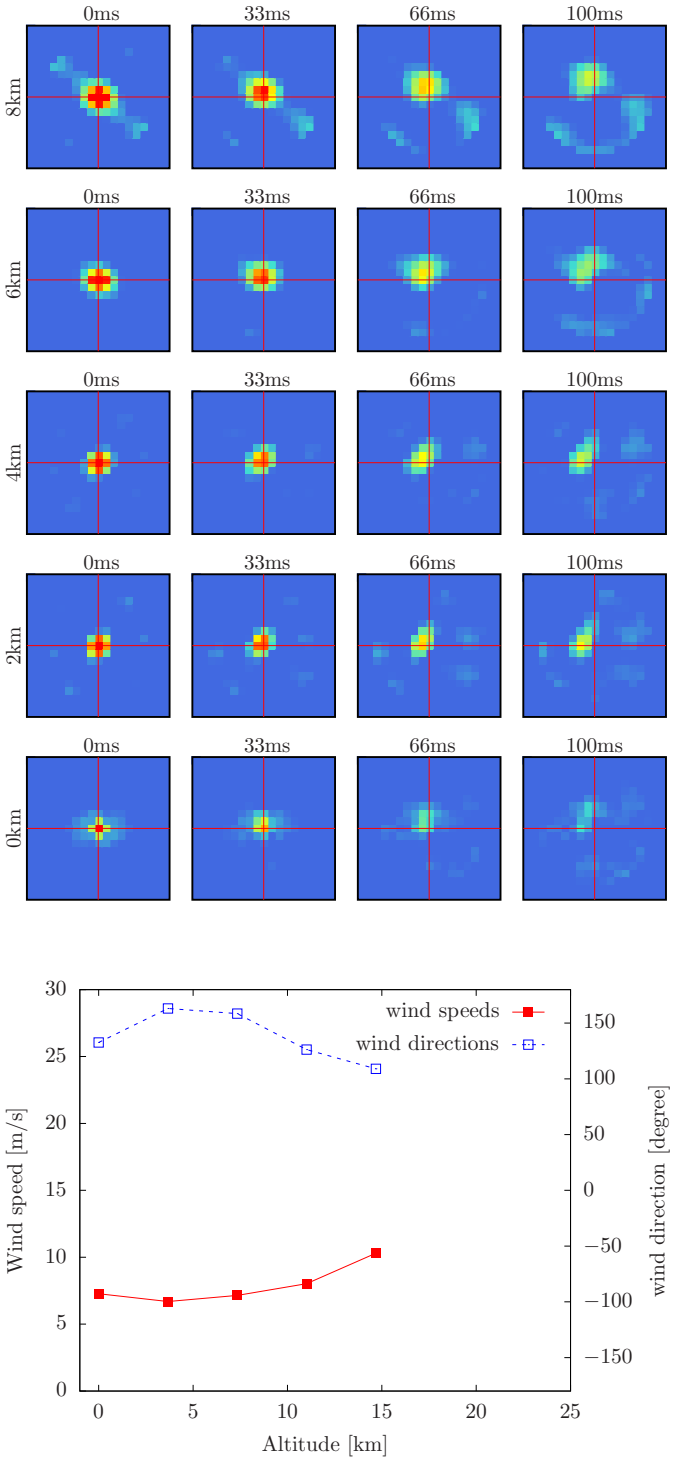

Figure. 6.11: The improved version of Fig. 6.6

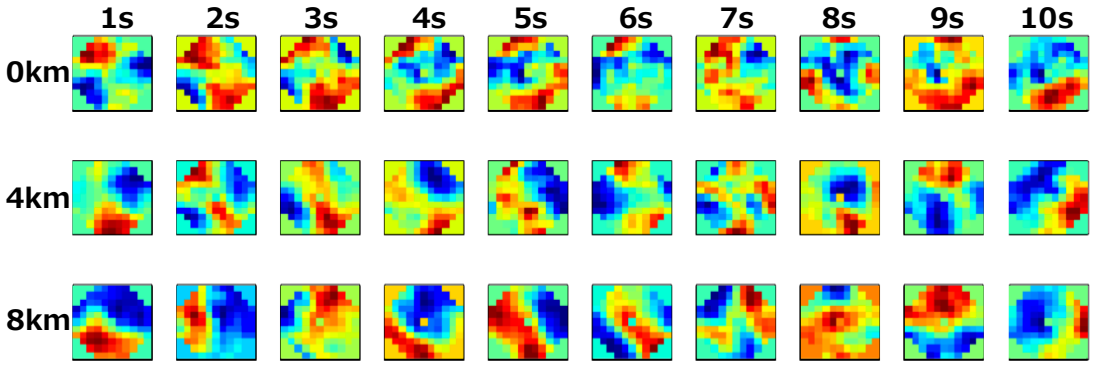

Figure. 6.12: Example of the phase distortion pattern averaged over each one second at different altitudes.

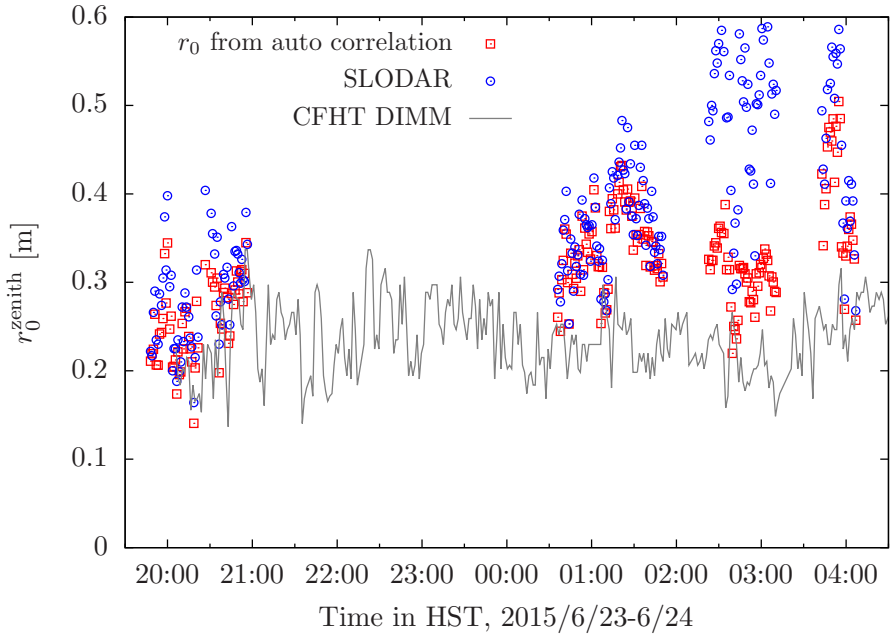

Figure. 6.13: r_0 profiles in the zenith direction on June 23–24th, 2015. The blue plots indicate the r_0 values measure by the correlation SLODAR of RAVEN. The red plots are the r_0 values measured by the auto-correlation fitting of RAVEN. The gray lines are r_0 values measured by the CFHT DIMM (http://mkwc.ifa.hawaii.edu/).

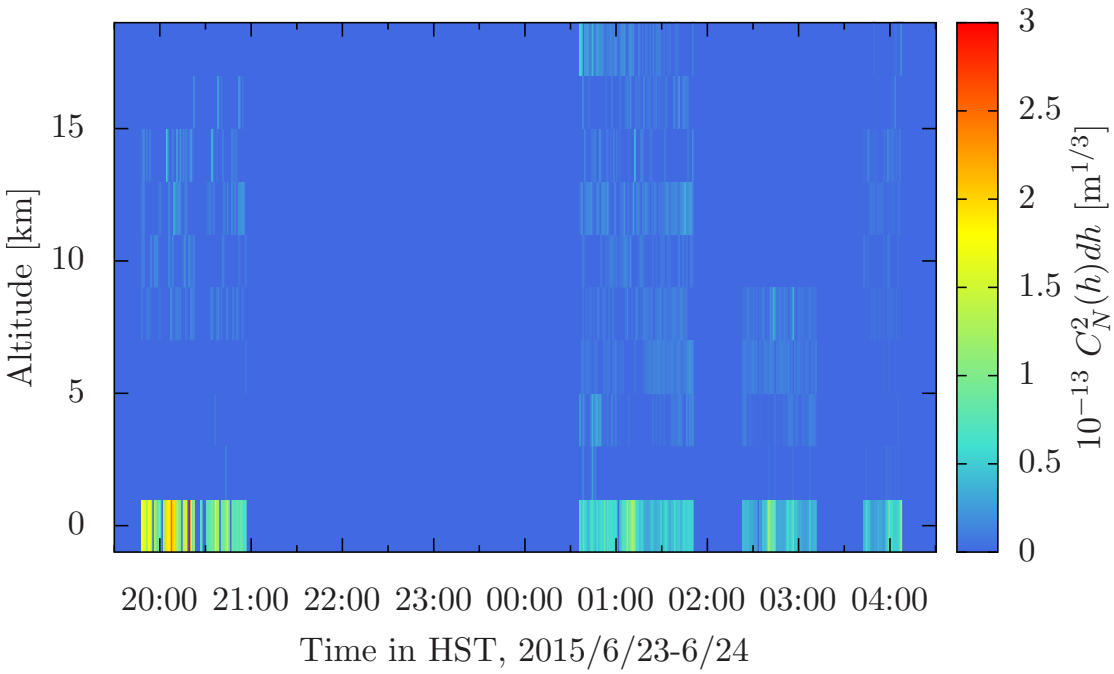

Figure. 6.14: $C_N^2(h)$ profile in the zenith direction on June 23–24th, 2015. The y-axis is altitudes from the telescope.

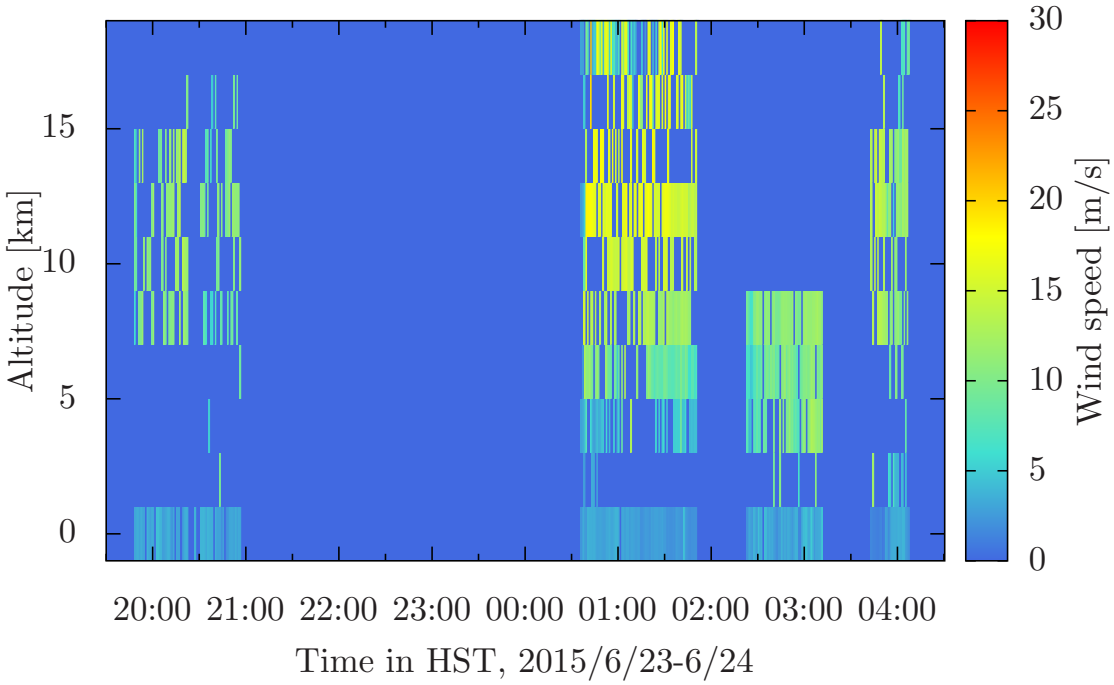

Figure. 6.15: Wind speed profile on June 23–24th, 2015. The y-axis is altitudes from the telescope.

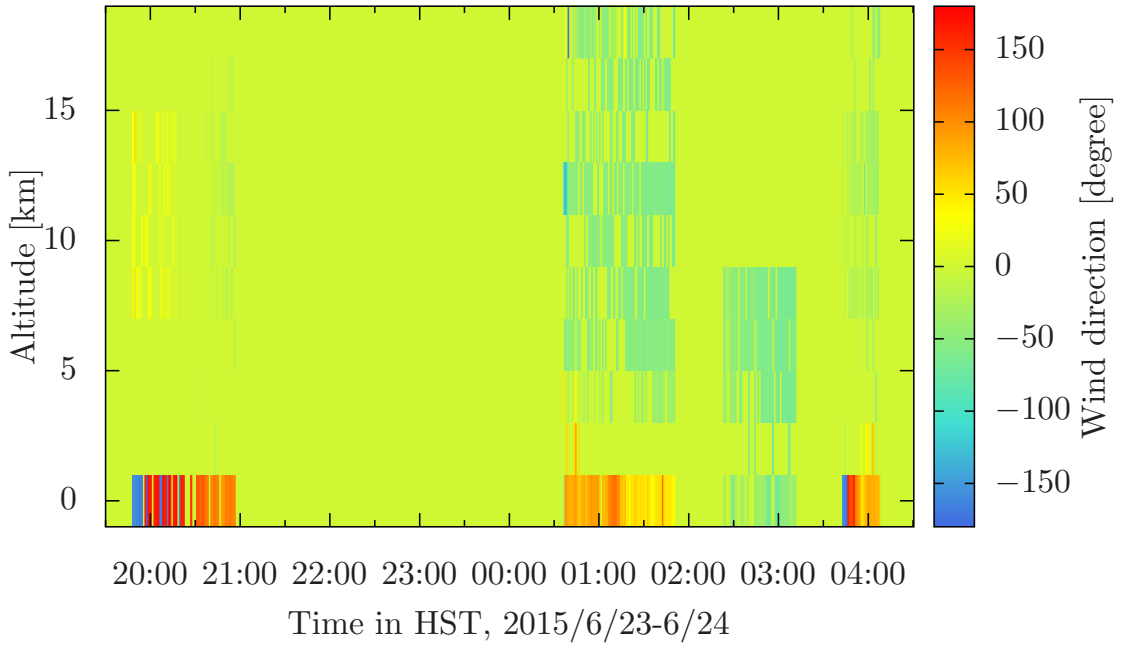

Figure. 6.16: Wind direction profile on June 23–24th, 2015. The y-axis is altitudes from the telescope.

6.2.3 Off-Line Evaluation of Multi Time-Step Reconstruction

Finally, we evaluate the performance of the multi time-step reconstruction with the improved wind estimates. We saved the on-sky measurements both of the OL and the CL-WFSs without an AO correction. The WFE can be computed by comparing the wave-front in the science direction reconstructed from the measurements of the open-loop SH-WFSs with the wave-front computed from the measurements of the closed-loop SH-WFSs.

In this subsection, we show the result of the off-line analysis with two different data set. The first one is shown in Fig. 6.17. Fig. 6.17 shows the asterism, C_N^2 profile, the wind profile, and the tip-tilt removed residual WFEs. The residual WFEs are computed from the on-sky measurement of the SH-WFSs with the single and multi time-step reconstruction. The multi time-step reconstructor is computed with the revised wind speeds and directions and different Δt. The turbulence spreads over the wide range of altitudes. The wind speeds are 1 m s^{-1}at 0 km, and 8 ms^{-1}at 14 km. In this case, the multi time-step reconstructor can decrease the WFE compared with the single time-step reconstructior. The WFE of the multi time-step reconstruction decreases with Δt up to Δt=0.16 s, and this trend is consistent with the results from the analytical model (Fig. 3.4) and numerical simulation (Fig. 4.5). When Δt is larger than 0.16 s, the WFE

starts to increase. This is because the effect of the turbulence boiling affects on the multi time-step reconstructor as $\Delta t > 0.16$ s. The expected decay ratio with $\Delta t = 0.16$ s for the fastest layer (7.16 $\mathrm{m\,s^{-1}}$) is f_{decay}=0.76. In other words, the frozen flow assumption is valid when $f_{\mathrm{decay}} \geq 0.76$. Furthermore, there is a gain with the multi time-step reconstruction in this case, even if $f_{\mathrm{decay}} \sim 0.8$, although the boiling of the turbulence affects the performance of the multi time-step reconstructor. Therefore, our assumption in the previous chapters that the frozen flow holds as $f_{\mathrm{decay}} \geq 0.7$ is valid.

Another case is shown in Fig. 6.18. In this case, the ground layer has a large contribution to the total turbulence power, and it is expected to the gain with the multi time-step reconstruction would be small compared with the first case, because the multi time-step reconstruction is more effective to the uncovered and unoverlapped areas at high altitudes. In Fig. 6.18, the WFE of the multi time-step reconstructor is larger than that of the single time-step reconstructor. This difference becomes larger with larger Δt. The considerable reasons is the error of the wind estimation.

Here, we discuss the effect of dome seeing in the multi time-step reconstructor as another reason making the difference in the performance of the multi time-step reconstruction between the two cases. Guesalaga et al (2014) [21] founds that the dome seeing has a different temporal decay pattern of the cross-correlation peak of the measured slopes from that of the atmospheric ground layer. They measure the fraction of the dome seeing in the ground layer by using this temporal decay. We compute this ground layer temporal decay from the temporal cross-correlation of the measured slopes for the two cases, and investigate the effect of the dome seeing. The intensity of the correlation peak is measured by summing correlations in the central 3×3 pixel on the temporal cross-correlation maps.

Fig. 6.19 shows the decay ratio of the ground layer for the first case. This can be fitted by only one linear line, and it suggests that the temporal decay of the cross-correlation can be describe with moving turbulence. The fitted line becomes 0 at the time delay of 1 s. Therefore, the ground layer is completely de-correlated in 1 s or the peak corresponding to the ground layer goes to out of the central 3×3 box in 1s (i.e, the ground layer moves 1.5 pixel on the correlation map or 1.2 m on the aperture plane). The observed wind speeds at the ground layer, shown in Fig. 6.17, is 1.14 $\mathrm{m\,s^{-1}}$, and the travel distance of the ground layer in 1 s is 1.14 m, which corresponds to ∼1.5 pixel on the correlation map. Thus, the decay ratio is consistent with the observed wind speeds.

On the contrast, the decay ratio of the ground layer consists of two slopes in

the second case. This feature is also observed by GEMS [21]. The steeper slope (blue) represents the temporal decay of the moving turbulence, and the moderate slope (green) represents the temporal decay of the dome seeing. If the dome seeing decays linearly as the time delay is smaller than 0.8 s, the initial fraction of the dome seeing in the ground layer is 64 %. In the multi time-step reconstructor, these two components moving differently at the same altitude can not be modeled and, as a result, it causes the tomographic error. The increase in the WFE with the multi time-step reconstructor in the second case shown in Fig. 6.18 is possibly affected by the dome seeing.

Such a dome seeing effect will affects not only the multi time-step reconstructor, but also predictive controllers [10, 20]. In order to avoid the effect of the dome seeing, it is required to monitor the fraction of the dome seeing, for example by checking the temporal decay of the ground layer, and use the multi time-step reconstruction in the case without the dome seeing.

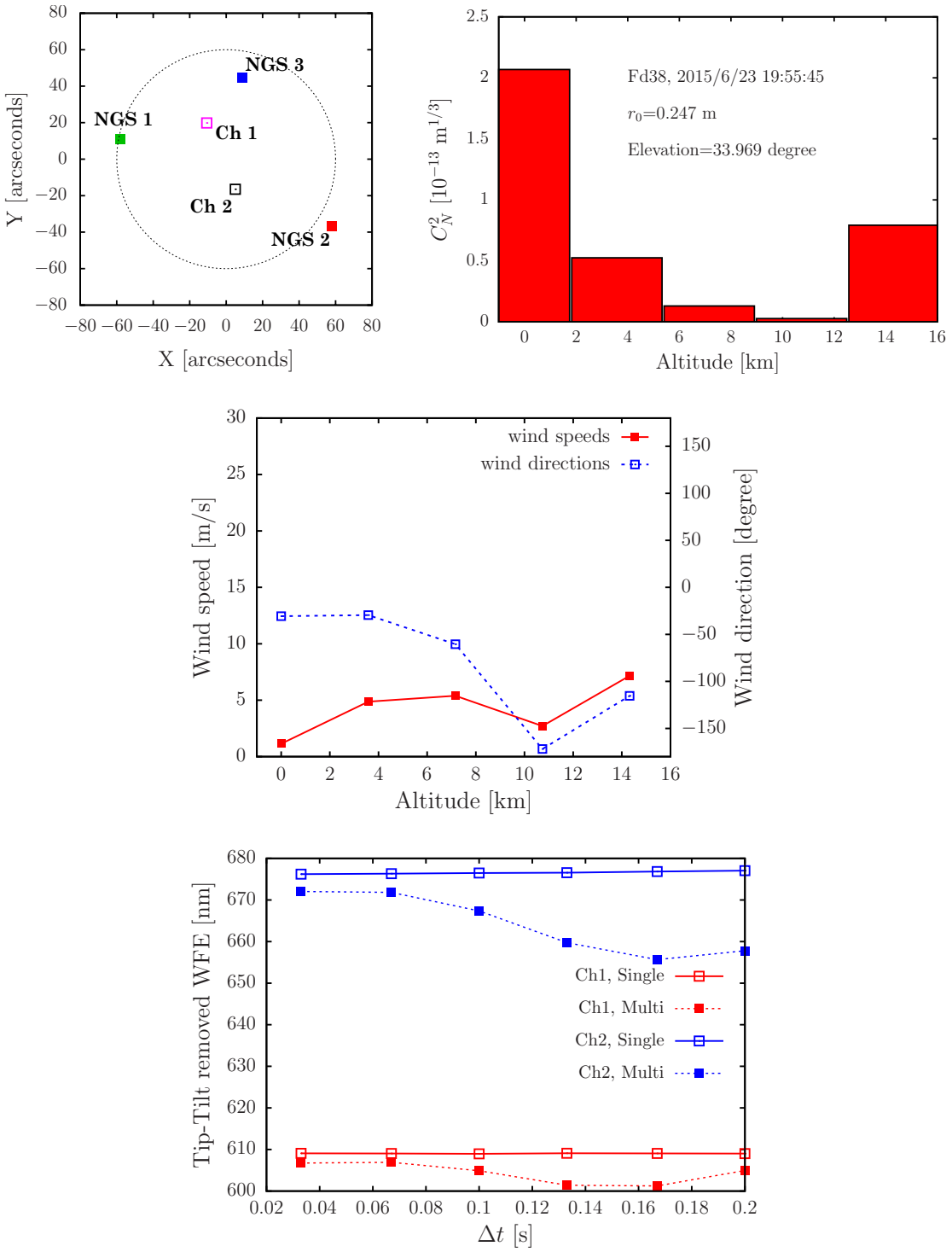

Figure. 6.17: Asterism (top left), C_N^2 profile (top right), the wind profile (middle), and the tip-tilt removed residual WFE (bottom). The residual WFEs are computed from the on-sky measurement of the SH-WFSs with the single and multi time-step reconstruction. The multi time-step reconstructor is computed with the revised wind speeds and directions and different time delay.

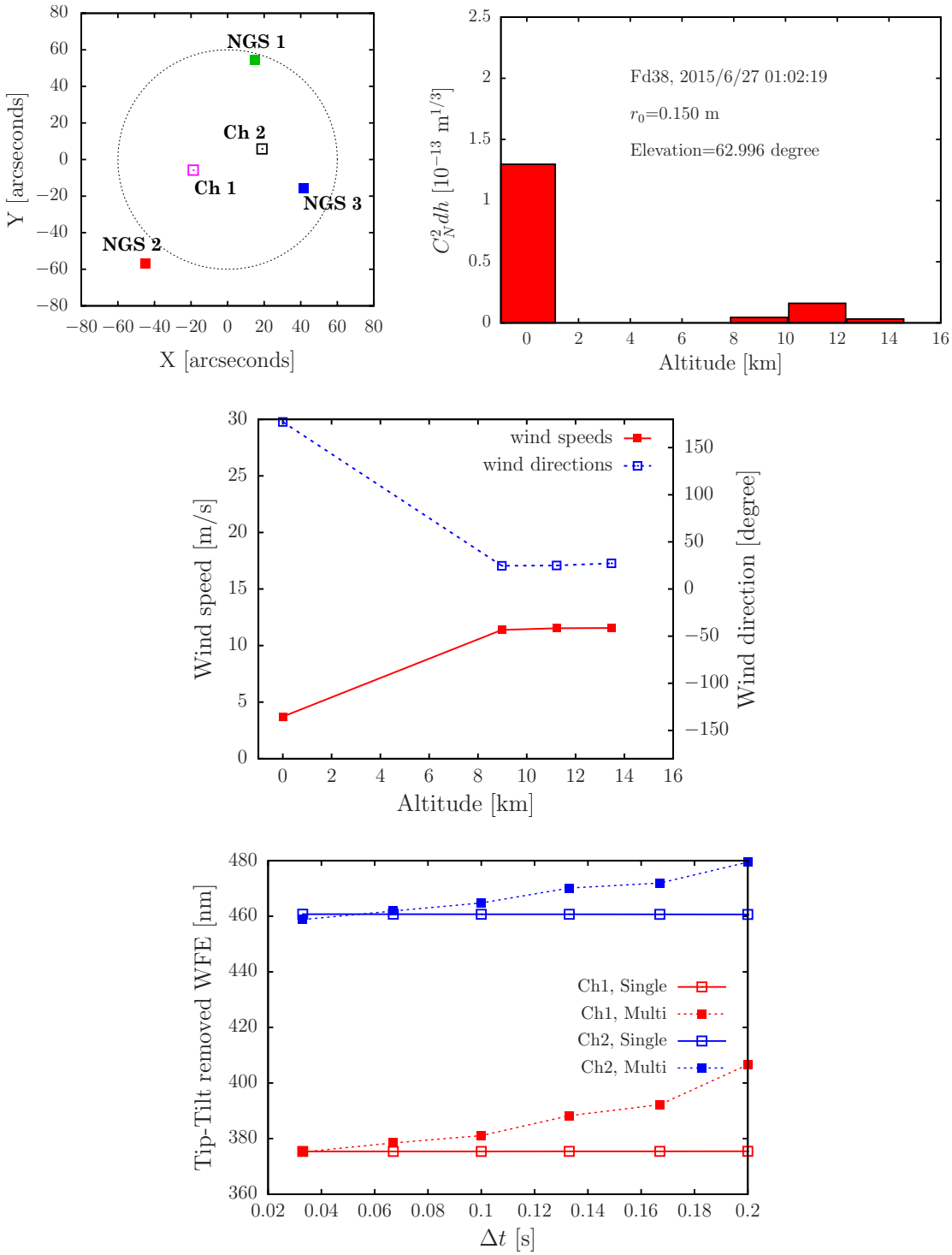

Figure. 6.18: The same figure as the Fig. 6.17 with a different case.

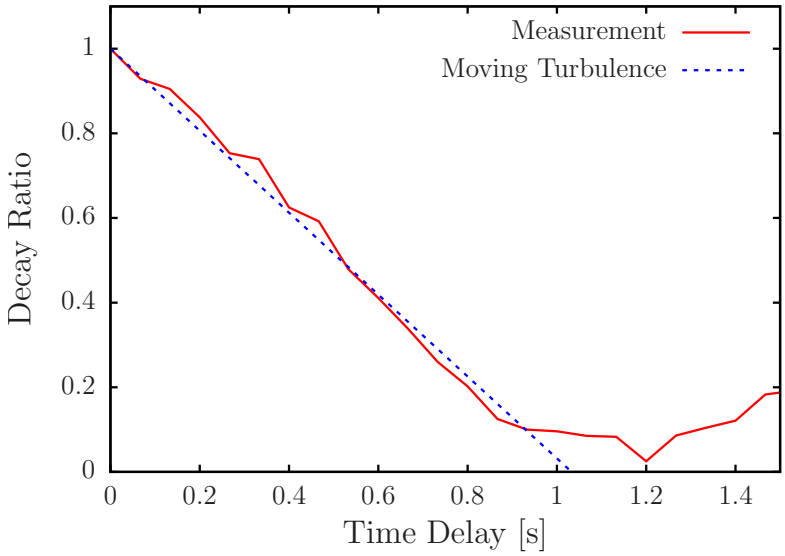

Figure. 6.19: Decay ratio for the ground layer in the first case shown in Fig. 6.17. The red and blue lines indicate the computed decay ratio and a linear line for the moving component determined by the least squares method, respectively.

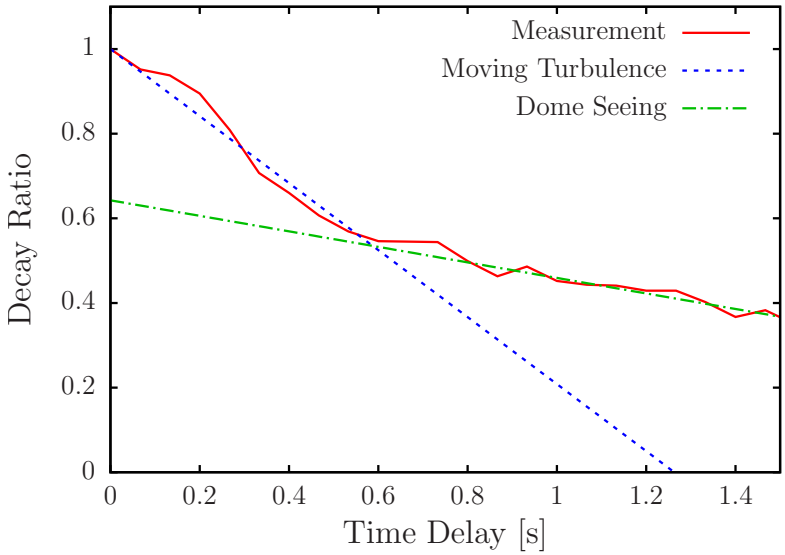

Figure. 6.20: Decay ratio for the ground layer in the first case shown in Fig. 6.18. The red, blue and green lines indicate the computed decay ratio, a linear line for the moving turbulence, and a linear line for the dome seeing, respectively. The linear lines are computed by the least squares method with the time delay range of [0 0.6] second for the moving turbulence and [0.8 1.5] second for the dome seeing.

Chapter 7

Conclusion

In this thesis, we develop and evaluate a new tomographic reconstruction method for the wide-field adaptive optics (WFAO), called *multi time-step reconstruction*, to solve the lack of information in the tomographic reconstruction and expand the size of the FoR of WFAO systems. Also, we evaluate a method to estimate wind speeds and directions at multiple altitudes from the measurements of multiple wave-front sensors. This wind estimation method is required to implement the multi time-step reconstruction. The basic idea of the multi time-step reconstruction is increasing the information by using the measurements at both of the current and previous time-steps with using wind speeds and directions and the frozen flow assumption.

First, we demonstrate the influence of the lack of information in the tomographic reconstruction. Then, we present that our tomographic reconstruction method is effective to reduce the tomographic error due to the lack of information. In the case of 3 NGSs and a telescope of 30 m circular aperture, the multi time-step reconstruction can expand the FoR size from 80 arcseconds diameter to 200 arcseconds diameter without increasing the tomographic error under the assumption that the turbulence follows the frozen flow assumption and we fully know the wind speeds and directions.

Second, we show the result of the numerical simulation of the tomographic reconstruction on a MOAO system on the future ELT. The numerical simulation shows that the multi time-step reconstruction increases Strehl ratio (SR) over a field of regard of 10 arcminutes diameter by a factor of 1.5–1.8 if we fully know the wind speeds and directions and the turbulence follows the frozen flow assumption.

Third, we present the laboratory of the multi time-step reconstruction method and the wind estimation method by using RAVEN, which is a MOAO demonstrator. We can successfully measure the wind speeds and directions in the laboratory experiment. Also, the multi time-step reconstructor can increase an EE in a 140

mas box by 0.03–0.05. However, absolute value of SR and EE is smaller than the value expected by the numerical simulation. Some part of the discrepancy can be explained by the implementation error and the residual tip-tilt errors. In order to understand what limits the performance of RAVEN, more experiments are required.

Finally, we present the on-sky performance of the multi time-step reconstruction and the wind estimation with RAVEN n the Subaru telescope. Unfortunately, there is no clear improvement with the multi time-step reconstruction because of the error of the wind estimation. With the off-line analysis using the on-sky measurement of the wave-front sensors, we improve the wind estimation method and re-evaluate the multi time-step reconstruction. We conclude that the multi time-step reconstruction can reduce the WFE compared with the single time-step reconstructor if $f_{\mathrm{decay}} > 0.7$ %. Also, we conclude that if there are both of the moving turbulence and the dome seeing, the multi time-step reconstructor does not work.

Appendix A

Mathematics

A.1 Minimum Variance Reconstructor and Analytical Tomographic Error

We drive the tomographic wave-front reconstructor Eq. (2.7). Substituting Eq. (2.5), $\boldsymbol{u}_{\boldsymbol{\beta_k}} = \boldsymbol{E}_{\boldsymbol{\beta_k}}\boldsymbol{s}_{\boldsymbol{\alpha}}$, and Eq. (2.10)into Eq. (2.6)

$$\begin{aligned}
\epsilon_{\beta_k} &= \langle ||\boldsymbol{\varphi}_{\boldsymbol{\beta_k}} - \hat{\boldsymbol{\varphi}}_{\boldsymbol{\beta_k}}||^2 \rangle \\
&= \langle ||\boldsymbol{P}_{\boldsymbol{\beta_k}}\boldsymbol{\phi} - \boldsymbol{N}_{\boldsymbol{\beta_k}}\hat{\boldsymbol{u}}_{\boldsymbol{\beta_k}}(t)||^2 \rangle \\
&= \langle ||\boldsymbol{P}_{\boldsymbol{\beta_k}}\boldsymbol{\phi} - \boldsymbol{N}_{\boldsymbol{\beta_k}}\boldsymbol{E}_{\boldsymbol{\beta_k}}\boldsymbol{s}_{\boldsymbol{\alpha}}||^2 \rangle \\
&= \langle ||\boldsymbol{P}_{\boldsymbol{\beta_k}}\boldsymbol{\phi} - \boldsymbol{N}_{\boldsymbol{\beta_k}}\boldsymbol{E}_{\boldsymbol{\beta_k}}(\boldsymbol{\Gamma}_{\boldsymbol{\alpha}}\boldsymbol{P}_{\boldsymbol{\alpha}}\boldsymbol{\phi} + \boldsymbol{\eta})||^2 \rangle \\
&= \langle ||(\boldsymbol{P}_{\boldsymbol{\beta_k}} - \boldsymbol{N}_{\boldsymbol{\beta_k}}\boldsymbol{E}_{\boldsymbol{\beta_k}}\boldsymbol{\Gamma}_{\boldsymbol{\alpha}}\boldsymbol{P}_{\boldsymbol{\alpha}})\boldsymbol{\phi} + \boldsymbol{N}_{\boldsymbol{\beta_k}}\boldsymbol{E}_{\boldsymbol{\beta_k}}\boldsymbol{\eta}||^2 \rangle
\end{aligned} \tag{A.1}$$

A variance of a column vector $\boldsymbol{x}$ is expressed as $||\boldsymbol{x}||^2 = \mathbf{Tr}[\boldsymbol{x}\boldsymbol{x}^T]$, where $\mathbf{Tr}(\boldsymbol{X})$ indicates the trace of a matrix $\boldsymbol{X}$. By using this expression and putting $\boldsymbol{A} = (\boldsymbol{P}_{\boldsymbol{\beta_k}} - \boldsymbol{N}_{\boldsymbol{\beta_k}}\boldsymbol{E}_{\boldsymbol{\beta_k}}\boldsymbol{\Gamma}_{\boldsymbol{\alpha}}\boldsymbol{P}_{\boldsymbol{\alpha}})$ and $\boldsymbol{B} = \boldsymbol{N}_{\boldsymbol{\beta_k}}\boldsymbol{E}_{\boldsymbol{\beta_k}}$, Eq. (A.1) can be transformed into

$$\begin{aligned}
\epsilon_{\beta_k} &= \mathbf{Tr}\left[\langle (\boldsymbol{A}\boldsymbol{\phi} - \boldsymbol{B}\boldsymbol{\eta})(\boldsymbol{A}\boldsymbol{\phi} - \boldsymbol{B}\boldsymbol{\eta})^T \rangle\right] \\
&= \mathbf{Tr}\left[\boldsymbol{A}\langle\boldsymbol{\phi}\boldsymbol{\phi}\rangle\boldsymbol{A}^T\right] + \mathbf{Tr}\left[\boldsymbol{B}\langle\boldsymbol{\eta}\boldsymbol{\eta}\rangle\boldsymbol{B}^T\right] \\
&= \mathbf{Tr}\left[\boldsymbol{A}\boldsymbol{\Sigma}_{\boldsymbol{\phi}\boldsymbol{\phi}}\boldsymbol{A}^T\right] + \mathbf{Tr}\left[\boldsymbol{B}\boldsymbol{\Sigma}_{\boldsymbol{\eta}\boldsymbol{\eta}}\boldsymbol{B}^T\right],
\end{aligned} \tag{A.2}$$

where $\langle\boldsymbol{\phi}\boldsymbol{\phi}\rangle = \boldsymbol{\Sigma}_{\boldsymbol{\phi}\boldsymbol{\phi}}$ and $\langle\boldsymbol{\eta}\boldsymbol{\eta}\rangle = \boldsymbol{\Sigma}_{\boldsymbol{\eta}\boldsymbol{\eta}}$ are covariance matrix for the phase distortion due to the atmospheric turbulence and a covariance matrix of the measurement noise, respectively. We assume that the phase distortion is independent from the measurement noise , this is, $\langle\boldsymbol{\phi}\boldsymbol{\eta}\rangle = \langle\boldsymbol{\eta}\boldsymbol{\phi}\rangle = \mathbf{0}$. We can compute the residual WFE due to the tomographic error from Eq. (A.2) analytically by matrix calculation.

The reconstructor $\boldsymbol{E}_{\boldsymbol{\beta_k}}$ for $\boldsymbol{\beta_k}$ direction is derived by minimizing ϵ_{β_k}. This is

equal to computing $\boldsymbol{E}_{\boldsymbol{\beta_k}}$, which meets $\partial\epsilon_{\beta_k}/\partial\boldsymbol{E}_{\boldsymbol{\beta_k}} = \mathbf{0}$. The partial differential of the first term is computed as

$$\begin{aligned}\frac{\partial(\boldsymbol{A}\boldsymbol{\Sigma}_{\boldsymbol{\phi\phi}}\boldsymbol{A}^T)}{\partial\boldsymbol{E}_{\boldsymbol{\beta_k}}} =& -\frac{\partial}{\partial\boldsymbol{E}_{\boldsymbol{\beta_k}}}\boldsymbol{P}_{\boldsymbol{\beta_k}}\boldsymbol{\Sigma}_{\boldsymbol{\phi\phi}}\boldsymbol{P}_{\boldsymbol{\alpha}}^T\boldsymbol{\Gamma}_{\boldsymbol{\alpha}}^T\boldsymbol{E}_{\boldsymbol{\beta_k}}^T\boldsymbol{N}_{\boldsymbol{\beta_k}}^T \\ &-\frac{\partial}{\partial\boldsymbol{E}_{\boldsymbol{\beta_k}}}\boldsymbol{N}_{\boldsymbol{\beta_k}}\boldsymbol{E}_{\boldsymbol{\beta_k}}\boldsymbol{\Gamma}_{\boldsymbol{\alpha}}\boldsymbol{P}_{\boldsymbol{\alpha}}\boldsymbol{\Sigma}_{\boldsymbol{\phi\phi}}\boldsymbol{P}_{\boldsymbol{\beta_k}}^T \\ &+\frac{\partial}{\partial\boldsymbol{E}_{\boldsymbol{\beta_k}}}\boldsymbol{N}_{\boldsymbol{\beta_k}}\boldsymbol{E}_{\boldsymbol{\beta_k}}\boldsymbol{\Gamma}_{\boldsymbol{\alpha}}\boldsymbol{P}_{\boldsymbol{\alpha}}\boldsymbol{\Sigma}_{\boldsymbol{\phi\phi}}\boldsymbol{P}_{\boldsymbol{\alpha}}^T\boldsymbol{\Gamma}_{\boldsymbol{\alpha}}^T\boldsymbol{E}_{\boldsymbol{\beta_k}}^T\boldsymbol{N}_{\boldsymbol{\beta_k}}^T \\ =& -2\boldsymbol{N}_{\boldsymbol{\beta_k}}^T\boldsymbol{P}_{\boldsymbol{\beta_k}}\boldsymbol{\Sigma}_{\boldsymbol{\phi\phi}}\boldsymbol{P}_{\boldsymbol{\alpha}}^T\boldsymbol{\Gamma}_{\boldsymbol{\alpha}}^T + 2\boldsymbol{N}_{\boldsymbol{\beta_k}}^T\boldsymbol{N}_{\boldsymbol{\beta_k}}\boldsymbol{E}_{\boldsymbol{\beta_k}}\boldsymbol{\Gamma}_{\boldsymbol{\alpha}}\boldsymbol{P}_{\boldsymbol{\alpha}}\boldsymbol{\Sigma}_{\boldsymbol{\phi\phi}}\boldsymbol{P}_{\boldsymbol{\alpha}}^T\boldsymbol{\Gamma}_{\boldsymbol{\alpha}}^T \\ =& 2\boldsymbol{N}_{\boldsymbol{\beta_k}}^T(\boldsymbol{N}_{\boldsymbol{\beta_k}}\boldsymbol{E}_{\boldsymbol{\beta_k}}\boldsymbol{\Gamma}_{\boldsymbol{\alpha}}\boldsymbol{P}_{\boldsymbol{\alpha}}\boldsymbol{\Sigma}_{\boldsymbol{\phi\phi}}\boldsymbol{P}_{\boldsymbol{\alpha}}^T\boldsymbol{\Gamma}_{\boldsymbol{\alpha}}^T - \boldsymbol{P}_{\boldsymbol{\beta_k}}\boldsymbol{\Sigma}_{\boldsymbol{\phi\phi}}\boldsymbol{P}_{\boldsymbol{\alpha}}^T\boldsymbol{\Gamma}_{\boldsymbol{\alpha}}^T). \end{aligned} \tag{A.3}$$

The partial differential of the second term is computed as

$$\begin{aligned}\frac{\partial(\boldsymbol{B}\boldsymbol{\Sigma}_{\boldsymbol{\eta\eta}}\boldsymbol{B}^T)}{\partial\boldsymbol{E}_{\boldsymbol{\beta_k}}} =& \frac{\partial}{\partial\boldsymbol{E}_{\boldsymbol{\beta_k}}}\boldsymbol{N}_{\boldsymbol{\beta_k}}\boldsymbol{E}_{\boldsymbol{\beta_k}}\boldsymbol{\Sigma}_{\boldsymbol{\eta\eta}}\boldsymbol{E}_{\boldsymbol{\beta_k}}^T \\ =& 2\boldsymbol{N}_{\boldsymbol{\beta_k}}^T\boldsymbol{N}_{\boldsymbol{\beta_k}}\boldsymbol{E}_{\boldsymbol{\beta_k}}\boldsymbol{\Sigma}_{\boldsymbol{\eta\eta}}. \end{aligned} \tag{A.4}$$

Then, combining Eq. (A.3) and Eq. (A.4) leads to

$$\frac{\partial\epsilon_{\beta_k}}{\partial\boldsymbol{E}_{\boldsymbol{\beta_k}}} = 2\boldsymbol{N}_{\boldsymbol{\beta_k}}^T\left[\boldsymbol{N}_{\boldsymbol{\beta_k}}\boldsymbol{E}_{\boldsymbol{\beta_k}}(\boldsymbol{\Gamma}_{\boldsymbol{\alpha}}\boldsymbol{P}_{\boldsymbol{\alpha}}\boldsymbol{\Sigma}_{\boldsymbol{\phi\phi}}\boldsymbol{P}_{\boldsymbol{\alpha}}^T\boldsymbol{\Gamma}_{\boldsymbol{\alpha}}^T - \boldsymbol{\Sigma}_{\boldsymbol{\eta\eta}}) - \boldsymbol{P}_{\boldsymbol{\beta_k}}\boldsymbol{\Sigma}_{\boldsymbol{\phi\phi}}\boldsymbol{P}_{\boldsymbol{\alpha}}^T\boldsymbol{\Gamma}_{\boldsymbol{\alpha}}^T\right]. \tag{A.5}$$

The reconstructor meeting $\partial\epsilon_{\beta_k}/\partial\boldsymbol{E}_{\boldsymbol{\beta_k}} = \mathbf{0}$ is given as

$$\boldsymbol{E}_{\boldsymbol{\beta_k}} = (\boldsymbol{N}_{\boldsymbol{\beta_k}}^T\boldsymbol{N}_{\boldsymbol{\beta_k}})^{-1}\boldsymbol{N}_{\boldsymbol{\beta_k}}^T\boldsymbol{P}_{\boldsymbol{\beta_k}}\boldsymbol{\Sigma}_{\boldsymbol{\phi\phi}}\boldsymbol{P}_{\boldsymbol{\alpha}}^T\boldsymbol{\Gamma}_{\boldsymbol{\alpha}}^T(\boldsymbol{\Gamma}_{\boldsymbol{\alpha}}\boldsymbol{P}_{\boldsymbol{\alpha}}\boldsymbol{\Sigma}_{\boldsymbol{\phi\phi}}\boldsymbol{P}_{\boldsymbol{\alpha}}^T\boldsymbol{\Gamma}_{\boldsymbol{\alpha}}^T - \boldsymbol{\Sigma}_{\boldsymbol{\eta\eta}})^{-1} \tag{A.6}$$

$$= \boldsymbol{F}_{\boldsymbol{\beta_k}}\boldsymbol{E}_{\boldsymbol{\phi}}. \tag{A.7}$$

This is the minimum variance reconstructor for MOAO, which compute the DM commands to compensate the phase distortion in $\boldsymbol{\beta_k}$ direction. The first matrix $\boldsymbol{F}_{\boldsymbol{\beta_k}}$ is a *fitting matrix* of a DM for $\boldsymbol{\beta_k}$ direction, and the second matrix $\boldsymbol{E}_{\boldsymbol{\phi}}$ is a *estimation matrix* to reconstructs the phase distortion of the atmospheric turbulence layers. The estimation matrix can be transformed as

$$\boldsymbol{E}_{\boldsymbol{\phi}} = (\boldsymbol{P}_{\boldsymbol{\alpha}}^T\boldsymbol{\Gamma}_{\boldsymbol{\alpha}}^T\boldsymbol{\Sigma}_{\boldsymbol{\eta\eta}}^{-1}\boldsymbol{\Gamma}_{\boldsymbol{\alpha}}\boldsymbol{P}_{\boldsymbol{\alpha}} - \boldsymbol{\Sigma}_{\boldsymbol{\phi\phi}}^{-1})^{-1}\boldsymbol{P}_{\boldsymbol{\alpha}}^T\boldsymbol{\Gamma}_{\boldsymbol{\alpha}}^T\boldsymbol{\Sigma}_{\boldsymbol{\eta\eta}}^{-1}. \tag{A.8}$$

A.2 The Scaling of Discrete Laplacian Matrix

In this section, we drive the scaling of discrete laplacian introduced in 2.1.3 based on [20]. The phase covariance matrix of the turbulence layer indexed by i, $\boldsymbol{\Sigma}_{\boldsymbol{\phi\phi},\boldsymbol{i}}$,

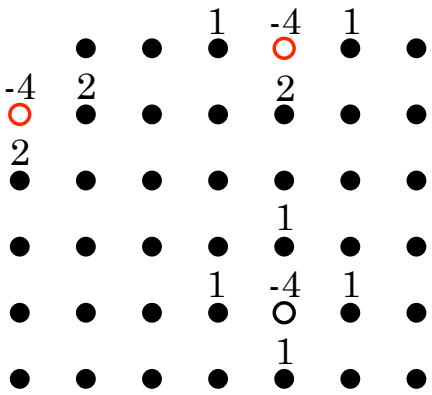

Figure. A.1: The

is approximated by using the discrete laplacian $\boldsymbol{L_i}$ as Eq. (2.14). In the approximation, each row of the discrete laplacian indicates the local curvature of each phase point on the turbulence layers, which is defined by surrounding four phase points as the following *stencil*.

$$\text{stencil}(\bar{\boldsymbol{L}}_{\boldsymbol{i}}) = \begin{bmatrix} 0 & \omega_1 & 0 \\ \omega_2 & \omega_3 & \omega_4 \\ 0 & \omega_5 & 0 \end{bmatrix}. \tag{A.9}$$

For the phase points which is not on the boundary, the weights are $\omega_3 = -4$ and $\omega_1 = \omega_2 = \omega_4 = \omega_5 = 1$. These weights are different for the boundary phase points as shown in Fig. A.1.

The scaling constant c_i for the discrete Laplacian is determined to satisfy $\langle \boldsymbol{\phi_i}^T \boldsymbol{\Sigma}_{\boldsymbol{\phi\phi},\boldsymbol{i}} \boldsymbol{\phi_i} \rangle = \langle \boldsymbol{\phi_i}^T \boldsymbol{L_i}^T \boldsymbol{L_i} \boldsymbol{\phi_i} \rangle = c_i^2 \langle \boldsymbol{\phi_i}^T \bar{\boldsymbol{L}}_{\boldsymbol{i}}^T \bar{\boldsymbol{L}}_{\boldsymbol{i}} \boldsymbol{\phi_i} \rangle$, where $\boldsymbol{\phi_i}$ is a phase distortion vector for ith turbulence layer. If the number of phase points on ith turbulence layer is denoted by n^i_{layer}, the right term can be computed as $\langle \boldsymbol{\phi_i}^T \boldsymbol{\Sigma}_{\boldsymbol{\phi\phi},\boldsymbol{i}} \boldsymbol{\phi_i} \rangle = n^i_{\text{layer}}$. Therefore, the scale constant is given by

$$c_i^2 = \frac{n^i_{\text{layer}}}{\langle \boldsymbol{\phi_i}^T \bar{\boldsymbol{L}}_{\boldsymbol{i}}^T \bar{\boldsymbol{L}}_{\boldsymbol{i}} \boldsymbol{\phi_i} \rangle}. \tag{A.10}$$

Denoting kth row vector of $\bar{\boldsymbol{L}}_{\boldsymbol{i}}$ by $\{\bar{\boldsymbol{l}}_{\boldsymbol{i}}\}_k$, we have

$$\langle \boldsymbol{\phi_i}^T \bar{\boldsymbol{L}}_{\boldsymbol{i}}^T \bar{\boldsymbol{L}}_{\boldsymbol{i}} \boldsymbol{\phi_i} \rangle = \sum_{k=1}^{n^i_{\text{layer}}} \left\langle \left(\boldsymbol{\phi}^T \{\bar{\boldsymbol{l}}_{\boldsymbol{i}}\}_k \right)^2 \right\rangle \tag{A.11}$$

Since each row vector of the discrete Laplacian contains no more than 5 non-zero element, which defined by the stencil, $\left\langle \left(\boldsymbol{\phi}^T \{\bar{\boldsymbol{l}}_{\boldsymbol{i}}\}_k \right)^2 \right\rangle$ for non-boundary phase point

is computed as

$$\begin{aligned}\left\langle \left(\boldsymbol{\phi}^T\{\bar{\boldsymbol{l}}_{\boldsymbol{i}}\}_k\right)^2 \right\rangle &= \left\langle \left(\sum_{j=1}^{5} \phi_j \omega_j\right)^2 \right\rangle \\ &= -\frac{1}{2}\sum_{j,j'=1}^{5} \omega_j \omega_{j'} \left\langle (\phi_j - \phi_{j'})^2 \right\rangle \\ &= -\frac{1}{2}\sum_{j,j'=1}^{5} \omega_j \omega_{j'} D_\phi(\xi_{j,j'}) \end{aligned} \tag{A.12}$$

where D_ϕ is a phase structure function from Eq. (1.7) for the Kolmogorov model or Eq. (1.14) for the von Karman model and $xi_{i,j'}$ is a spatial separation between phase point j and j'. Then, $\left\langle \left(\boldsymbol{\phi}^T\{\bar{\boldsymbol{l}}_{\boldsymbol{i}}\}_k\right)^2 \right\rangle$ for the boundary phase points can be computed similarly. Finally, the scale constant c_i can be obtained by combining Eq. (A.10), Eq. (A.11), and Eq. (A.12).

Reference

[1] M. Akiyama, S. Oya, Y. H. Ono, H. Takami, S. Ozaki, Y. Hayano, I. Iwata, K. Hane, T. Wu, T. Yamamuro, and Y. Ikeda, "Tmt-age: wide field of regard multi-object adaptive optics for tmt," Proc. SPIE **9148**, 914814–914814–14 (2014).

[2] S. M. Ammons, L. Poyneer, D. T. Gavel, R. Kupke, C. E. Max, and L. Johnson, "Evidence that wind prediction with multiple guide stars reduces tomographic errors and expands moao field of regard," Proc. SPIE **8447**, 84471U (2012).

[3] D. R. Andersen, S. S. Eikenberry, M. Fletcher, W. Gardhouse, B. Leckie, J.-P. VÃľran, D. Gavel, R. Clare, R. Guzman, L. Jolissaint, R. Julian, and W. Rambold, "The moao system of the irmos near-infrared multi-object spectrograph for tmt," Proc. SPIE **6269**, 62694K–62694K–12 (2006).

[4] D. R. Andersen, K. J. Jackson, C. Blain, C. Bradley, C. Correia, M. Ito, O. LardiÃĺre, and J.-P. VÃľran, "Performance Modeling for the RAVEN Multi-Object Adaptive Optics Demonstrator," Publications of the Astronomical Society of the Pacific **124**, pp. 469–484 (2012).

[5] P. S. Argall, O. N. Vassiliev, R. J. Sica, and M. M. Mwangi, "Lidar measurements taken with a large-aperture liquid mirror. 2. sodium resonance-fluorescence system," Appl. Opt. **39**, 2393–2400 (2000).

[6] J. Beckers, "Increasing the size of the anisoplanatic patch with multiconjugate adaptive optics," Proc. ESO conference **4007**, 693–703 (1988).

[7] R. J. Bouwens, G. D. Illingworth, P. A. Oesch, M. Trenti, I. LabbÃľ, L. Bradley, M. Carollo, P. G. van Dokkum, V. Gonzalez, B. Holwerda, M. Franx, L. Spitler, R. Smit, and D. Magee, "Uv luminosity functions at redshifts z âĹij 4 to z âĹij 10: 10,000 galaxies from hst legacy fields," The Astrophysical Journal **803**, 34 (2015).

[8] T. Butterley, R. W. Wilson, and M. Sarazin, "Determination of the profile of atmospheric optical turbulence strength from SLODAR data," Monthly Notices of the Royal Astronomical Society **369**, 835–845 (2006).

[9] A. Consortini and L. Ronchi, "Choice of the model of atmospheric turbulence," Appl. Opt. **11**, 1205–1211 (1972).

[10] C. Correia, K. Jackson, J.-P. Véran, D. Andersen, O. Lardière, and C. Bradley, "Static and predictive tomographic reconstruction for wide-field multi-object adaptive optics systems," J. Opt. Soc. Am. A **31**, 101–113 (2014).

[11] C. M. Correia, K. Jackson, J.-P. Véran, D. Andersen, O. Lardière, and C. Bradley, "Spatio-angular minimum-variance tomographic controller for multi-object adaptive-optics systems," Appl. Opt. **54**, 5281–5290 (2015).

[12] A. CortÃľs, B. Neichel, A. Guesalaga, J. Osborn, F. Rigaut, and D. Guzman, "Atmospheric turbulence profiling using multiple laser star wavefront sensors," Monthly Notices of the Royal Astronomical Society **427**, 2089–2099 (2012).

[13] G. P. David J. E. Floyd, Jo Thomas-Osip, "Seeing, wind, and outer scale effects on image quality at the magellan telescopes," Publications of the Astronomical Society of the Pacific **122**, 731–742 (2010).

[14] E. Diolaiti, "MAORY: A Multi-conjugate Adaptive Optics RelaY for the E-ELT," The Messenger **140**, 28–29 (2010).

[15] B. L. Ellerbroek, "Efficient computation of minimum-variance wave-front reconstructors with sparse matrix techniques," J. Opt. Soc. Am. A **19**, 1803–1816 (2002).

[16] S. G. Els, T. Travouillon, M. SchÃűck, R. Riddle, W. Skidmore, J. Seguel, E. Bustos, and D. Walker, "Thirty Meter Telescope Site Testing VI: Turbulence Profiles," Publications of the Astronomical Society of the Pacific **121**, pp. 527–543 (2009).

[17] D. L. Fried, "Statistics of a geometric representation of wavefront distortion," J. Opt. Soc. Am. **55**, 1427–1435 (1965).

[18] Gendron, E., Vidal, F., Brangier, M., Morris, T., Hubert, Z., Basden, A., Rousset, G., Myers, R., Chemla, F., Longmore, A., Butterley, T., Dipper, N., Dunlop, C., Geng, D., Gratadour, D., Henry, D., Laporte, P., Looker, N., Perret, D., Sevin, A., Talbot, G., and Younger, E., "Moao first on-sky demonstration with canary," A&A **529**, L2 (2011).

[19] L. Gilles and B. Ellerbroek, "Shack-hartmann wavefront sensing with elongated sodium laser beacons: centroiding versus matched filtering," Appl. Opt. **45**, 6568–6576 (2006).

[20] L. Gilles, P. Massioni, C. Kulcsár, H.-F. Raynaud, and B. Ellerbroek, "Distributed Kalman filtering compared to Fourier domain preconditioned conjugate gradient for laser guide star tomography on extremely large telescopes," J. Opt. Soc. Am. A **30**, 898–909 (2013).

[21] A. Guesalaga, B. Neichel, A. CortÃľs, C. BÃľchet, and D. GuzmÃąn, "Using the C_n^2 and wind profiler method with wide-field laser-guide-stars adaptive

optics to quantify the frozen-flow decay," Monthly Notices of the Royal Astronomical Society **440**, 1925–1933 (2014).

[22] W. GÃď'ssler, S. Rabien, S. Esposito, M. Lloyd-Hart, L. Barl, U. Beckmann, T. Bluemchen, M. Bonaglia, J. L. Borelli, G. Brusa, J. Brynnel, P. Buschkamp, L. Busoni, L. Carbonaro, C. Connot, R. Davies, M. Deysenroth, O. Durney, R. Green, H. Gemperlein, V. Gasho, M. Haug, P. Hubbard, S. Ihle, M. Kulas, R. Lederer, J. Lewis, C. Loose, M. Lehmitz, J. Noenickx, E. Nussbaum, G. Orban de Xivry, D. Peter, A. Quirrenbach, M. Rademacher, W. Raab, J. Storm, C. Schwab, V. Vaitheeswaran, and J. Ziegleder, "Status of the argos ground layer adaptive optics system," Proc. SPIE **8447**, 844702–844702–10 (2012).

[23] F. Hammer, F. SayÃĺde, E. Gendron, T. Fusco, D. Burgarella, V. Cayatte, J. Conan, F. Courbin, H. Flores, I. Guinouard, L. Jocou, A. LanÃğon, G. Monnet, M. Mouhcine, F. Rigaud, D. Rouan, G. Rousset, V. Buat, and F. Zamkotsian, "The falcon concept: multi-object spectroscopy combined with mcao in near-ir," Proc. ESO workshop p. 139 (2002).

[24] J. W. Hardy, *Adaptive Optics for Astronomical Telescopes* (Oxford University Press, 1998).

[25] Y. Hayano, H. Takami, S. Oya, M. Hattori, Y. Saito, M. Watanabe, O. Guyon, Y. Minowa, S. E. Egner, M. Ito, V. Garrel, S. Colley, T. Golota, and M. Iye, "Commissioning status of Subaru laser guide star adaptive optics system," Proc. SPIE **7736**, 77360N (2010).

[26] T. M. Herbst, R. Ragazzoni, A. Eckart, and G. Weigelt, "Linc-nirvana: achieving 10 mas imagery on the large binocular telescope," Proc. SPIE **7014**, 70141A–70141A–6 (2008).

[27] G. H. Herriot, D. R. Andersen, J. Atwood, C. Correia, P. Byrnes, C. Boyer, K. Caputa, J. Dunn, B. Ellerbroek, J. Fitzsimmons, L. Gilles, P. Hickson, A. Hill, J. Pazder, V. Reshetov, S. Roberts, M. Smith, J.-P. Veran, L. Wang, and I. Wevers, "Nfiraos; tmt early light adaptive optics system," Imaging and Applied Optics p. AWA4 (2011).

[28] K. Jackson, C. Correia, O. LardiÃĺre, D. Andersen, C. Bradley, L. Pham, C. Blain, R. Nash, D. Gamroth, and J.-P. VÃľran, "Tomography and calibration for raven: from simulations to laboratory results," Proc. SPIE **9148**, 91482K–91482K–13 (2014).

[29] N. Kobayashi, A. T. Tokunaga, H. Terada, M. Goto, M. Weber, R. Potter, P. M. Onaka, G. K. Ching, T. T. Young, K. Fletcher, D. Neil, L. Robertson, D. Cook, M. Imanishi, and D. W. Warren, "IRCS: infrared camera and

spectrograph for the Subaru Telescope," Proc. SPIE **4008**, 1056–1066 (2000).

[30] A. N. Kolmogorov, "Dissipation of energy in the locally isotropic turbulence," Akademiia Nauk SSSR **32**, 16 (1941).

[31] M. Lamb, D. R. Andersen, J.-P. VÃľran, C. Correia, G. Herriot, M. Rosensteiner, and J. Fiege, "Non-common path aberration corrections for current and future ao systems," Proc. SPIE **9148**, 914857–914857–13 (2014).

[32] O. LardiÃĺre, D. Andersen, C. Blain, C. Bradley, D. Gamroth, K. Jackson, P. Lach, R. Nash, K. Venn, J.-P. VÃľran, C. Correia, S. Oya, Y. Hayano, H. Terada, Y. Ono, and M. Akiyama, "Multi-object adaptive optics on-sky results with Raven," Proc. SPIE **9148**, 91481G (2014).

[33] J.-F. Lavigne, F. Lamontagne, G. Anctil, M. Wang, M. Tremblay, O. LardiÃĺre, R. Nash, D. Andersen, M. Savard, P. CÃťtÃľ, C. H. Bradley, and F. ChÃćteauneuf, "Design and test results of the calibration unit for the MOAO demonstrator RAVEN," Proc. SPIE **8447**, 844754 (2012).

[34] C. Lawson and R. Hanson, *Solving Least Squares Problems* (Prentice-Hall, 1974).

[35] L. H. Lee, "Sparse-matrix regularization for minimum-variancereconstruction of pseudo-kolmogorov turbulence," in "Adaptive Optics: Analysis and Methods/Computational Optical Sensing and Imaging/Information Photonics/Signal Recovery and Synthesis Topical Meetings on CD-ROM," (Optical Society of America, 2007), p. JTuA2.

[36] L. Lessard, M. West, D. MacMynowski, and S. Lall, "Warm-started wavefront reconstruction for adaptive optics," J. Opt. Soc. Am. A **25**, 1147–1155 (2008).

[37] J. V. M. Azouit, "Optical turbulence profiling with balloons relevant to astronomy and atmospheric physics," Publications of the Astronomical Society of the Pacific **117**, 536–543 (2005).

[38] P. Massioni, C. Kulcsár, H.-F. Raynaud, and J.-M. Conan, "Fast computation of an optimal controller for large-scale adaptive optics," J. Opt. Soc. Am. A **28**, 2298–2309 (2011).

[39] A. Miyashita, N. Takato, T. Usuda, F. Uraguchi, and R. Ogasawara, "Statistics of the weather data, environment data, and the seeing of the Subaru Telescope," Proc. SPIE **5489**, 207–217 (2004).

[40] B. Neichel, F. Rigaut, F. Vidal, M. A. van Dam, V. Garrel, E. R. Carrasco, P. Pessev, C. Winge, M. Boccas, C. d'Orgeville, G. Arriagada, A. Serio, V. Fesquet, W. N. Rambold, J. LÃijhrs, C. Moreno, G. Gausachs, R. L. Galvez, V. Montes, T. B. Vucina, E. Marin, C. Urrutia, A. Lopez, S. J.

Diggs, C. Marchant, A. W. Ebbers, C. Trujillo, M. Bec, G. Trancho, P. McGregor, P. J. Young, F. Colazo, and M. L. Edwards, "Gemini multiconjugate adaptive optics system review âĂŞ ii. commissioning, operation and overall performance," Monthly Notices of the Royal Astronomical Society **440**, 1002–1019 (2014).

[41] A. M. Obukhov, "Structure of the temperature field in a turbulent flow," Akademiia Nauk SSSR **13**, 58 (1949).

[42] L. Poyneer, M. van Dam, and J.-P. Véran, "Experimental verification of the frozen flow atmospheric turbulence assumption with use of astronomical adaptive optics telemetry," J. Opt. Soc. Am. A **26**, 833–846 (2009).

[43] F. J. Rigaut, B. L. Ellerbroek, and R. Flicker, "Principles, limitations, and performance of multiconjugate adaptive optics," Proc. SPIE **4007**, 1022–1031 (2000).

[44] F. Rigaut, B. Neichel, M. Boccas, C. d'Orgeville, F. Vidal, M. A. van Dam, G. Arriagada, V. Fesquet, R. L. Galvez, G. Gausachs, C. Cavedoni, A. W. Ebbers, S. Karewicz, E. James, J. LÃijhrs, V. Montes, G. Perez, W. N. Rambold, R. Rojas, S. Walker, M. Bec, G. Trancho, M. Sheehan, B. Irarrazaval, C. Boyer, B. L. Ellerbroek, R. Flicker, D. Gratadour, A. Garcia-Rissmann, and F. Daruich, "Gemini multiconjugate adaptive optics system review âĂŞ i. design, trade-offs and integration," Monthly Notices of the Royal Astronomical Society **437**, 2361–2375 (2014).

[45] G. Rousset, T. Fusco, F. Assemat, E. Gendron, T. Morris, C. Robert, R. Myers, M. Cohen, N. Dipper, C. Evans, D. Gratadour, P. Jagourel, P. Laporte, D. Le Mignant, M. Puech, H. Schnetler, W. Taylor, F. Vidal, J.-G. Cuby, M. Lehnert, S. Morris, and P. Parr-Burman, "Eagle moao system conceptual design and related technologies," Proc. SPIE **7736**, 77360S–77360S–11 (2010).

[46] M. Schöck and E. J. Spillar, "Method for a quantitative investigation of the frozen flow hypothesis," J. Opt. Soc. Am. A **17**, 1650–1658 (2000).

[47] V. I. Tatarski, *Wave Propagaton in a Turbulent Medium* (McGraw-Hill, 1961).

[48] A. Tokovinin, "From differential image motion to seeing," Publications of the Astronomical Society of the Pacific **114**, pp. 1156–1166 (2002).

[49] C. R. Vogel and Q. Yang, "Fast optimal wavefront reconstruction for multiconjugate adaptive optics using the fourier domain preconditioned conjugate gradient algorithm," Opt. Express **14**, 7487–7498 (2006).

[50] R. W. Wilson, "SLODAR: measuring optical turbulence altitude with a

ShackâĂŞHartmann wavefront sensor," Monthly Notices of the Royal Astronomical Society **337**, 103–108 (2002).

[51] S. A. Wright, E. J. Barton, J. E. Larkin, A. M. Moore, D. Crampton, and L. Simard, "The infrared imaging spectrograph (iris) for tmt: sensitivities and simulations," Proc. SPIE **7735**, 77357P–77357P–13 (2010).